Probing the Decay Characteristics of the Pygmy Dipole Resonance in the Semi-Magic Nucleus ^{140}Ce with γ-γ Coincidence Measurements

Dissertation

zur Erlangung des Grades
"Doktor der Naturwissenschaften"
im Promotionsfach Physik

am Fachbereich Physik, Mathematik und Informatik
der Johannes Gutenberg-Universität Mainz

Bastian Löher, M.Sc.

geboren in Krefeld

Darmstadt, 2014

Datum der Einreichung: 03.10.2014
Tag der mündlichen Prüfung: 08.07.2014

Zusammenfassung

Im Rahmen dieser Arbeit wurde ein neuartiger Experimentaufbau – das γ^3 Experiment – zur Messung von photoneninduzierten Kern-Dipolanregungen in stabilen Isotopen konzipiert und an der High Intensity γ-ray Source (HIγS) an der Duke University installiert. Die hohe Energieauflösung und die hohe Nachweiseffizienz des Detektoraufbaus, welcher aus einer Kombination von $LaBr_3$:Ce Szintillatoren und hochreinen Germanium-Detektoren besteht, erlaubt erstmals die effiziente Messung von γ-γ-Koinzidenzen in Verbindung mit der Methode der Kernresonanzfluoreszenz. Diese Methode eröffnet den Zugang zum Zerfallsverhalten der angeregten Dipolzustände als zusätzlicher Observablen, die ein detaillierteres Verständnis der zugrunde liegenden Struktur dieser Anregungen ermöglicht. Der Detektoraufbau wurde bereits erfolgreich im Rahmen von zwei Experimentkampagnen in 2012 und 2013 für die Untersuchung von 13 verschiedenen Isotopen verwendet. Im Fokus dieser Arbeit stand die Analyse der Pygmy-Dipolresonanz (PDR) im Kern ^{140}Ce im Energiebereich von 5.2 MeV bis 8.3 MeV basierend auf den mit dem γ^3 Experimentaufbau gemessenen Daten. Insbesondere das Zerfallsverhalten der Zustände, die an der PDR beteiligt sind, wurde untersucht.

Der Experimentaufbau, die Details der Analyse sowie die Resultate werden in der vorliegenden Arbeit präsentiert. Desweiteren erlaubt ein Vergleich der Ergebnisse mit theoretischen Rechnungen im quasi-particle phonon model (QPM) eine Interpretation des beobachteten Zerfallsverhaltens.

Abstract

This work presents the design and installation of a novel experimental setup – the γ^3 setup – for measuring photon-induced nuclear dipole excitations in stable isotopes at the High Intensity γ-ray Source (HIγS) at the Duke University. The high energy resolution and high detection efficiency of the detector array, consisting of a combination of $LaBr_3$:Ce and HPGe detectors, allows for the first time the efficient measurement of γ-γ-coincidences in combination with the method of nuclear resonance fluorescence. This technique provides access to the decay pattern of dipole excited states as an additional observable, which allows a deeper insight into the underlying structure of these excitations. The experimental setup has already been used successfully for two experimental campaigns in 2012 and 2013 in the investigation of 13 different target isotopes. Within the scope of this thesis the Pygmy Dipole Resonance (PDR) of ^{140}Ce was studied in the excitation energy range from 5.2 MeV to 8.3 MeV based on data obtained with the γ^3 setup. In particular the decay pattern of the states participating in the PDR was investigated.

The experimental setup, the details of the analysis and the experimental results are presented in this thesis. A comparison of the results to theoretical quasi-particle phonon model (QPM) calculations allows for an interpretation of the observed decay behaviour.

Contents

1 Introduction **1**
- 1.1 The Pygmy Dipole Resonance . . . 3
- 1.2 The case of ^{140}Ce . . . 4
- 1.3 The γ-γ-coincidence method . . . 5

2 Theoretical Basis **9**
- 2.1 Nuclear Resonance Fluorescence . . . 9
- 2.2 Angular distributions of emitted photons . . . 11
  - 2.2.1 Generic formalism . . . 12
  - 2.2.2 Emission of photons following excitation with linearly polarised radiation . . . 15
  - 2.2.3 Example distributions . . . 16
- 2.3 Spectrum unfolding . . . 17
  - 2.3.1 Top-Down unfolding . . . 19
  - 2.3.2 Gold unfolding method . . . 20

3 Experimental Setup **25**
- 3.1 The HIγS facility at TUNL . . . 25
  - 3.1.1 Production of a quasi-monoenergetic photon beam . . . 25
- 3.2 The γ^3 setup . . . 27
  - 3.2.1 Modifications to the existing experimental setup . . . 28
- 3.3 Data acquisition . . . 33
  - 3.3.1 GENIE system . . . 33
  - 3.3.2 MBS system . . . 33
  - 3.3.3 Software . . . 37
  - 3.3.4 ADC integral linearity . . . 38
- 3.4 Diagnostics . . . 40
  - 3.4.1 Measurement of photon flux and energy . . . 41
  - 3.4.2 Deadtime measurement . . . 41
  - 3.4.3 Beam pulse pickup . . . 42
  - 3.4.4 Target alignment . . . 43
- 3.5 Experimental run . . . 43

3.6 Differences between the 2012 and 2013 beam time 44

4 Data Analysis **47**
4.1 Experimental procedure 47
4.1.1 Spectrum unfolding 49
4.1.2 Energy calibration 52
4.1.3 Efficiency calibration 56
4.1.4 Event selection 59
4.1.5 Background estimation 62
4.1.6 Determination of the photon flux 64
4.2 Singles spectra 69
4.2.1 Angular distributions 69
4.2.2 Extraction of cross-sections 70
4.2.3 Parity measurement 70
4.2.4 Branching ratios to excited states 71
4.3 Analysis of γ-γ coincidence data 71
4.3.1 Projected spectra 74
4.3.2 Angular correlation 78
4.3.3 Extraction of branching ratios 79

5 Experimental results for ^{32}S **81**
5.1 Branching ratio 81
5.2 Angular distributions 84

6 Experimental results for ^{140}Ce **87**
6.1 Nuclear levels 87
6.2 Parity measurements 89
6.3 Branching ratios from singles data 91
6.4 Branching ratios for single states 93
6.5 Averaged branching ratios 96

7 Summary and Outlook **101**
7.1 Future experiments 102

A Experimental data **105**
A.1 Levels of ^{140}Ce 105
A.2 Angular distributions 111

B Experimental supplement **113**
B.1 Trigger generation matrices 113
B.2 GHOST - Gamma Histogramming and Online Spectra Tool 116
B.3 Backup strategies 117

List of Figures

1.1 Schematic E1 strength distribution . . . 3
1.2 Splitting of the PDR in ^{140}Ce . . . 4
1.3 NRF principle . . . 6

2.1 Coordinate system . . . 14
2.2 Example distributions . . . 18
2.3 Detector response simulation . . . 20
2.4 Example for Top-Down Unfolding . . . 21
2.5 Examples for Gold unfolding . . . 22
2.6 Refolded spectra after Gold unfolding . . . 23

3.1 Overview of the HIγS facility . . . 26
3.2 Overview of the γ^3 setup . . . 27
3.3 γ^3 schematic drawing . . . 28
3.4 Detector layout . . . 29
3.5 Total full energy peak efficiency of the γ^3 setup . . . 30
3.6 HPGe spectrum without target . . . 31
3.7 Schematic overview of the data acquisition system . . . 34
3.8 Schematic of QDC gate generation . . . 36
3.9 Trigger matrix example . . . 37
3.10 The GHOST Histogramming Tool . . . 39
3.11 Integral linearity . . . 40
3.12 Beam energy distribution, measured and deconvoluted . . . 40
3.13 Time difference between detector and beam pickup . . . 42
3.14 CCD image of the photon beam . . . 43

4.1 Unfolding methods . . . 48
4.2 Unfolding result vs. calibration . . . 51
4.3 Gain vs. Time . . . 53
4.4 Peak width calibration . . . 54
4.5 LaBr non-linearity . . . 55
4.6 FOM vs. calibration . . . 56
4.7 Detector efficiency 2012 and 2013 . . . 57
4.8 GEANT4 geometry . . . 58

4.9 Timing selection 60
4.10 Time difference 61
4.11 Natural background 62
4.12 Simulated non-resonant background 63
4.13 Synthetic spectra 65
4.14 Beam shape model 66
4.15 Paddle Rate 68
4.16 Level scheme ^{140}Ce 72
4.17 Coincidence matrices 73
4.18 Projections HPGe-LaBr (all energies) 74
4.19 Projections HPGe-LaBr (only 2^+) at 5200 keV 75
4.20 Projections HPGe-LaBr (only 2^+) at 8300 keV 76
4.21 Projections unfolded 77

5.1 Level scheme of ^{32}S 82
5.2 HPGe spectra of ^{32}S 83
5.3 $LaBr_3$:Ce spectra of ^{32}S 84
5.4 Angular distribution of ^{32}S singles 85
5.5 Angular distribution of ^{32}S coincidences 86

6.1 B(E1) strength in ^{140}Ce 88
6.2 B(E1) strength in ^{140}Ce vs. QPM 89
6.3 Parities ^{140}Ce 90
6.4 Feeding of low-lying states, cross section 92
6.5 Branching ratio 5.6 MeV 93
6.6 Branching ratio 6.5 MeV 94
6.7 Projections unfolded 5.2 MeV and 6.5 MeV 97
6.8 Projections unfolded 98
6.9 Averaged branching ratios ^{140}Ce Top-Down 99
6.10 Averaged branching ratios ^{140}Ce Gold 99

List of Tables

3.1 HIγS γ-beam properties 25
3.2 γ^3 experiments 44

4.1 Experimental properties 49
4.2 Photon Flux 69

5.1 Branching ratio ^{32}S singles 82

6.1 Branching ratio ^{140}Ce single states 95

A.1 Nuclear levels in ^{140}Ce 105
A.2 Angular correlations 2012 111
A.3 Angular correlations 2013 112

B.1 Trigger Generation 2012 114
B.2 Trigger Generation 2013 115

Chapter 1

Introduction

Nuclear physics is a vast scientific field concerned with the fundamental aspects of nature, striving for a coherent and complete understanding of the world we live in, from the extremely large structures of the universe down to the smallest scales of atoms, nuclei and their constituents. The aim of nuclear physics is to give conclusive answers to lingering questions about the beginning of time in the Big Bang, about the origin of matter and the elements in the universe. Starting in the early 20th century from the first experiments with radioactivity conducted by A. H. Becquerel, and P. and M. Curie [1], nuclear physics has evolved into a highly diverse research area intertwining experimental and theoretical advances, and today represents the foundational basis for explaining the complexity of our surroundings.

Nuclear physics is based on a quantum mechanical description of matter and its fundamental interactions, and only few aspects can be properly described within the regime of classical mechanics. Experimental techniques involve particle accelerators and radiation detectors, ranging from table-top setups to large-scale installations like the Large Hadron Collider at the CERN research facility or the IceCube neutrino observatory.

Today's low-energy nuclear physics, as opposed to high-energy physics or particle physics, is mainly concerned with the study of the atomic nucleus, its structure and its interaction with external fields. The discovery of the atomic nucleus in α-scattering experiments [2] marked the beginning of nuclear structure physics and sparked the interest to investigate the properties of nuclei across the nuclear landscape.

The atomic nucleus and its underlying structure can be investigated by using electromagnetic or hadronic probes with sufficiently high energy. The radial extent of the typical nucleus is on the order of a few fm, which translates to an energy range of 1 MeV to 100 MeV. One of the most important observables, which yields information about the nuclear structure, is the probability of scattering a probe of a certain energy into a specific solid angle, called the *differential cross-section* $\frac{\mathrm{d}\sigma}{\mathrm{d}\Omega}$. In the past, experiments with different probes such as pho-

tons, electrons, protons, neutrons, α-particles, and heavier particles have been performed.

Of particular importance for nuclear structure physics are photon-scattering, or Nuclear Resonance Fluorescence (NRF), experiments where the nucleus is excited via resonant photo-absorption, and subsequently de-excites via emission of one or more photons. The first successful NRF experiment was conducted by P. B. Moon in 1951 [3] on ^{198}Hg using ^{198}Au in a centrifuge as a radiation source. First experiments were limited to the investigation of excited nuclear states close to energies that could be reached with natural radioactive sources. The availability of high energy bremsstrahlung photons for NRF [4] and the development of high-resolution semi-conductor Germanium detectors enabled a quick expansion of the field and allowed the investigation of stable nuclei over a wide energy range [5, 6] and with high precision. More recently, experiments using a completely polarised photon beam from a laser Compton back-scattering (LCB) facility have been carried out by Ohgaki *et al.* [7]. This method was used for the investigation of nuclear level parities by Pietralla *et al.* [8, 9] at the High Intensity γ-ray Source [10] (HIγS) at the Triangle Universities National Laboratory (TUNL).

In NRF experiments the photo-absorption cross-section is measured with high accuracy and without additional input from model calculations. From this cross-section the radiation widths Γ_i can be determined, which are proportional to the reduced transition probabilities B(XL) for radiation of multipolarity L and character X. The energy dependent distribution of the reduced transition probabilities is called the strength distribution. The typical strength distribution for dipole-excited states (or photoresponse) of a spherical nucleus is shown schematically in Fig. 1.1. The most prominent feature is the Giant Dipole Resonance (GDR) in the energy range above the particle separation threshold, which was first experimentally established by G. C. Baldwin and G. S. Klaiber [11] using photo-fission reactions. The cross-section observed in this resonance exhausts nearly 100 % of the Thomas-Reiche-Kuhn sum-rule [12, 13]. The nature of this excitation mode was explained as an isovectorial collective dipole oscillation of all protons against all neutrons in the nucleus by Goldhaber and Teller [14]. On the low-energy part of the spectrum, a single state stands out. The lowest 1^- state in spherical nuclei, the so-called 2-phonon state, was studied systematically in (γ, γ') experiments [15–18] and with hadronic probes [19, 20]. These studies have shown that this state is a coupled $[2^+ \otimes 3^-]$ quadrupole-octupole excitation [21], and that it has dominant isoscalar character [22]. In the study of neutron capture γ-rays (see e.g. [23]) the first evidence for an enhancement of low-lying dipole strength, located around the particle separation threshold, was observed in many isotopes. Today, this excitation is commonly denoted as the *Pygmy Dipole Resonance* (PDR), because it carries only a comparatively small fraction of the total dipole strength.

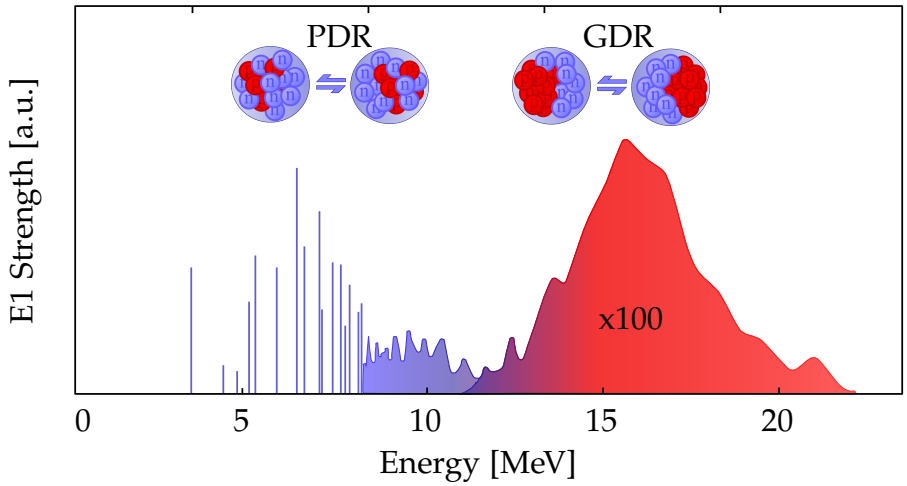

Figure 1.1: Schematic electric dipole strength distribution in spherical atomic nuclei.

1.1 The Pygmy Dipole Resonance

The PDR was first described in the context of a three-fluid hydro-dynamical model by R. Mohan *et al.* [24], which reproduced the large asymmetry between the fraction of the dipole strength in the GDR and the PDR. This model suggested the interpretation of the PDR mode as an oscillation of valence neutrons against a core of protons and *blocked* neutrons. Numerous measurements within the last 20 years focused primarily on the investigation of this 'new' excitation mode using bremsstrahlung beams, e.g. in Gent [25], Darmstadt [26–28] and Dresden [29], with LCB photons [30–32], α-particles [33–36] as well as with radioactive ion beams at GSI [37–39]. Despite comprehensive systematic studies in, e.g. the Ca [28] and Sn [38, 40] isotopes, as well as the N = 82 isotones [34], the underlying excitation mechanism of the PDR is still under discussion. Particularly the degree of collectivity exhibited by the PDR and the isospin character of the strength attributed to the PDR are a matter of current interest [33, 41, 42]. The experimental studies of the Pygmy Dipole Resonance have been compiled in an extensive review by D. Savran [43].

The theoretical description of the PDR is usually carried out using mean-field calculations, such as Hartree-Fock and Hartree-Fock-Bogoliubov approaches [44, 45]. Many different attempts have been made to reproduce the strength in the Pygmy region, and to gain access to underlying processes that cause this phenomenon. Today, several different theoretical approaches to describe the PDR are pursued, such as for example the (quasi-particle) random phase approximation [42, 46–50], the second RPA [51, 52], the extended theory of finite fermi systems (ETFFS) [28, 53], or the algebraic Interacting Boson Approximation (IBA) [54]. Two promising approaches that allow a microscopic understand-

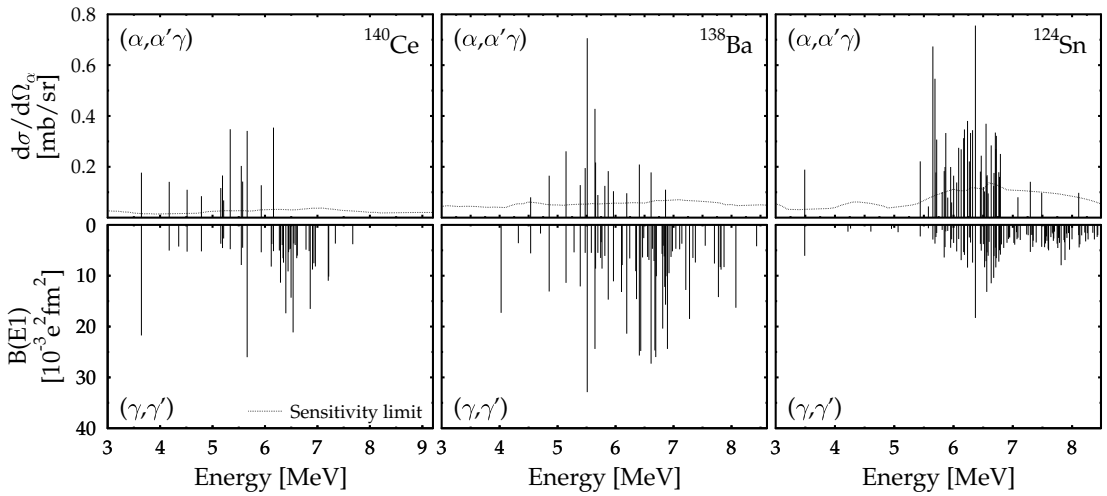

Figure 1.2: Comparison of cross-sections measured in the $(\alpha, \alpha'\gamma)$ experiments (upper part) with B(E1) strengths derived from (γ, γ') (lower part) for ^{140}Ce, ^{138}Ba and ^{124}Sn. The line in the upper part indicates the sensitivity limit [62].

ing of the PDR, are the relativistic quasi-particle random phase approximation (RQRPA), its extension, the relativistic quasi-particle time-blocking approximation (RQTBA) [55–57], and the quasi-particle phonon model (QPM) [58, 59] with coupling to complex configurations. It has been shown that this coupling to complex configurations, that has been incorporated in the model description, plays a crucial role in recreating the strong fragmentation of the strength in the PDR region [60]. A comprehensive review of the theoretical studies of collective excitations has been compiled by N. Paar [61].

1.2 The case of ^{140}Ce

The dipole response of the nucleus ^{140}Ce was investigated with the NRF method already in 1997 by R. D. Herzberg *et al.* [60] to study the PDR. Subsequent studies of ^{140}Ce extended the energy range [63], and used α-scattering as a complementary probe [34]. A surprising splitting of the PDR was discovered, when the dipole excited states below 6.5 MeV were investigated in the (γ, γ') experiment as well as in the $(\alpha, \alpha'\gamma)$ experiment. The E1 states above this energy were instead only excited in the (γ, γ') reaction (see Fig. 1.2). This kind of structural splitting has also been discovered in other nuclei in the same mass region [33, 64]. A likely cause for this splitting is the different isospin nature of the two experimental probes and their distinct interaction regions within the nucleus [35]. Photons of E1 character are isovectorial probes and tend to interact with the nucleus as a whole, because of their long wavelength in comparison

to the nuclear radius. In contrast, α-particles are isoscalar probes and interact strongly with the surface of the nucleus. These results started new efforts to fully understand the nature of the PDR excitation.

An additional observable that can be exploited to investigate the nature of the PDR and collect supplementary information is the *decay pattern* of the states that participate in the PDR region. This includes studying the branching ratios of the PDR states to the low-lying excited states. The partial decay widths Γ_i of transitions to low-lying excited states or to the ground state are directly linked to the electromagnetic transition matrix elements between the corresponding states. Therefore, each decay channel is sensitive to a different component in the wave function. The observation of these transitions and the determination of branching ratios thus reveals important experimental information, which is needed to provide stringent and sensitive tests to modern model calculations.

For instance, the QPM description of the nuclear excitations predicts the presence of one-phonon 1^- states in the PDR region, that predominantly decay to the ground state, and others (two-phonon states) that decay strongly to excited 2^+ states. Within the model, these states constitute different parts of the PDR wave function, i.e. a PDR built on the ground state, a second one built on the first 2^+ state, and so on. The latter have very weak excitation probability from the ground state compared to the first one. The coupling between simple and complex configurations introduces mixing between the different PDR components (i.e. $[1^- \otimes 2_1^+]$) and other two- and three-phonon states and leads to the strong fragmentation that is known from experimental data. By studying the direct decays to the ground state as well as decays to excited states, it is possible to investigate the strength of this mixing [65].

1.3 The γ-γ-coincidence method

Figure 1.3 illustrates the principle of the NRF method. A nucleus A_x is excited from the ground state (Energy 0) to an excited state with energy E_γ and angular momentum J. The de-excitation can either happen directly back to the ground state, or via intermediate states. Experimental evidence shows that the direct decay to the ground state is the dominant de-excitation channel, i.e. that individual branching ratios to excited states (indicated as Γ_i in Fig 1.3) are small in comparison to the ground state radiation width Γ_0 (see e.g. [25]). However, additional experiments have shown that, especially at higher excitation energy, the integrated radiation width to excited states stemming from a multitude of possible decays can represent a substantial fraction of the total width Γ [30, 32, 66].

So far, the experimental sensitivity in past NRF experiments was not sufficient to observe peaks stemming from these transitions to excited states. In the energy range where these transitions are expected, the background originating from the photon beam and from non-resonant scattering processes in the target

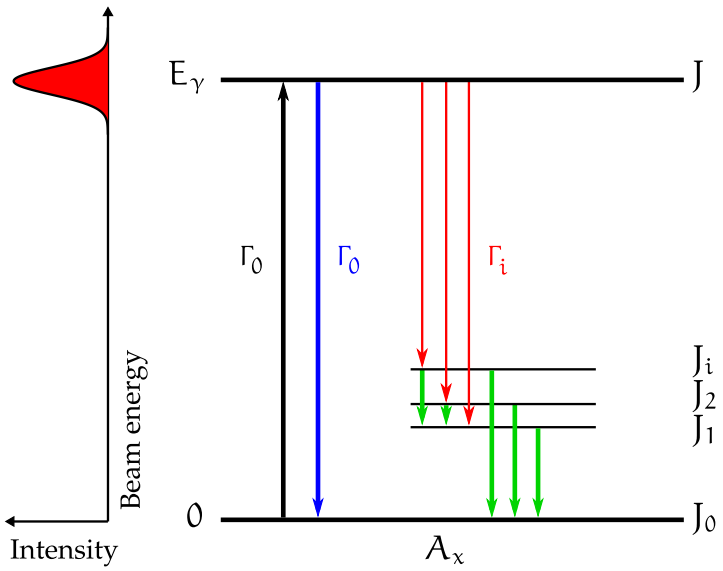

Figure 1.3: The nuclear resonance fluorescence (NRF) principle.

is substantial. Therefore, the peak to background ratio for these transitions is too small to allow for a proper analysis. The method of in-beam γ-ray coincidences in the spectroscopy of the γ-decay of excited states in combination with charged-particle induced reactions was proven to be a powerful tool for measuring even small branching ratios to excited low-lying states [67, 68]. Until now γ-γ-coincidence experiments have been performed mainly in combination with particle-induced reactions [69]. In such reactions high-lying $J = 1$ states are often not or only very weakly excited, which excludes the investigation of the decay pattern of such states.

The NRF reaction prefers a selective excitation of $J = 1$ states, since the excitation mechanism is highly selective to dipole-excited states [15]. The combination of the NRF reaction with γ-γ-coincidences in the decay spectroscopy thus provides selectivity plus high sensitivity to transitions to excited states. In addition the linearly polarised quasi-monoenergetic photon beam of the HIγS facility allows to excite the target nucleus only in a narrow energy range. This is indicated by the beam intensity distribution in Fig. 1.3. Combining these methods prepares the nucleus in an initial state with well-known energy and angular momentum. To measure the subsequent decay of the nucleus with the γ-γ-coincidence method, an experimental setup with a high photo-peak efficiency is needed to detect the two photons.

Within the scope of this thesis a new experimental setup was installed at the HIγS facility, with the aim to increase the experimental sensitivity to weak transitions, and to allow the direct and model-independent measurement of the decay pattern of dipole-excited states. The γ^3 setup [70], which is described

in detail in Chapter 3, is a small detector array consisting of a combination of high-resolution HPGe[1] detectors and $LaBr_3$:Ce scintillation detectors with high full-energy peak efficiency.

In 2012 and 2013 the γ^3 setup was used in two experimental campaigns. In total more than 1400 h of beam time was spent on the investigation of 12 different nuclei in the low, medium and heavy mass region. The objectives were the investigation of low-lying E1 strength and the decay of the PDR, the study of the fragmentation of the M1 scissors mode [71–73], as well as the measurement of the $[2^+ \otimes 3^-]$ 2-phonon state in light and heavy nuclei.

This thesis covers the analysis of the ^{32}S data from the commissioning phase, and the analysis of the E1 strength distribution as well as the decay of the PDR in ^{140}Ce. Chapter 4 contains a detailed description of the analysis steps. The results of the analyses are shown in Chapters 5 and 6. An introduction to the necessary theoretical background is given in the following chapter.

[1] high-purity Germanium

Chapter 2

Theoretical Basis

This chapter gives an overview of the basic theoretical concepts that are used throughout the course of this thesis. First the method of nuclear resonance fluorescence (NRF) is introduced along with the description of the physical observables. Then a more detailed discussion of angular distributions and correlations follows, which are used in the analysis of coincidence data. The chapter closes with the introduction of unfolding methods for energy spectra.

2.1 Nuclear Resonance Fluorescence

The method of nuclear resonance fluorescence has been in use for over 50 years [74]. This method allows to probe the structure of the nucleus in a model-independent way, since the observables such as the photo-absorption cross-section, the transition widths for individual states, and the reduced transition probabilities can be directly determined from the data without additional input from model calculations [15]. It is very sensitive to dipole excitations and enables the study of single excited states with the use of high-resolution HPGe detectors.

The principle of NRF involves the excitation of a nucleus from the ground state to an excited state by photon absorption and the successive de-excitation by photon emission. This process is illustrated in Figure 1.3. The energy E_γ of the absorbed photon (black arrow) must be equal to the energy difference between the two nuclear states in order to be absorbed in a resonant way. The figure shows the ground state with total angular momentum J_0 and the excited state with total angular momentum J, that is excited through a photon with energy E_γ. The Γ_i indicate the associated partial radiation widths for each of the shown de-excitations. Especially in heavy nuclei there exists not only a single path for de-excitation from an excited state, but instead one of many different decay paths are possible. The direct decay back to the ground state indicated by Γ_0 (blue) is usually referred to as the *elastic* transition, while the transitions

involving intermediate states are called *inelastic* (red). The question, why one or the other path is preferred by the nucleus is of particular interest in nuclear structure physics and theoretical models attempt to describe this *decay behaviour* correctly. Past experiments have shown that the majority of states excited in the NRF reaction decay directly back to the ground state with a large partial radiation width Γ_0. The partial radiation widths Γ_i to excited states are usually comparatively small, such that the total radiation width Γ can be approximately equal to the ground state radiation width Γ_0. However, if a large number of possible decay paths is available, the sum of Γ_i can result in a significant contribution to Γ

$$\Gamma = \Gamma_0 + \sum_{i=1}^{n} \Gamma_i \tag{2.1}$$

The quantity

$$b_i = \frac{\Gamma_i}{\Gamma} \tag{2.2}$$

is called the *branching ratio*, i.e. the relative probability for the transition Γ_i to the i^{th}-excited state to take place. This quantity is of particular importance in this thesis, because the experimental setup described in Chapter 3 allows for the first time to measure this branching ratio directly in a model independent way. The branching ratio plays a major role in the determination of cross-sections and dipole-transition strengths, as is introduced below.

In each transition in Figure 1.3 the emitted radiation has a multipole order λ that satisfies the triangle relation of the associated initial and final angular momenta J_i and J_f:

$$|J_i - J_f| < \lambda < |J_i + J_f| \,. \tag{2.3}$$

The multipole character of the radiation is determined from the parities π_i and π_f of the participating states using the selection rules:

$$\text{Electric radiation} \quad (E\lambda): \quad \pi_i = (-1)^{\lambda}\pi_f \tag{2.4}$$

$$\text{Magnetic radiation} \quad (M\lambda): \quad \pi_i = (-1)^{\lambda+1}\pi_f \,. \tag{2.5}$$

Since photons mainly induce dipole-transitions as well as electric quadrupole-transitions, NRF experiments are perfectly suited for the investigation of nuclear states with $J = 0, 1, 2$ in even-even nuclei.

One of the physical observables accessible in NRF experiments is the energy-integrated cross-section for the excitation of a nucleus from the ground state to an excited state with energy E_j and angular momentum J_j, and the subsequent de-excitation to a final state k. This integrated quantity $I_{j\to k}(E)$ results from an integral over the photo-absorption cross-section $\sigma_{j\to k}$, which is given by

$$\sigma_{j\to k}(E) = \frac{\pi}{2}\left(\frac{\hbar c}{E_j}\right)^2 \cdot g \cdot \frac{\Gamma_0\Gamma_j}{(E - E_j)^2 + \Gamma^2/4} \tag{2.6}$$

with the spin-statistical factor $g = (2J_j + 1)/(2J_0 + 1)$. This cross-section has a Breit-Wigner shape with a full width at half maximum (FWHM) of Γ. Additional effects such as the Doppler broadening caused by thermal motion of the nucleus, modify the line shape and increase the apparent width. The integral over the cross-section, however, stays the same. Due to the energy resolution, which is usually limited to a few keV, only the energy-integrated cross-section is accessible. This leads to the following expression

$$I_{j\to k}(E_j) = \int \sigma_{j\to k}(E)\, dE = \pi^2 \left(\frac{\hbar c}{E_j}\right)^2 \cdot g \cdot \frac{\Gamma_0 \Gamma_j}{\Gamma}\,. \tag{2.7}$$

The peak area A_i corresponding to a transition with energy difference E_i is the main quantity extracted from the measured energy spectra. It represents the number of events registered in a detector with a total efficiency ϵ_{tot}. The peak area can be expressed in terms of the integrated cross-section $I_{j\to k}$:

$$A_i = N_T \cdot \epsilon_{tot}(E_i) \cdot N_\gamma \cdot I_{j\to k}(E_i) \cdot W_{eff}(\theta, \varphi, \Delta\Omega)\,, \tag{2.8}$$

which is proportional to the number of target nuclei N_T illuminated by the photon beam with the number of photons N_γ, that are available for the reaction. The effective angular distribution of the emitted photons, averaged over the solid angle $\Delta\Omega$ covered by the detector, is taken into account via $W_{eff}(\theta, \varphi, \Delta\Omega)$. Equation (2.8) is essential for the analysis of NRF experiments, because it allows to directly determine the integrated cross-section from the measured peak areas, if all other quantities are known. Using the partial radiation widths the reduced transition probabilities or transition strengths for electric and magnetic transitions are calculated according to [74]:

$$B(E1)\uparrow = 9.554 \cdot 10^{-4} \cdot g \cdot \frac{\Gamma_0}{E_\gamma^3} \tag{2.9}$$

$$B(M1)\uparrow = 8.641 \cdot 10^{-2} \cdot g \cdot \frac{\Gamma_0}{E_\gamma^3} \tag{2.10}$$

For the calculation of these quantities a precise knowledge of the branching ratios Γ_i/Γ is of paramount importance. Section 2.2 covers the theory of angular distributions and correlations to determine W_{eff}. The analysis chapter covers techniques to determine the detector efficiency (see Section 4.1.3) and the number of photons (see Section 4.1.6).

2.2 Angular distributions of emitted photons

In the NRF equation (2.8) the angular distribution of the photons emitted in the decay of an excited state has to be taken into account. When two photons are

detected in coincidence it is necessary to correctly treat the associated angular correlations. The generic theoretical basis of angular distribution and correlation of γ-rays is thoroughly described by R. M. Steffen and K. Alder in [75]. At first the main building blocks for the basic theory are reproduced in an abbreviated fashion to introduce the necessary concepts, but for a complete derivation of the expressions the lecture of Ref. [75] is recommended. From these basic concepts a theoretical description of the distributions and correlations encountered in the γ^3 experimental setup was derived as part of this work.

2.2.1 Generic formalism

The generic formalism treats the emission of photons as the evolution of a final-state density matrix $\langle\varphi|\rho|\varphi'\rangle$ which represents an ensemble of N sub-states. Each sub-state must exhibit a sharp angular momentum J and in general the basis states can be chosen such that ρ is a diagonal matrix. For the case of a pure state (i.e. only a single sub-state is populated) ρ reduces to a matrix with a single diagonal value. In contrast, an initially random state, where all sub-states are equally populated, is represented by a diagonal matrix $\rho = \frac{1}{N}\mathbb{1}$, where all sub-states are uniformly populated.

Emission of a single radiation

The process of radiation emission is described by the transition from an initial-state density matrix

$$\langle J_i m_i|\rho|J_i m_i\rangle$$

to a final-state density matrix

$$\langle \mathbf{p}\tau J_f m_f|\rho(\infty)|\mathbf{p}\tau J_f m_f\rangle \ .$$

Here J_i and m_i are the angular momentum and magnetic quantum number of the initial state, and J_f and m_f the respective quantum numbers for the final state. Momentum (and direction of emission) and helicity of the emitted radiation are denoted by $\mathbf{p}$ and τ. The angular momentum states $|jm\rangle$ transform under rotation of the quantisation axes from one system S to another $\bar{S}$ according to

$$|j\bar{m}\rangle_{\bar{S}} = \sum_m |jm\rangle_S \, D^{(j)*}_{m\bar{m}}(S \to \bar{S}) \tag{2.11}$$

using the Wigner-D-matrix $D^{(j)*}_{m\bar{m}}$ that defines the rotation. The rotation is needed to express the observation of emitted radiation in a direction different from the original orientation direction of the state. Any density matrix transforms under a rotation of the reference frame according to

$$\rho(j_1 j_2)_{\bar{S}} = D^{(j_1)*\dagger}(S \to \bar{S})\rho(j_1 j_2)_S D^{(j_2)*}(S \to \bar{S}) \tag{2.12}$$

with the shorthand notation $\rho(j_1 j_2) = \langle j_1 m_1 | \rho | j_2 m_2 \rangle$.

It is possible to express the density matrix of any state in terms of a statistical tensor that contains the equivalent amount of information, and in addition exhibits simpler transformation properties:

$$\rho_q^\lambda(j_1, j_2) = \sum_{m_1} (-1)^{j_1 + m_1} \langle j_1 - m_1 j_2 m_2 | \lambda q \rangle \langle j_1 m_1 | \rho | j_2 m_2 \rangle \tag{2.13}$$

The tensor rank λ is an integer and can vary between $|j_1 - j_2|$ and $|j_1 + j_2|$. The subscript q denotes the q-th component of the tensor of a specific rank λ. The Clebsch-Gordan coefficients $\langle j_1 - m_1 j_2 m_2 | \lambda q \rangle$ originate from the series expansion of the product of Wigner-D-matrices.

The emission process is modelled using the time dependence of the density operator $\rho_{op}(t)$. Using first-order perturbation theory the final-state density can be obtained in the limit of $t \to \infty$. From the final-state density the final-state statistical tensor can be obtained (see Equ. 12.174 in [75]):

$$\begin{aligned} \langle \tau | \rho_{q_f}^{\lambda_f}(J_f, \mathbf{p}) | \tau' \rangle = \frac{d\Omega}{8\pi\lambda_\gamma} \sum_{\lambda_1 \lambda q_1 q L L'} & (-1)^{\lambda_1 - q_1} (2\lambda + 1)^{1/2} \left(\frac{2J_i + 1}{2J_f + 1} \right)^{1/2} \\ & \times \begin{pmatrix} \lambda_f & \lambda & \lambda_i \\ q_f & q & -q_i \end{pmatrix} \rho_{q_i}^{\lambda_i}(J_i) D_{q\mu}^{(\lambda)*}(\mathbf{e_z} \to \mathbf{k}) [\gamma(EL) + \tau\gamma(ML)] \\ & \times [\gamma^*(EL') + \tau'\gamma^*(ML')] \frac{\begin{pmatrix} L & L' & \lambda \\ \tau & -\tau' & \mu \end{pmatrix}}{\begin{pmatrix} L & L' & \lambda \\ 1 & -1 & 0 \end{pmatrix}} F_\lambda^{\lambda_f \lambda_i}(LL' J_f J_i). \end{aligned} \tag{2.14}$$

Here the generalised F-coefficients $F_\lambda^{\lambda_f \lambda_i}$ and the multipole transition amplitudes $\gamma(\pi L)$ are used. The generalised F-coefficients are tabulated for example in the Appendices of [76]. The six parameter symbols in round brackets are the Wigner-3j-symbols. This equation is very general and imposes no restrictions on either the initial or the final state, or the type of radiation. It describes the states formed after the emission of a γ-quantum of helicity τ and momentum $\mathbf{p}$ into a solid angle $d\Omega$.

Angular distribution of a single emitted photon

Figure 2.1 introduces the coordinate system for the following part. Radiation directions are denoted with $\mathbf{k_i}$, with the associated angles θ_i and φ_i with respect to $\mathbf{k_0}$. The probability of detecting the radiation in a direction $\mathbf{k}$ with a detector, that is described by an efficiency matrix $\epsilon(Q)$, is given by:

$$W(\mathbf{kQ}) = \sum_{\tau\tau'} \langle \tau | \rho_0^0(J_f) | \tau' \rangle \langle \tau' | \epsilon(Q) | \tau \rangle (2J_f + 1)^{1/2}. \tag{2.15}$$

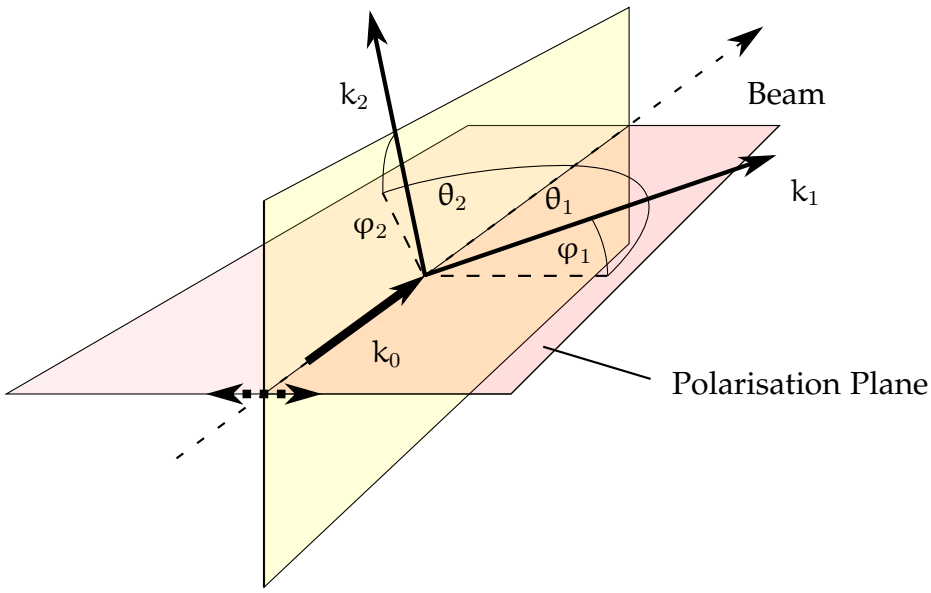

Figure 2.1: The coordinate system used for the description of angular distributions.

The efficiency matrix models the detection efficiency for the different helicity components of the radiation. For the present case $\epsilon(Q)$ is a diagonal matrix, because the detectors used in the experiment are not polarisation sensitive, and respond to both helicities in the same manner. This allows to set $\epsilon(Q)$ to the identity matrix, and handle the efficiency externally. Therefore, using (2.14) in (2.15) and setting $\epsilon(Q) = \mathbf{I}$, the directional distribution function for the emission of a single γ-ray from an initial state described by $\rho^{\lambda}_{q}(J_i)$ is given by:

$$W(\theta_1, \varphi_1) = \frac{d\Omega}{2\sqrt{\pi}} \sum_{\lambda q} (2J_i + 1)^{1/2} \rho^{\lambda}_{q}(J_i) A_{\lambda}(\gamma) (2\lambda + 1)^{-1/2} Y^{*}_{\lambda q}(\theta_1, \varphi_1). \qquad (2.16)$$

For this specific case a number of simplifications could be performed. Most notably it is possible to express the D-matrices using spherical harmonics $Y_{\lambda q}$, the Wigner-3j-symbols reduce to unity, and the ordinary angular distribution coefficients $A_{\lambda}(\gamma)$ have been introduced to take care of the properties of the emitted radiation. The $A_{\lambda}(\gamma)$ are defined as:

$$A_{\lambda}(\gamma) = \sum_{LL'\pi\pi'} F_{\lambda}(LL'J_f J_i) \gamma(\pi L) \gamma^{*}(\pi' L') \Bigg/ \sum_{L\pi} |\gamma(\pi L)|^2 \ , \qquad (2.17)$$

and contain the ordinary F-coefficients F_{λ}, which are usually tabulated along with the generalised F-coefficients. When the emitted radiation is a mixture of two multipoles, the multipole (amplitude) mixing ratio $\delta(\gamma) = \gamma(\pi' L + 1)/\gamma(\pi L)$ can be used, and the angular distribution coefficients reduce to a simpler form:

$$A_{\lambda}(\gamma) = \frac{F_{\lambda}(LLJ_f J_i) + 2\delta(\gamma) F_{\lambda}(LL'J_f J_i) + \delta^2(\gamma) F_{\lambda}(L'L'J_f J_i)}{1 + \delta^2(\gamma)}. \qquad (2.18)$$

Angular correlation of two photons emitted in succession

From Equ. (2.14) the final-state statistical tensor $\rho^{\lambda 1}_{q1}(J_1, \mathbf{p_1})$ after the emission of a single radiation γ_1 is calculated. For the emission of a second radiation γ_2 from the state described by this tensor into the direction $\mathbf{k_2}$ and solid angle $d\Omega_2$, the same equation (2.14) has to be applied a second time. Using $\rho^{\lambda 1}_{q1}(J_1, \mathbf{p_1})$ as the initial state, $\rho^{\lambda 2}_{q2}(J_2, \mathbf{p_1}, \mathbf{p_2})$ will be obtained. The general form of this expression is quite complex and a reproduction would not add much value to this derivation. However, under the assumptions that the nuclear states have perfect parity (as opposed to a mixing of two or more parities) and that only the directional correlation between the two emitted γ-rays is observed, a simplified, yet still sufficiently generic form, can be obtained:

$$W(\theta_1\varphi_1\theta_2\varphi_2) = \frac{d\Omega_1\, d\Omega_2}{4\pi} \sum_{\substack{\lambda_0 q_0 \lambda_1 q_1 \lambda_2 q_2 \\ \lambda_1,\lambda_2=\text{even}}} (-1)^{\lambda_1+\lambda_2}(2J_0+1)^{1/2}\rho^{\lambda_0}_{q_0}(J_0)A^{\lambda_2\lambda_0}_{\lambda_1}(\gamma_1) \times A_{\lambda_2}(\gamma_2)\begin{pmatrix}\lambda_2 & \lambda_1 & \lambda \\ q_2 & q_1 & q\end{pmatrix}(2\lambda_2+1)^{-1/2}Y_{\lambda_1 q_1}(\theta_1\varphi_1)Y_{\lambda_2 q_2}(\theta_2\varphi_2). \tag{2.19}$$

The sums over λ_i run only over even integers from 0 to 4, if only the absorption and emission of photons is concerned. The subscripts q_i are in the range $[-\lambda_i, \lambda_i]$. J_0 is the initial angular momentum preceding the decay.

2.2.2 Emission of photons following excitation with linearly polarised radiation

Equations (2.16) and (2.19) are useful for the description of the emission processes in the reactions studied with the γ^3 setup. Their counterparts in [75] are Equations (12.186) and (12.204). In the following a specialised version for the initial state is defined, such that the angular distributions and correlations can be calculated. At the HIγS facility the target is irradiated by a linearly polarised photon beam. A nucleus that initially occupies a randomly oriented state absorbs a polarised photon from the beam and is excited to an aligned state with higher energy. If the direction of the photon beam $\mathbf{k_0}$ is along the z-axis of the laboratory system, the initial-state statistical tensor $\rho^{\lambda_0}_{q_0}(J_0)$ has the following form (Equ. (12.271) in [75]):

$$\rho^{\lambda_0}_0(J_0) = (2J_0+1)^{-1/2}B_{\lambda_0}(\gamma_0) \tag{2.20}$$

$$\rho^{\lambda_0}_{\pm 2}(J_0) = (2J_0+1)^{-1/2}B_{\lambda_0,2}(\gamma_0) \tag{2.21}$$

with the parameters $B_\lambda(\gamma)$ and $B_{\lambda,2}(\gamma)$ defined for the general case of a possibly mixed radiation γ as:

$$B_\lambda(\gamma) = \sum_{LL'\pi\pi'} (-1)^{L+L'} \gamma(\pi L)\gamma^*(\pi' L') F_\lambda(LL'J_0J) \Bigg/ \sum_{L\pi} |\gamma(\pi L)|^2 \tag{2.22}$$

$$B_{\lambda,2}(\gamma) = -\frac{1}{2} \frac{\sum_{LL'\pi\pi'} (-1)^{L+L'} \frac{\begin{pmatrix} L & L' & \lambda \\ 1 & 1 & -2 \end{pmatrix}}{\begin{pmatrix} L & L' & \lambda \\ 1 & -1 & 0 \end{pmatrix}} (-1)^\sigma F_\lambda(LL'J_0J)\gamma(\pi L)\gamma^*(\pi' L')}{\sum_{L\pi} |\gamma(\pi L)|^2} \tag{2.23}$$

Where J_0 is the angular momentum of the initially random state, and J is the corresponding angular momentum of the state populated by the absorption of a linearly polarised photon with angular momentum difference L and parity difference π. The parameter σ depends on the character of the radiation and is equal to 0 for an electric transition or 1 for a magnetic transition. The B parameters reduce to simpler expressions for the case of unmixed radiation ($\delta = 0$). Then $L = L'$ and the sums vanish.

$$B_\lambda(\gamma) = F_\lambda(LLJ_0J) \tag{2.24}$$

$$B_{\lambda,2}(\gamma) = -\frac{1}{2}(-1)^\sigma \frac{\begin{pmatrix} L & L & \lambda \\ 1 & 1 & -2 \end{pmatrix}}{\begin{pmatrix} L & L & \lambda \\ 1 & -1 & 0 \end{pmatrix}} F_\lambda(LLJ_0J) \tag{2.25}$$

With the such defined initial state it is possible to further simplify Equation (2.16). The spherical harmonics reduce to Legendre polynomials $P_\lambda, P_\lambda^{(2)}$ and the angular distribution function can be written as:

$$W(\theta,\psi) = \frac{d\Omega_1\, d\Omega_2}{32\pi^2} \sum_\lambda A_\lambda(\gamma_1) \tag{2.26}$$

$$\times \left[B_\lambda(\gamma_0) P_\lambda(\cos\theta) + 2B_{\lambda,2}(\gamma_0) \left[\frac{(\lambda-2)!}{(\lambda+2)!}\right]^{1/2} P_\lambda^{(2)}(\cos\theta)\cos 2\psi \right] \tag{2.27}$$

Here the angle φ has been substituted by the angle ψ to denote the angle between the polarisation direction and the observed radiation. Equation (2.19) on the other hand does not simplify easily with the specific initial-state tensor and therefore has to be used as written above.

2.2.3 Example distributions

The angular distributions shown in Figure 2.2 constitute some of the cases encountered in the analysis of data from the γ^3 setup. In most cases $J = 1^\pi$ states are excited, which is why only such distributions are displayed here. Also only the case of an even-even nucleus (i.e. $J_0^\pi = 0^+$) is considered in the following.

Examples (a) and (b) display the distributions for the decay of an $J = 1^-$ and an $J = 1^+$ state back to the J_0^π ground state, respectively. It is clearly visible that detectors placed at positions $(\pi/2, \pi/2)$ and $(\pi/2, 0)$ will allow to separate between the two cases with a large sensitivity. This property has been used in past experiments to determine parities at the HIγS facility [8, 9]. Examples (c) and (d) illustrate that in the case of a decay from $J = 1^\pi$ states to a 2^+ state the distribution is almost isotropic, such that this transition is much less sensitive to the parity. The last two examples (e) and (f) show that in a two-step cascade the distribution of the second γ-ray depends strongly on the direction of the first emitted photon. In example (e) the first photon is detected at $(\theta_1, \varphi_1) = (\frac{\pi}{2}, \frac{\pi}{2})$, while in example (f) the first photon is detected at a perpendicular angle $(\theta_1, \varphi_1) = (\frac{\pi}{2}, 0)$. These examples show that it is important to take into account the correct angular distribution not only for the analysis of the singles data, but especially for the γ-γ-coincidences.

2.3 Spectrum unfolding

Usually, the energy spectrum f measured with a detector can be described as the convolution of an underlying *true* spectrum g with the detector response function h

$$f = (g * h) + \epsilon \,, \tag{2.28}$$

where a small perturbation ϵ is usually present due to finite statistical errors. The technique of extracting the underlying spectrum from a measured spectrum with a known or unknown detector response function is commonly called *spectrum unfolding* or *deconvolution*. This involves an algorithmic process that can either be deterministic or of statistical nature (depending on the knowledge of h), and is either applied straight-forward or iteratively by minimising a cost function. Two fundamentally different techniques are briefly introduced here, which will be applied to the measured spectra as described in Section 4.1.1. Both methods assume that the measured spectra are available as a histogram of discrete energy bins E_i. The detector response function must be known as well and is assumed to be available as a set of energy spectra with the same bin width as the measured spectra and for each energy E_i. These response functions can for example be obtained using Monte-Carlo simulations.

Figure 2.3 shows three such detector response functions simulated with different photon energies for HPGe detectors. They have been normalised in order to correctly represent the detector efficiency at the energy of the full-energy peak. The typical structure of the detector response can be seen. The different parts of the detector response originate from the different processes for the electromagnetic interaction. The three major processes are the photoelectric absorption of the photon, Compton scattering, and pair production [77, 78]. In the photoelec-

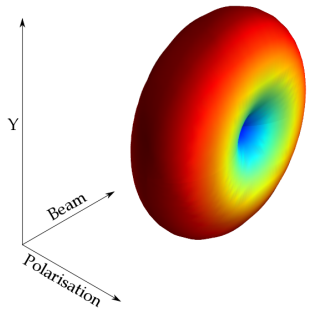

(a) $0^+ \to 1^- \to 0^+$

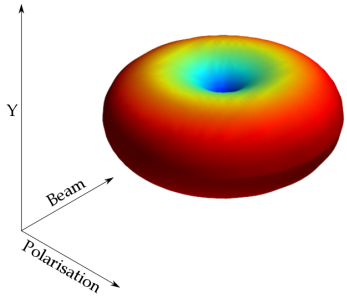

(b) $0^+ \to 1^+ \to 0^+$

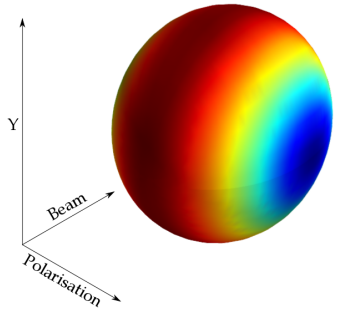

(c) $0^+ \to 1^- \to 2^+$

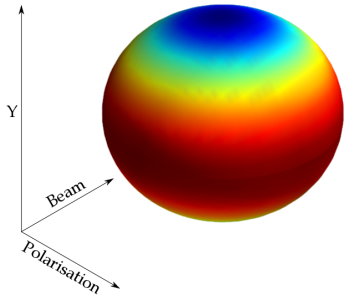

(d) $0^+ \to 1^+ \to 2^+$

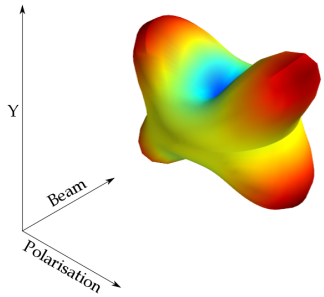

(e) $0^+ \to 1^- \to 2^+ \to 0^+$, $(\theta_1, \varphi_1) = (\frac{\pi}{2}, \frac{\pi}{2})$

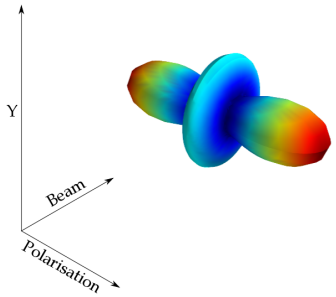

(f) $0^+ \to 1^- \to 2^+ \to 0^+$, $(\theta_1, \varphi_1) = (\frac{\pi}{2}, 0)$

Figure 2.2: Example angular distributions of emitted photons after absorption of linearly polarised radiation. The colours indicate the absolute value of the angular distribution from blue (small values) to red (large values).

tric absorption the complete energy of the photon is absorbed. This leads to the full-energy peak at the highest energy in the spectrum. In the Compton scattering process the photon interacts with the electron shell of the nucleus, and loses only a fraction of its energy. This produces the continuous distribution along the low energy part of the spectrum. At a photon energy above 1.022 MeV the pair production process is possible, where the photon is converted into an electron-positron pair. These two particles share the excess photon energy equally. The positron usually annihilates with another electron in the detector medium and produces a pair of 511 keV photons. In the case that one or both of these photons are not detected, then the total energy deposited in the detector will be smaller by that amount. This leads to the formation of single and double escape peaks below the full-energy peak. At high energy (in the spectra shown in Fig. 2.3 at > 5 MeV) the single and double escape peaks are more prominent than the full-energy peak, because pair production is the dominant process, and the detector efficiency is not high enough to detect the pair of photons.

2.3.1 Top-Down unfolding

The first simple method is the so-called Top-Down unfolding method. This method is only applicable, if the detector response function $h(E_i)$ for a certain energy bin E_i has no contribution at any energy above this energy. As can be seen in Figure 2.3 for the present case of γ-ray detectors, clearly no such contribution is present. If the complete set of detector response functions is regarded as a square matrix $\mathbf{H}$ with entries $H(E_i, E_j)$, then this matrix is triangular. The unfolding algorithm proceeds as follows: A starting energy E_i is selected at the top of the spectrum. The detector response function corresponding to this energy $h(E_i)$ is scaled with a scaling factor s, such that the amount of counts in the full-energy peak of the detector response equal the counts in the spectrum at the starting energy. The scaling factor s is the unfolding result for this energy E_i. In the actual unfolding step the scaled detector response is subtracted bin-by-bin from the original spectrum. For the next iteration the next lower energy bin with energy $E_{(i-1)}$ is selected and the process is repeated until the lowest bin is reached.

The successive application of this algorithm is shown in Figure 2.4. The upper part shows the high energy part of a measured $LaBr_3$:Ce spectrum with the full-energy peaks (FEP), the single escape (SE) and the double escape (DE) peaks. This spectrum is now modified by the above algorithm. The lower part of the figure shows the unfolding result at intermediate stages. The energy range that was already unfolded is indicated with a shaded region. When the algorithm is finished, the unfolding result is complete (bottom part of the figure). One drawback of this algorithm is that it allows negative bin counts in the unfolding result, which is non-physical. Such an 'undershoot' region can be seen at around

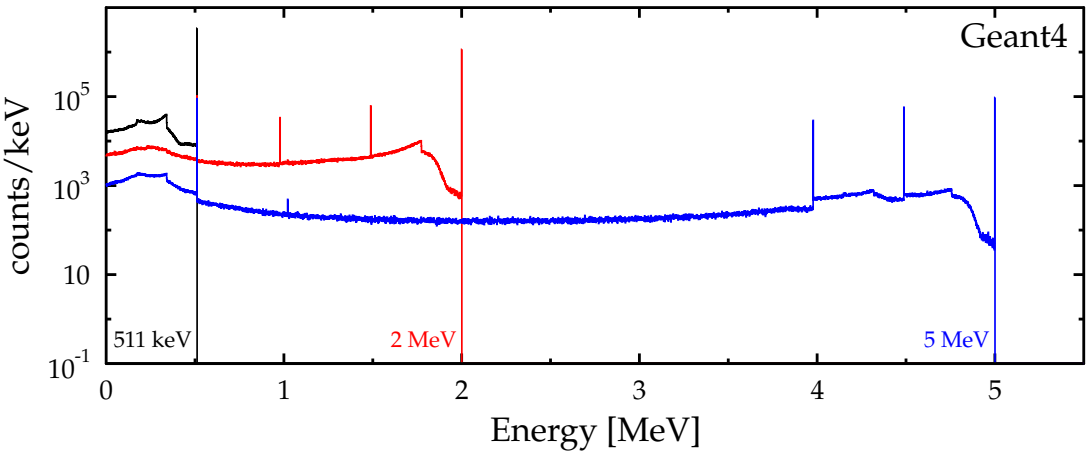

Figure 2.3: Simulated detector response spectra corresponding to incident photon energies of 511 keV, 2000 keV and 5000 keV. The shape of the detector response and especially the FEP/SE ratio changes as a function of the energy.

5.1 MeV. This is a result of the statistical fluctuations present in the measured spectrum, which lead to a different ratio of the full-energy peak to the rest of the spectrum as assumed in the simulated detector response function. For most of the cases this effect is negligible, or can instead be used as an indication for incorrect energy calibration (see Section 4.1.2).

2.3.2 Gold unfolding method

The second method is a variation of the Van-Cittert algorithm [79] with a specific choice of the regularisation parameter μ. This method is called the Gold unfolding method [80] after the inventor R. Gold, and has the advantage that the resulting spectrum has only positive entries. The algorithm has been improved by M. Morháč *et al.* [81] and incorporated in the ROOT analysis framework [82] as part of the `TSpectrum` class. The applicability to nuclear spectroscopy data using simulated detector response functions is shown in [83]. The underlying approach of the Gold unfolding algorithm is different from the Top-Down method in several aspects: The algorithm is iterative and therefore has no single solution, but can converge towards a result that minimises a special cost function. This cost function is given by

$$f = ||\mathbf{H}\hat{x} - y||^2 + \mu||\mathbf{Q}\hat{x}||^2 \tag{2.29}$$

with the transfer function (detector response) in the form of the matrix $\mathbf{H}$, the assumed solution $\hat{x}$, the regularisation parameter μ and the measured spectrum $y = \mathbf{H}\hat{x}$. The matrix $\mathbf{Q}$ is a square Toeplitz type matrix[1], and in the Gold algo-

[1] In a Toeplitz matrix the entries Q_{ij} depend only on the difference of $i - j$

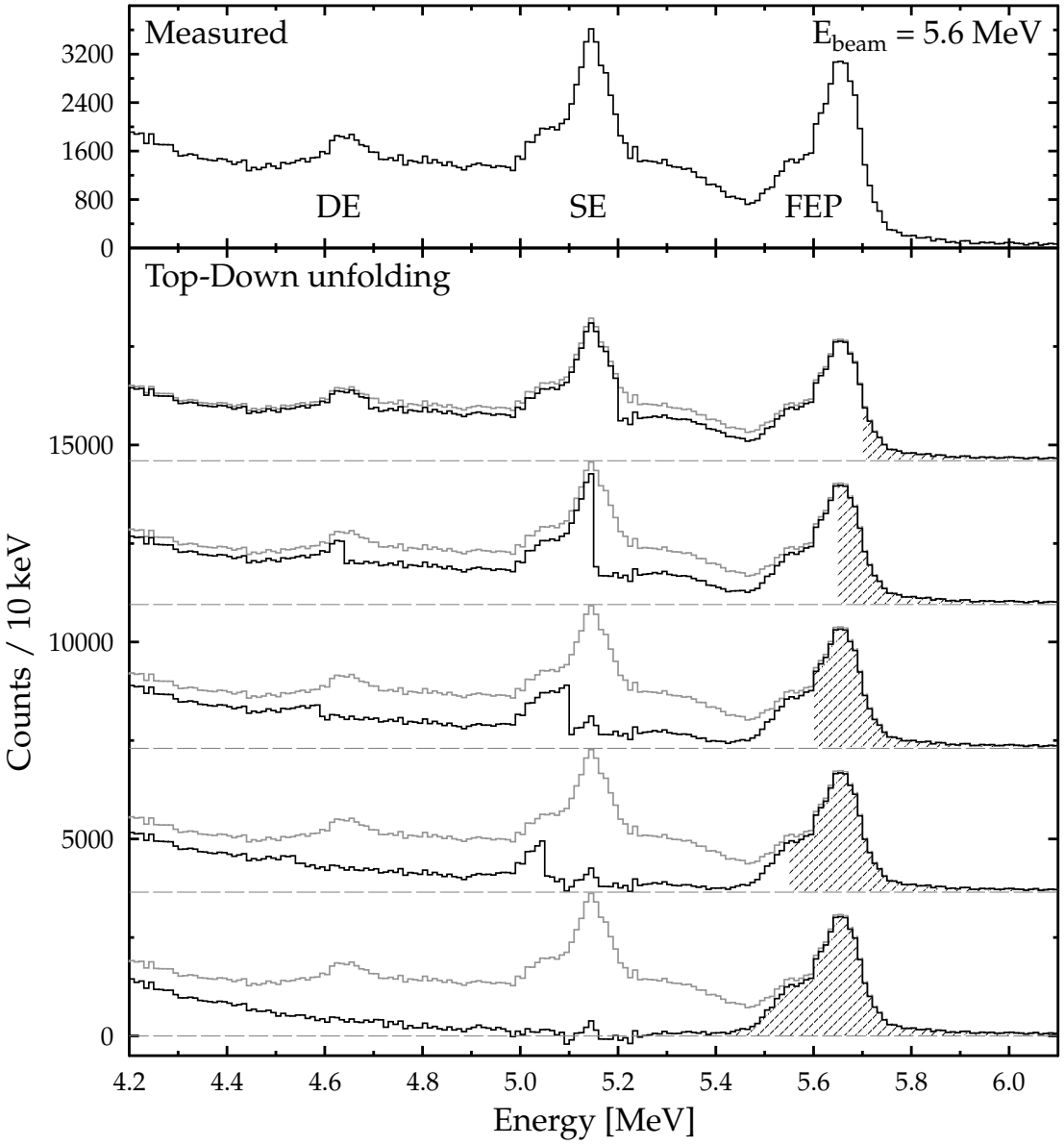

Figure 2.4: The Top-Down Unfolding algorithm applied to a $LaBr_3$:Ce spectrum measured with ^{140}Ce target at 5.6 MeV beam energy. The lower part shows the stepwise unfolding procedure. The shaded area marks the energy bins that have already been taken into account.

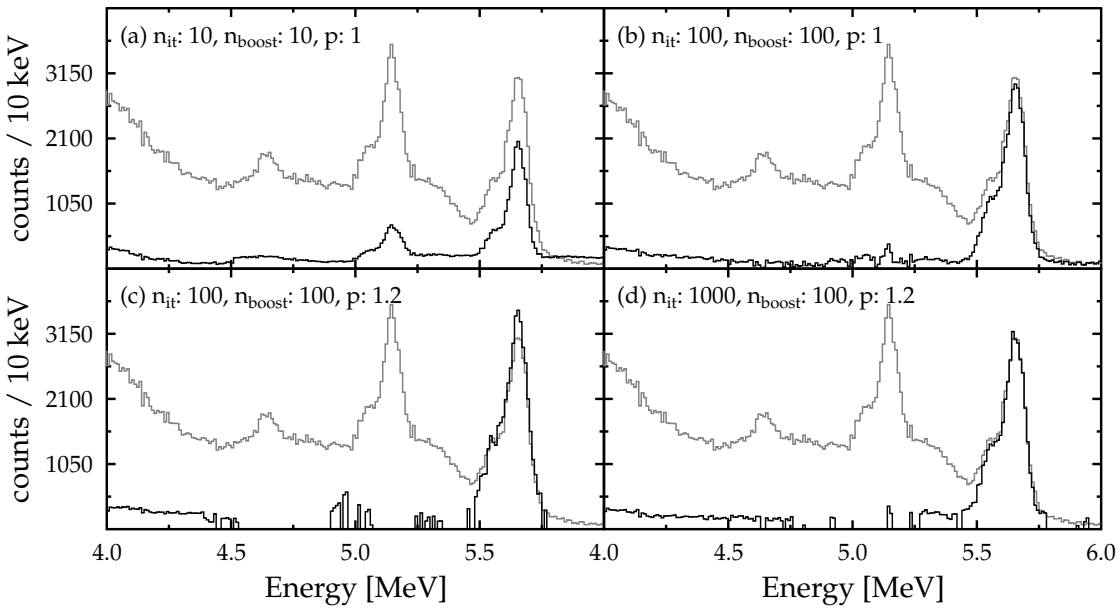

Figure 2.5: The Gold unfolding algorithm applied to the same spectrum as in Fig. 2.4 with different control parameters: The number of iterations (n_{it}), the number of repetitions (n_{boost}) and the boost exponent (p) are varied. The parameters from (d) have been used in the analysis. The original spectrum is shown in grey.

rithm the product $\mathbf{H}^T\mathbf{H}$ is used. This is a special case of Tikhonov regularisation [84]. The regularisation parameter μ controls the importance of the norm of the vector $\hat{x}$ in the cost function. A higher value of μ prefers solutions to the problem with smaller norms. The solution to this problem is found by inverting the matrix $\mathbf{H}$. This can not be done directly, because $\mathbf{H}$ is in most cases almost singular (ill-conditioned) and the direct inversion can not lead to a stable solution. Therefore an inverse for $\mathbf{H}$ must be found in an iterative way including a method of regularisation

$$x_i^{(n+1)} = x^{(n)} + \mu[\mathbf{H}^T y - \mathbf{H}^T\mathbf{H}x^{(n)}]\,, \tag{2.30}$$

the Van-Cittert algorithm. The Gold algorithm makes use of a special local choice of μ depending on the index i, such that its components are fixed to

$$\mu_i = \frac{x_i^{(n)}}{\sum_{m=0}^{M-1} \mathbf{Q}_{im} x_m^{(n)}} \tag{2.31}$$

for the n-th iteration of the algorithm and with the abbreviation $\mathbf{H}^T\mathbf{H} = \mathbf{Q}$. The iteration rule for the algorithm thus becomes

$$x_i^{(n+1)} = \frac{y_i}{\sum_{m=0}^{M-1} \mathbf{Q}_{im} x_m^{(n)}} x_i^{(n)} \tag{2.32}$$

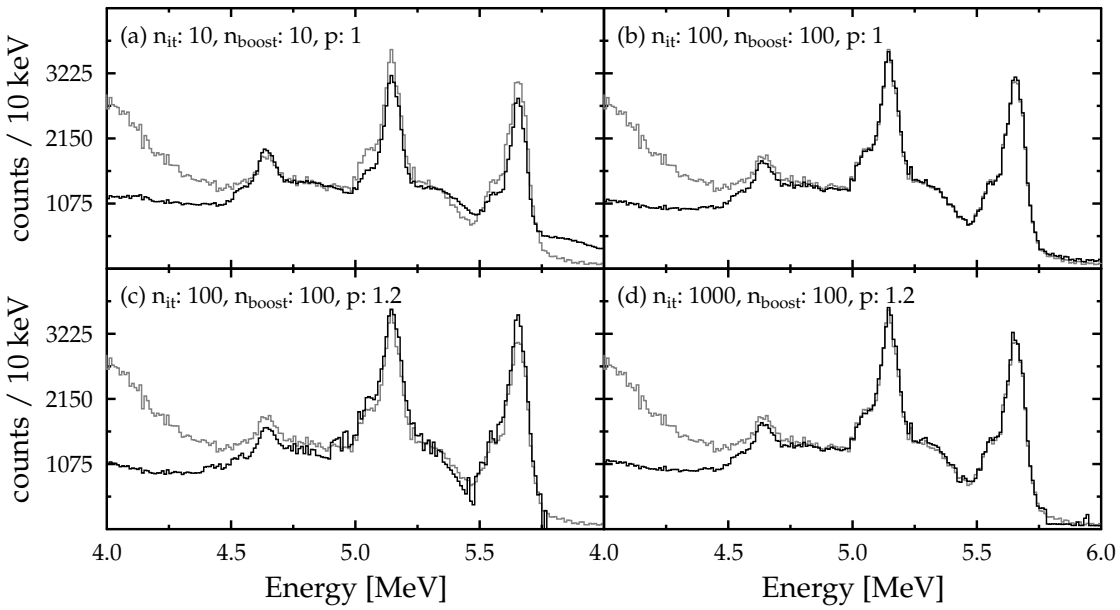

Figure 2.6: The Gold unfolded spectra from Fig.2.5 are again folded with the detector response. These refolded spectra are shown together with the original spectrum (grey) for comparison.

To avoid converging to a local minimum, an additional boosting operation can be performed after initial convergence, which raises each bin count in the result to the power p, called the boosting coefficient

$$x_i^{(0)} = [x_i^{(L)}]^p \tag{2.33}$$

which serves as the initial solution for the next convergence cycle. This alternating pattern of boosting and converging can be repeated several times until a suitable solution is found.

The part of the spectrum at high energy, which is of importance for the analysis, is comparatively small with regard to the complete spectrum. The cost function that is minimised is a global quantity instead. Applying the Gold method to the complete spectrum leads to a poor unfolding result, because the high energy region only adds a small contribution to the cost function. To improve the results, the Gold method is only applied to the high energy region including the FEP, SE, and DEP region of the spectra.

In Figure 2.5 a few unfolding results after applying the Gold algorithm to the same spectrum as in Figure 2.4 in the energy range from 4 MeV to 7 MeV are shown. The number of iterations n_{it} and the number of boosts n_{boost} are varied to show the effect on the unfolding result. Too few iterations (a) do not result in a converged unfolding result. Contributions from the single escape are still present in the spectrum. Without boosting (i.e. $p = 1$) the result visually

resembles the solution that would be obtained from the Top-Down unfolding method (b). Boosting leads to a concentration of the bin contents in fewer bins and reduces the noise in the spectrum (c). Increasing the number of iterations to 1000 produces the unfolding result shown in (d).

The quality of the unfolding result can be judged by folding it again with the detector response. This *refolded* spectrum is then compared to the initial one. Figure 2.6 shows these refolded spectra for the same cases as in Fig. 2.5. Clearly the closest match between the original spectrum and the refolded spectrum is obtained with the parameters from (b) and (d). Consistently good results over the whole energy range are achieved with the parameters from (d). Therefore this set of parameters was used in the analysis.

Regarding the two different unfolding methods, no clear decision as to which one performs better on the given data can be made. Both algorithms perform equally well and produce a good unfolding result. The Gold method has the advantage of always producing a spectrum that contains only positive entries. The advantage of the Top-Down approach is that no parameters have to be adjusted. Due to their fundamentally different nature both methods are used in the data analysis, in order to perform cross-checks.

Chapter 3

Experimental Setup

The following chapter describes the details of the experimental setup, which has been implemented within this work and used to take the data analysed in chapter 4. At first an overview of the High Intensity γ-ray Source (HIγS) [10] at the Triangle Universities Nuclear Laboratory (TUNL) will be given, followed by an in-depth description of the new γ^3 setup. The layout of the electronics and the data acquisition system are described as well as the main systems for additional diagnostic measurements, for instance target alignment and photon beam energy. The last section contains information about important differences of the setup introduced in between the two beam times in 2012 and 2013.

3.1 The HIγS facility at TUNL

The HIγS facility is located at TUNL and delivers a highly polarised quasi-monoenergetic photon beam through the mechanism of laser Compton backscattering (LCBS) in a free electron laser (FEL) driven by the combination of an electron accelerator and a storage ring.

3.1.1 Production of a quasi-monoenergetic photon beam

An overview of the HIγS facility is shown in Fig. 3.1. The linear electron accelerator produces a bunched electron beam with energies in the range from

Table 3.1: Properties of the γ-ray beam at the target position at HIγS.

E_γ	1 – 100	MeV
N_γ	> 50	γ/eV/s
Energy resolution	0.8 – 10	%
Degree of polarisation	95	%

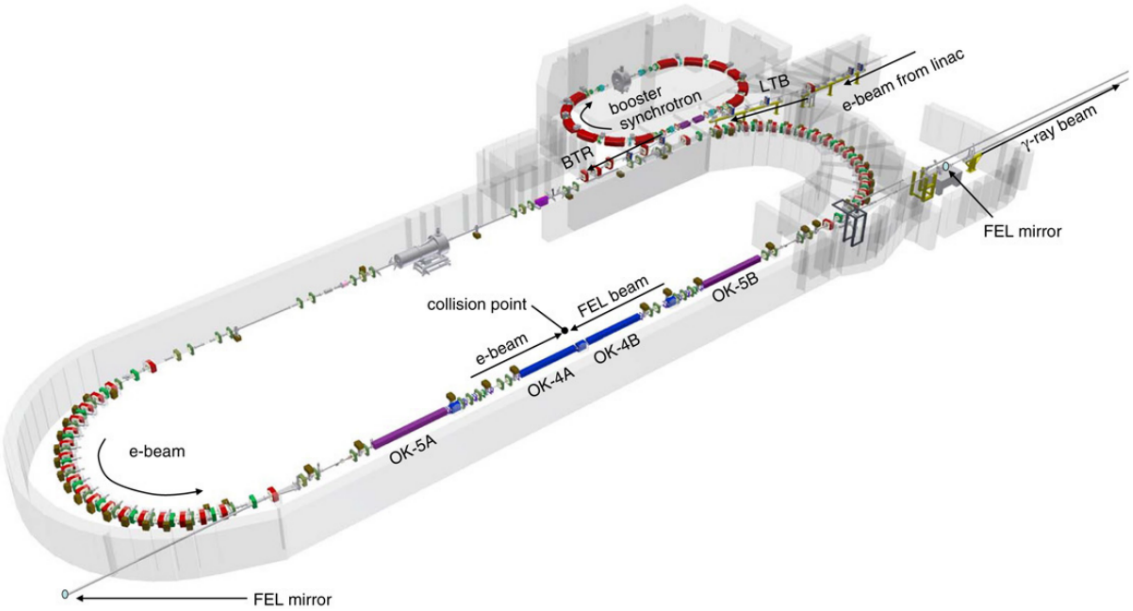

Figure 3.1: The HIγS facility at TUNL. Reprinted from [10], Copyright (2008), with permission from Elsevier.

180 MeV to 280 MeV, which is subsequently accelerated to energies ranging from 0.24 GeV to 1.2 GeV in the booster synchrotron. These electrons are injected into the storage ring which operates at an adjustable electron energy and a revolution frequency of about 2.79 MHz. One of the straight sections of the storage ring is equipped with wiggler magnets which together with a set of optical mirrors constitute a Free Electron Laser (FEL) that is capable of producing a linearly or circularly polarised beam of laser photons. The high-energy photon beam is produced by colliding these polarised laser photons and electrons in the storage ring at the collision point. This technique is called laser Compton back-scattering and has been used also at other facilities before [7, 85]. The intra-cavity production of the laser photons has certain advantages regarding alignment and synchronisation of the colliding beams, and allows to cover a wide range of beam energies. The polarisation of the laser photons is preserved during the scattering process such that the resulting high-energy photon beam is also linearly polarised to a degree in excess of 95 %. The storage ring is used for two main reasons: Most of the electrons from each bunch don't undergo a scattering process and can be reused in the next cycle. The use of the storage ring also allows much higher beam currents than what could be delivered from the linear accelerator itself, thus providing a much higher photon intensity. Current operation of the FEL allows to produce laser photons with an energy between 1.2 eV to 6.5 eV, which are boosted to an energy range of 1 MeV to 100 MeV after the Compton back-scattering process. From an electron beam current of up to 80 mA (LCBS operation) a high-energy photon flux of $> 10^9\,\gamma/\mathrm{s}$ can be achieved at the colli-

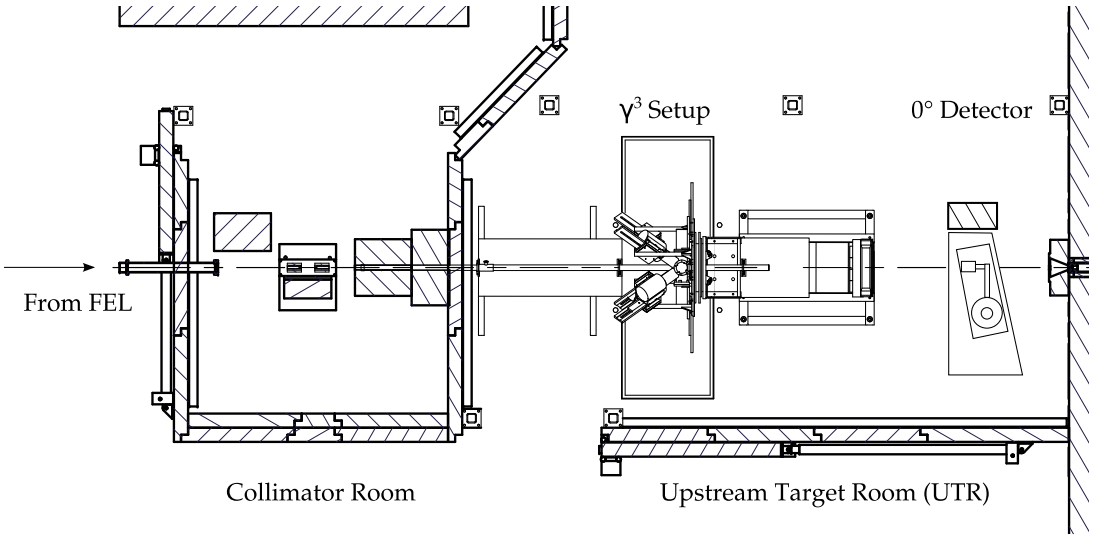

Figure 3.2: Overview of the γ^3 setup. The monoenergetic photon beam is delivered from the FEL (on the left), collimated to the appropriate size in the collimator room and hits the target in the centre of the γ^3 setup.

sion point. Since in a Compton scattering process the energy of the scattered particles depends on the scattering angle, it is necessary to collimate the photon beam in order to produce a beam with a narrow energy spread. Therefore a collimation system located 57.2 m from the collision point allows to narrow the beam diameter to sizes between 2 cm to 5 cm [86, 87]. The properties of the γ-ray beam at the target position are summarised in Table 3.1.

3.2 The γ^3 setup

The newly installed γ^3 detection system is located in the HIγS upstream target room (UTR) which is situated around 60 m from the collision point of the FEL. Figure 3.2 shows an overview of the complete experimental setup with the collimation room, the γ^3 detectors around the target position and the 0° detector. In this section the modifications to the existing NRF setup will be described in detail.

First photon scattering experiments at HIγS were carried out in 2002 by Pietralla *et al.* [8, 9] with an experimental setup consisting of four HPGe detectors. The four detectors with a relative efficiency of 60 % were arranged in a polarimetry geometry. Two horizontal detectors detected photons scattered in the plane of polarisation (see Fig.2.1), while two vertical detectors detected photons scattered in the perpendicular plane. All detectors were positioned at an azimuthal angle of $\theta = 90^\circ$. This arrangement has been used for various experi-

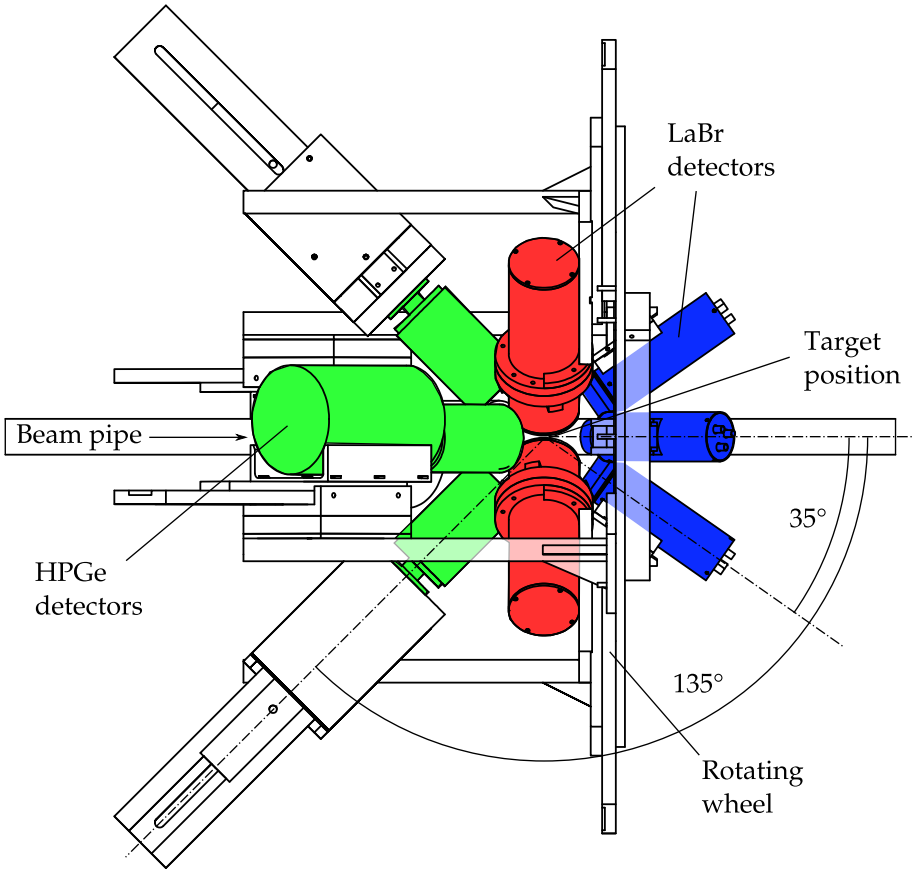

Figure 3.3: Detail drawing of the γ^3 setup. The various detectors are shown in colour: The backwards HPGe detectors in green, the 3" x 3" $LaBr_3$:Ce detectors at 90° in red, and the 1.5" x 1.5" $LaBr_3$:Ce detectors at 35°.

ments (see e.g. Refs. [10, 30, 31, 88]) making use of the excellent performance of the HIγS facility.

3.2.1 Modifications to the existing experimental setup

The existing experimental setup has been modified and extended to increase the photon detection efficiency. This makes the detection of two coincident γ-rays from a single nuclear decay viable and allows the measurement of the eponymous $(\gamma, \gamma'\gamma'')$ reaction. The additional detectors made substantial changes to the mechanical structure necessary. At the same time modifications to the beam pipe and detector shielding were made to allow a close geometry and improve the peak to background ratio in the measured energy spectra.

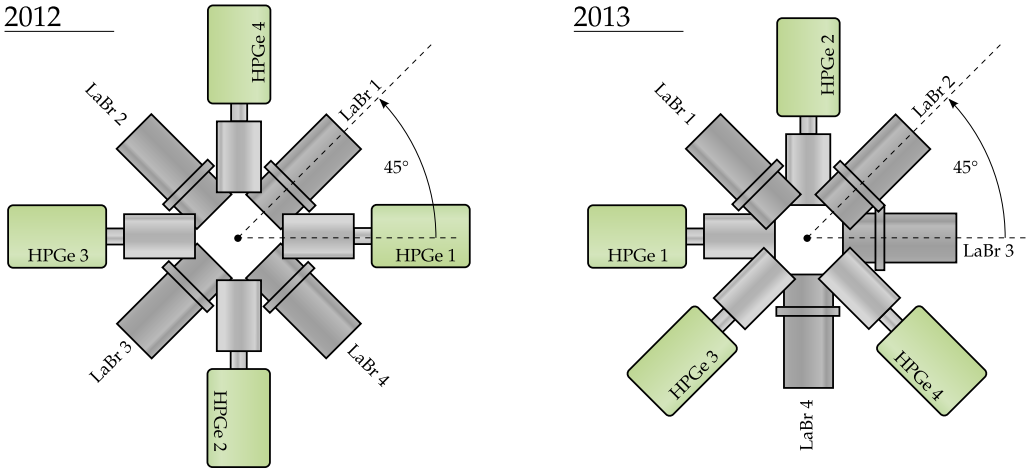

Figure 3.4: Schematic layout and naming convention for the detectors in 2012 and 2013. The direction of the beam points into the page. The complete detector array can be rotated by 45° counter-clockwise.

Detectors

In addition to the four HPGe detectors with high energy resolution, a set of four 3"x3" $LaBr_3$:Ce scintillators and four 1.5"x1.5" $LaBr_3$:Ce scintillators with high efficiency was installed in the detector array. Figure 3.3 shows a schematic drawing of the extended array, with the HPGe detectors shown in green and the $LaBr_3$:Ce detectors in red (3"x3") and blue (1.5"x1.5"). The 3"x3" $LaBr_3$:Ce detectors were read out using photo-multiplier tubes (PMT) of type R6233-100 SEL from Hamamatsu and active voltage dividers produced in-house following a design from the University Milan and INFN, Milan [89]. These active voltage dividers have already shown better performance in combination with $LaBr_3$:Ce detectors [90] compared to conventional designs. Other voltage divider layouts such as discussed in [91, 92] were also considered for this purpose, but the active voltage dividers promised the best performance. Two of the 1.5"x1.5" detectors were equipped with PMTs of type R9779 from Hamamatsu while the third one was read out using a Photonis model XB2020. For the experiments that took place in 2012 only three small $LaBr_3$:Ce detectors were available, such that in total 11 detectors were used. Due to the large amount of background detected in the small $LaBr_3$:Ce detectors, their contribution to the measurements was unfortunately limited. Therefore, in the following analysis the data from these detectors has not been used. In the 2013 experiments the small detectors have not been installed. Figure 3.4 shows the layout and naming scheme for the detectors in the setup as used in most of the experiments in 2012, and 2013.

The detection efficiency was measured using a calibration source (^{56}Co) in the energy range up to 3.6 MeV. Using the Monte-Carlo simulation framework GEANT4 [93], the detector geometry was recreated in detail, taking into ac-

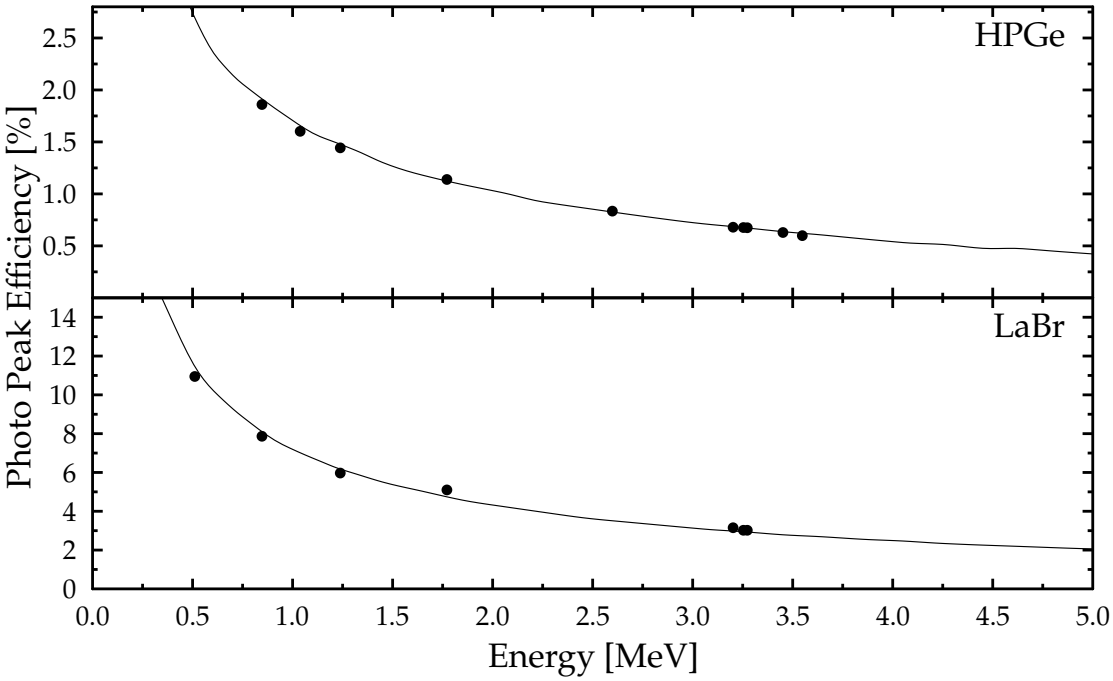

Figure 3.5: Total full energy peak efficiency of the γ^3 setup using the standard geometry shown in Fig. 3.3. Data points represent values measured with a calibration source (^{56}Co), the smooth curve shows data from a Monte-Carlo simulation (GEANT4 [93]).

count the measured detector positions. The measured and simulated detection efficiency of the two detector systems is shown in Fig. 3.5 as a function of the photon energy. Including a detailed geometry resulted in efficiency values very close to the measured values. Deviations from the data are attributed to uncertainties of detector positions.

Mechanical engineering

The experimental setup was moved about 2 m downstream from the original position to install a circular detector mount that allows the entire detector array to be rotated around the beam axis by an angle of up to $\Delta\phi = 45°$. The wheel has four detector positions each at a polar angle $\theta = 135°$ (backward), $\theta = 90°$ (middle) and $\theta = 45°$ (forward) with respect to the beam axis. Angular spacing between the positions is $90°$ for each polar angle. The middle detectors are rotated by $\phi = 45°$ around the beam axis with respect to the forward and backward detectors to minimise shadowing effects, and to maximise the solid angle coverage. Additional mounts for the forward detectors allow them to be installed at an angle of $90°$ as well to increase the sensitivity for measuring angular distributions. Custom parts for mounting all detectors on this wheel have been designed, such that both types of detectors could be mounted in any

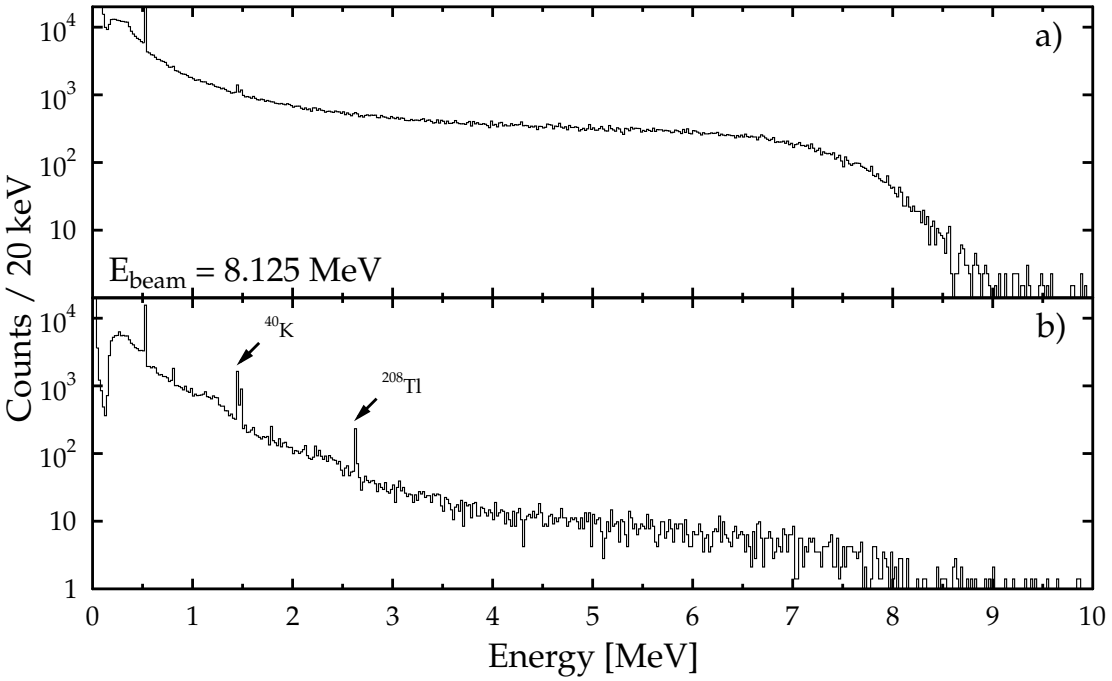

Figure 3.6: HPGe spectrum measured with and without air in the beam pipe. Both measurements were performed without scattering target: a) Measurement with air. b) Beam pipe is evacuated. All other conditions are the same. Background contributions in the critical energy range from 2 to 9 MeV have been reduced by at least one order of magnitude.

position interchangeably for maximum flexibility during the experiment. The main design challenge was to keep all detectors pointed directly at the target position while maintaining this flexibility.

A new transparent PVC beam pipe starting from the collimation system and extending beyond the target position with a smaller diameter compared to the existing one was designed and constructed. This allowed to move the detectors closer to the target and to increase the covered solid angle. Since $LaBr_3$:Ce detectors have been shown to operate well even at very high event rates [94], they can be placed very close to the target. Decreasing the diameter of the beam pipe from the former 9 cm to 5 cm allows a minimal distance to the target of 5 cm for the $90°$ detectors and of 8 cm for the $135°$ detectors.

Custom target holders that allow a precise alignment of the target inside the beam pipe were constructed as well. The amount of material at the target area was kept to a minimum, while the rear end of the target holder served as a self-closing vacuum seal for the beam pipe.

Evacuated beam pipe

The beam pipe was equipped with a vacuum pump to reach a medium vacuum with a pressure around 1 mbar to 10 mbar. The reduced number of air molecules leads to a longer mean free path length for the photons and greatly reduces the probability for atomic scattering processes. The effect of evacuating the beam pipe on the measured energy spectra is shown in Fig. 3.6. Here two spectra recorded without any NRF scattering target (“empty target") are shown. The measurements were done once with air at normal pressure in the beam pipe and once with an evacuated beam pipe under otherwise identical conditions at a beam energy of 8.125 MeV. The two spectra are normalised with respect to the measurement time. With air at normal pressure the contribution to the observed background events stemming from atomic scattering on air molecules is substantial over the whole energy range up to the beam energy. When the beam pipe is evacuated, this contribution is reduced by at least an order of magnitude in the energy range from 2 MeV to 9 MeV. This reduction is important for two main reasons: The count rate in the $LaBr_3$:Ce (HPGe) detectors is reduced from 1.4 kHz to 0.3 kHz (2.5 kHz to 0.25 kHz), resulting in a shorter dead-time for all detectors. With a reduction of the background the sensitivity for small peaks in the energy spectrum is increased, which can be seen from the peaks stemming from natural background (^{40}K and ^{208}Tl). All experiments within the scope of this dissertation have been carried out with an evacuated beam pipe.

Shielding

At several positions in the setup shielding material has been used to reduce background radiation. Directly behind the collimator the photon beam has to pass a 30 cm thick lead wall with a 5 cm hole for the beam pipe to stop all radiation scattered from the collimator. In between the wall and the experimental setup a second 15 cm wall was constructed to shield the detectors from the beam halo radiation originating from small angle scattering. Each detector face can be individually equipped with a combination of Cu, Cd and Pb *filter* discs to absorb low-energy γ-rays scattered from the target and reduce the count rate in the detectors. The thickness of these *filters* can be adjusted to match the conditions for each target and beam energy. The individual detectors are wrapped in a thin cylindrical layer of lead with 2 mm thickness to reduce scattering of reaction products from one detector into the active volume of the others. Additionally, a lead shield with 3.3 mm thickness can be placed around the beam pipe at the target position.

3.3 Data acquisition

The detector signals are digitised and recorded by two independent data acquisition (DAQ) systems. The Canberra GENIE 2000 system from the existing setup is used to record singles spectra (i.e. spectra without any restrictive or coincidence condition) of the HPGe detectors, while the Multi Branch System (MBS) [95] from GSI records the data on an event by event basis to produce binary list mode data (LMD). Figure 3.7 shows a simplified schematic overview of the data acquisition layout.

3.3.1 GENIE system

The GENIE acquisition benefits from shorter dead-time compared to the MBS system and allows the measurement with a very low energy threshold. These are optimal conditions for recording singles spectra. Each of the preamplifier signals of the HPGe detectors were shaped by a Canberra spectroscopy amplifier and converted by a 14 bit Canberra MCA[1] singles spectra. Using the free XYLIB tool [96] the histograms can be converted from the proprietary format to standard ASCII files.

3.3.2 MBS system

The MBS acquisition system uses VME[2] electronics for digitisation of detector signals and data readout on an event by event basis. A single-slot PowerPC board of type CES RIO4 reads the data from the VME modules and produces a binary stream of list mode data. When combining readout electronics from several manufacturers – as was the case in these experiments – it is best to run the acquisition in a triggered mode, i.e. that all converters adhere to a central main trigger and synchronously converting the detector signals. The main feature of the MBS system is the flexible trigger logic TrLoII [97] implemented on the generic VME logic module VULOM4 from GSI. This trigger logic allows to define higher level triggers, such as coincidence triggers between detector groups, as a combination of low-level triggers generated using standard NIM electronics. Several features are also implemented to reduce the total event rate and thus decrease the system dead-time. A CAEN v775 TDC (time to digital converter) is used to record the detector times relative to the main trigger signal from the trigger logic, as well as the times of each generated low-level trigger. Detector count rates are recorded with a CAEN v830 scaler for the low and the high trigger threshold separately. The energy signals from the $LaBr_3$:Ce detectors are integrated using a CAEN v965 QDC (charge to digital converter). The signals

[1] Multi-channel analyser
[2] Versa Module Eurocard-bus

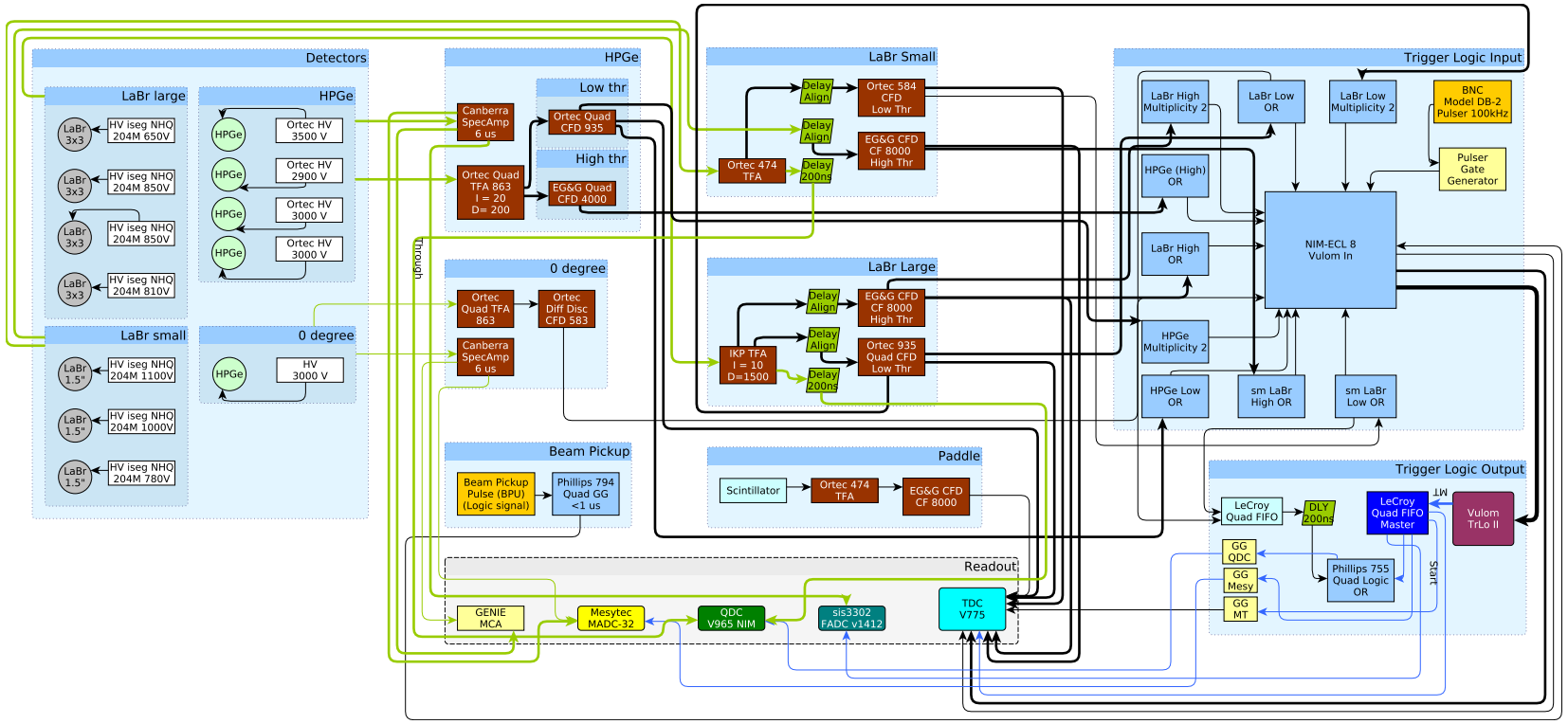

Figure 3.7: Schematic overview of the γ^3 data acquisition system, as it was used for the experiments in 2012. Some parts have been simplified for reasons of clarity. Green lines indicate analogue signals, black lines stand for timing and logic signals, and blue lines show the trigger distribution.

from the HPGe detectors were recorded with two different VME modules. The traditional readout was done using an Ortec spectroscopy amplifier in combination with a Mesytec MADC32 ADC (analogue to digital converter). In addition, a new digitising 16 bit flash ADC of type Struck SIS3302 operated at a sampling frequency of 100 MHz with the specialised Gamma-Firmware (V1412) was used. This firmware uses digital signal processing algorithms to determine the arrival time and energy of the pulses, and also adds information about pile-up and triggered channels.

The detector signals are split into two main paths; one for fast timing and triggering and one for energy measurement. In the case of the HPGe detectors, which readily provide two outputs from the preamplifier, this can be done directly. The signals from the $LaBr_3$:Ce detectors are first amplified by timing filter amplifiers (TFA) and then split.

The signals on the energy branch are delayed using passive delays by about 300 ns to account for the latency introduced by the CFD (constant fraction discriminator) delay, the trigger decision process and signal shaping or QDC gate generation. After the delay they are directly digitised using either ADCs in the case of the HPGe detectors or using a QDC for the $LaBr_3$:Ce detectors.

A crucial part of the electronics setup was to ensure a low jitter between the $LaBr_3$:Ce energy signals and the generated QDC gate to avoid energy resolution losses from incomplete charge integration. This necessitates the precise time alignment of the CFD output signals before entering the trigger logic module. The signals of each detector group were individually delayed to arrive within a time window of 3 ns and 20 ns for the $LaBr_3$:Ce and HPGe detectors respectively. The group of signals from the $LaBr_3$:Ce detectors was also delayed such that they always enter the trigger logic later than the HPGe signals to assure that they define the timing of combined triggers. The main trigger output of the trigger logic module has an inherent jitter of 10 ns, which is unacceptable for producing a QDC gate of good quality. For this reason a logic AND of the main trigger and the properly delayed OR trigger of the $LaBr_3$:Ce detectors is produced to create the QDC gate. The schematic is shown in Fig. 3.8.

Timing and trigger logic

The timing branch uses two CFD modules for each detector to provide two independent energy thresholds per channel. This allows to construct trigger conditions that require both a γ-ray with high energy and a second one with a lower energy in coincidence. This reduces the amount of coincidences where both photons have low energy and thus reduces the total event rate. Using standard NIM[3] electronics a number of low-level trigger conditions are composed from the CFD outputs, such as OR triggers for each of the detector groups (HPGe,

[3]Nuclear Instrumentation Module

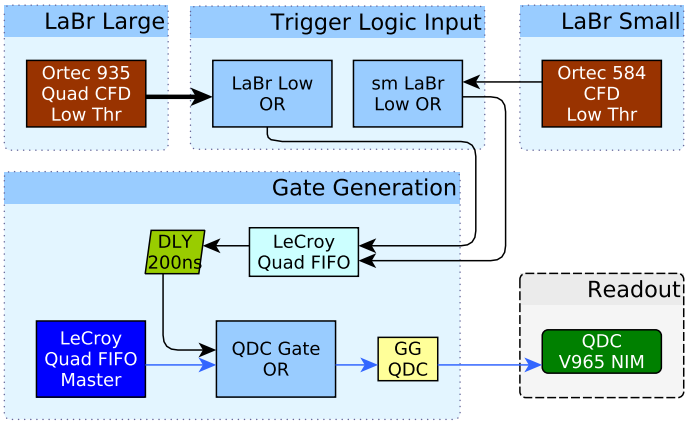

Figure 3.8: Schematic of QDC gate generation.

large $LaBr_3$:Ce, small $LaBr_3$:Ce) and multiplicity 2 (M2) triggers (i.e. two detectors of the same kind have triggered) for each group. These hardware triggers are combined in the trigger logic, which decides to either accept or decline a trigger and broadcast a main trigger signal (MT). The trigger logic TrLoII is implemented on an VME FPGA[4] board (VULOM 4) with 16 trigger inputs and an output for the main trigger. Any of the trigger inputs can be combined via a selection of coincidence or anti-coincidence conditions to form a high-level trigger. Such a trigger matrix is shown in Figure 3.9. Each column (red) in the matrix represents one of the low-level (RAW) triggers that enter the trigger logic, while each set of two rows (yellow) stands for one of the generated high-level triggers. Triggers can be combined either with a coincidence or anti-coincidence condition. These conditions are switched on by setting the matrix element to '1' in the corresponding row and column. Furthermore, the TrLoII also provides advanced features, such as a dead-time locking mechanism to avoid signal conversion before the readout is complete, scaler counters for individual triggers, trigger reduction factors, gate generators and periodic pulses. For each event the trigger pattern (TPAT), i.e. the information which of the triggers were active during the event, is generated and can be stored to disk along with the detector data. This allows to select specific subsets of data corresponding to certain trigger types in the analysis. All settings for the trigger can be adjusted via software commands or configuration files during the run time of the experiment. The combination of these features dramatically increases the flexibility of the setup, because it enables the user to quickly switch between different trigger schemes without the need to actually rewire the electronics, e.g. for calibration measurements, beam energy measurements or production runs. The γ^3 setup makes extensive use of this capability and consequently reduced the amount of necessary NIM electronics, resulting in a very compact 1-rack solution.

[4]Field-Programmable Gate Array

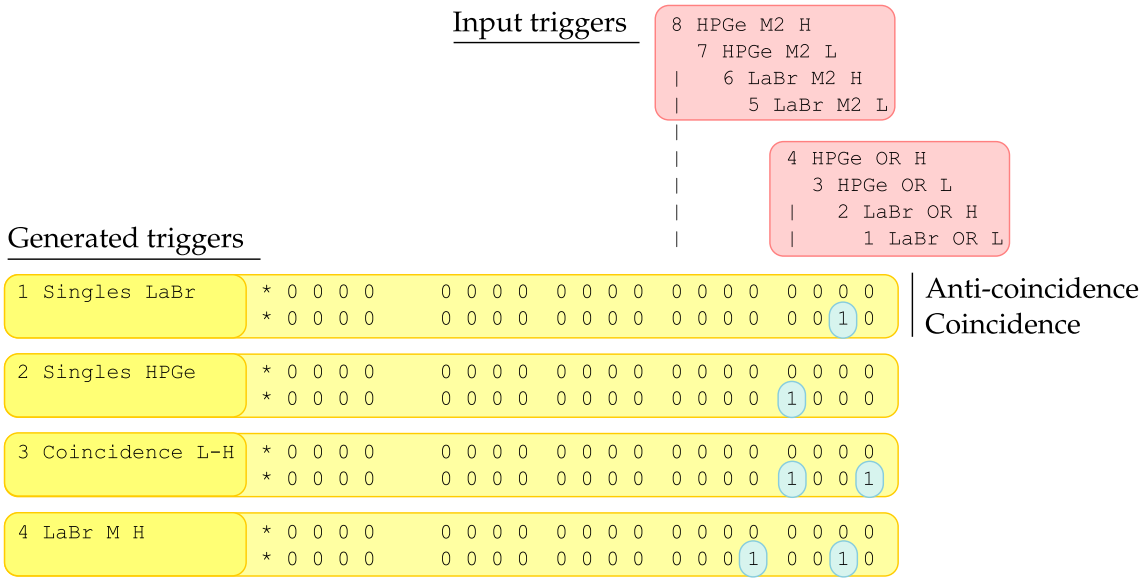

Figure 3.9: Exemplary part of the trigger matrix showing the configuration for the first four triggers. Each column (red) represents one of the low-level (RAW) triggers that enter the trigger logic, while each set of two rows (yellow) stands for one of the generated triggers. Triggers can be combined either with a coincidence or anti-coincidence condition. These conditions are switched on by setting the matrix element to '1' in the corresponding row and column.

3.3.3 Software

Unpacking

The recorded LMD files contain the collected data in a very compact and unaltered form, which is in many cases unsuitable for direct processing. The task of an unpacking (or sorting) program is to produce easily accessible data files in a standard format that allows the use of analysis frameworks to work on these data. Such an unpacking program usually has to be written to specifically match the data format in the LMD files. To reduce the amount of work needed to produce a suitable unpacking program, the configurable UCESB unpacker [98] is used. With the use of this unpacker the LMD files are converted to files containing ROOT [82] *trees*, which represent the experimental data for each recorded *event* in a single *entry* in the tree. Each detector channel (ADC, TDC, or QDC) is represented by a *branch* in the tree with a descriptive name assigned by the unpacker. Even though the UCESB unpacker provides also advanced features like calibration and filtering of the input data, this has not been used for the γ^3 experiments. The LMD data have to be unpacked only once to the ROOT data format. Calibration and analysis can then be done based on these files.

Online analysis and histogramming (GHOST)

To allow for monitoring of the data quality during the recording phase of the experiment it is useful to have the ability to quickly unpack, analyse and visualise the currently accumulated data. As described above, unpacking is handled by the UCESB unpacker, which cannot only read from already stored LMD files, but just as well read directly from a network stream provided by the data acquisition system. To read, analyse and display these files, the *Gamma Histogramming and Online Spectra Tool* (GHOST) was written as a ROOT program. GHOST updates the content of the histograms automatically, leading to a near-realtime view of the data. Each detector of the γ^3 setup is represented with two energy (uncalibrated and calibrated) and two timing (raw and with respect to a reference detector) histograms. Additionally, it is possible to specify filtering conditions (e.g. timing constraints) for a special set of energy histograms. The main feature of the visualisation is the possibility to directly produce summed energy histograms of all detectors of each type and also two-dimensional matrices showing the energies of two coincident detector hits. Figure 3.10 shows two screen shots of the running application. In the top screen shot the energy spectra are shown for the $LaBr_3$:Ce detectors, and the bottom picture shows the view containing the summed energy spectra and the coincidence matrices. For additional information on GHOST refer to Appendix 3.3.3.

3.3.4 ADC integral linearity

Different ADCs are known to exhibit differing behaviour regarding their integral linearity; a property which is very important for high resolution spectroscopy. To investigate this property, a few different ADC models have been used in the data acquisition system. The GENIE DAQ naturally uses the Canberra Multiport MCA with a very low value of 0.025 % (or 0.25 keV at 1 MeV) of non-linearity. This value is low enough that the effect is negligible given an energy resolution of HPGe detectors in the range of 2 keV to 8 keV between 1 MeV to 10 MeV (see Fig. 4.4). This has been confirmed by comparing energy spectra recorded with different channels at different gain settings. The integral linearity of the ADCs used in the MBS DAQ (namely the Mesytec MADC32 and the Struck SIS3302) tends not only to be worse compared to the Canberra MCA, but also a significant difference between these two modules can be seen. Figure 3.11 compares the deviation from a linear model for the two different modules as a function of the energy. Clearly, the deviation from linearity is much larger in the MADC32. For the analysis of the coincidence data only the energies as measured with the SIS3302 ADC have been used.

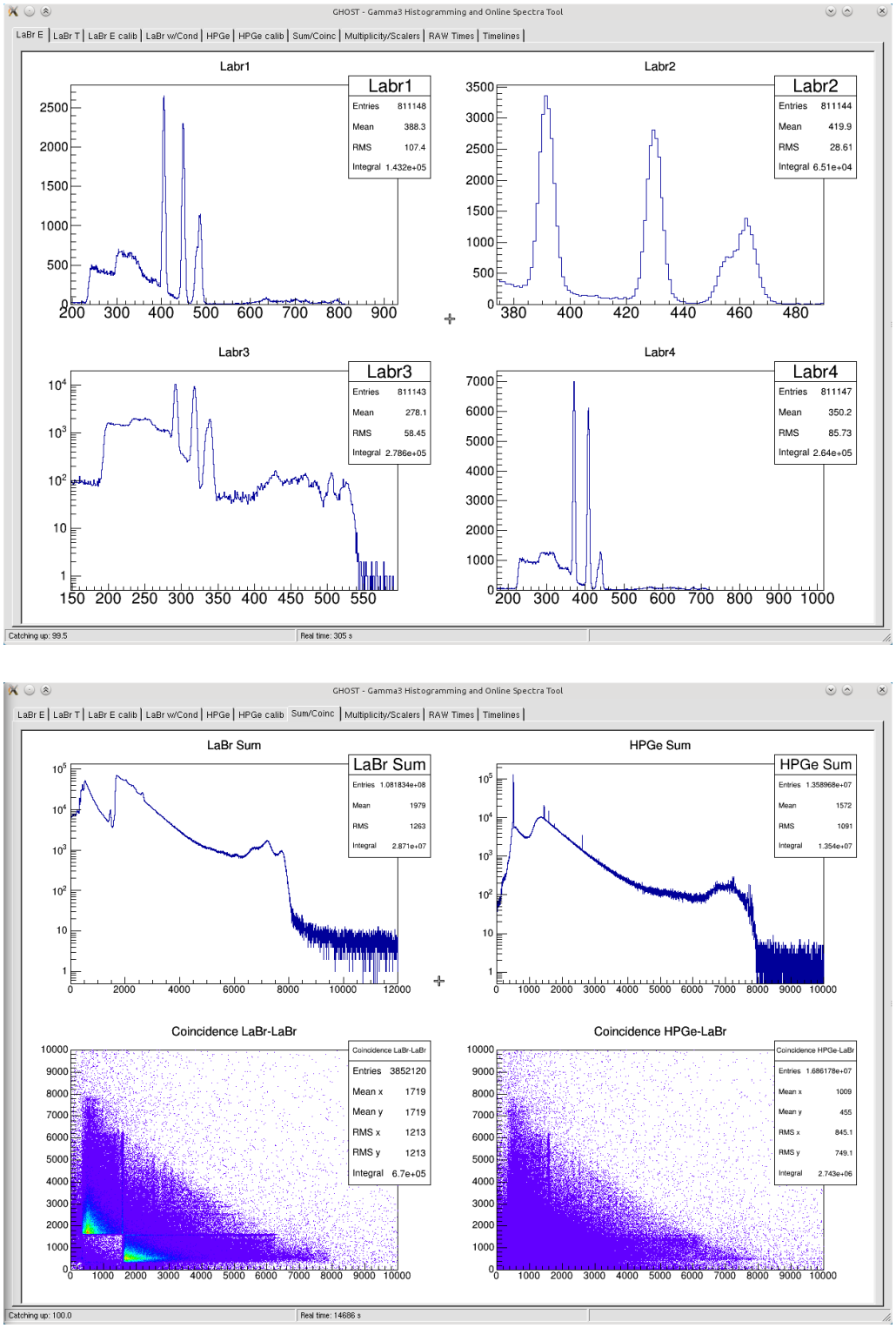

Figure 3.10: Screen captures showing the GHOST Histogramming Tool.

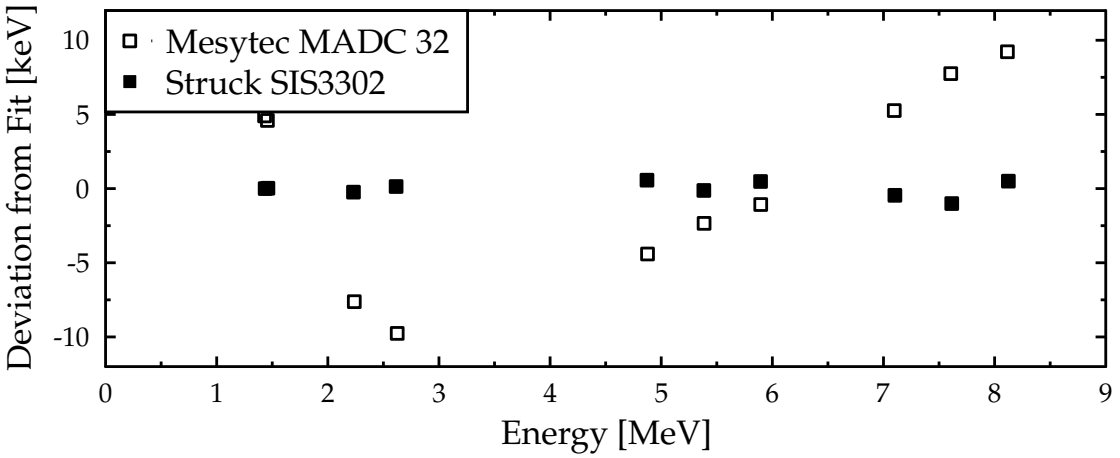

Figure 3.11: Comparison of integral linearity of the Mesytec MADC32 and Struck SIS3302 ADCs. Shown is the deviation from a linear fit of the peak positions to the energies of a spectrum from a ^{56}Co source.

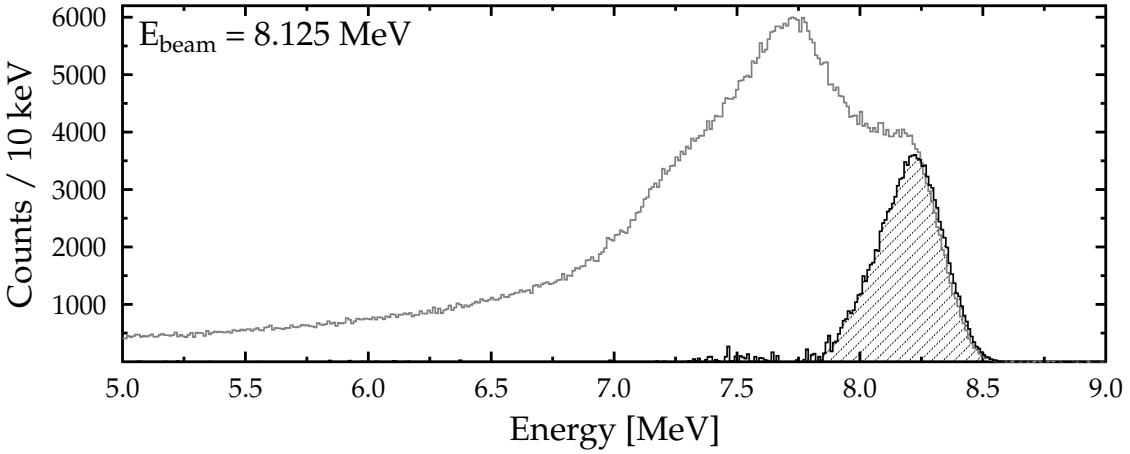

Figure 3.12: Spectral distribution of the photon beam, measured with the zero-degree detector (ZDD) for a mean energy of 8.125 MeV. The measured spectrum is shown in grey, and the spectrum after deconvolution in black. The resulting distribution is of Gaussian shape.

3.4 Diagnostics

Auxiliary measurements have to be done to provide data needed in the various analysis steps. This includes the knowledge of the photon flux and energy distribution of the beam, as well as measurement of the acquisition deadtime. A beam pulse pickup allows for better event selection, while precise position measurements have to be done to align the target. These particular points are the scope of this section.

3.4.1 Measurement of photon flux and energy

The energy distribution of the photon beam is measured at low beam intensity in between the NRF measurements with a 123 % HPGe detector (Zero-degree detector, ZDD) placed in the beam behind the target (see Fig. 3.2). The measured energy spectrum is a convolution of the true energy profile of the beam and the detector response of the HPGe detector as explained in detail in Section **??** (see also [87]). Using a set of simulated detector responses, the measured profile can be unfolded using the FORTRAN code DET_RESP_CORR to yield the underlying energy distribution of the beam, which is of Gaussian shape. This program is also an implementation of the Top-Down unfolding method, but includes the specific detector response for the ZDD. Figure 3.12 shows both the measured distribution as well as the unfolded distribution for the beam energy of 8.125 MeV. In the measured spectrum the detector response including the single escape and double escape peaks is visible, however washed out due to the beam energy spread of 4 %. The unfolded spectrum shows the beam energy distribution which is used to determine the photon flux. The energy distribution of the photons impinging on the target is an important factor in the NRF equation 2.8, if absolute transition strengths are of interest. At the HIγS facility the peak value of the photon flux and the energy spread of the distribution depend strongly on the various machine parameters, such as electron beam energy, laser photon energy and the fill level of the storage ring. Therefore, it is necessary to determine the energy distribution of the photon beam for each beam energy setting separately.

3.4.2 Deadtime measurement

System dead-time in the GENIE acquisition was mainly caused by the conversion time of roughly 6 µs of the MCAs, while the MBS DAQ was limited by a combination of ADC conversion time and the time needed for the readout of the VME modules, which amounted to a total of about 50 µs per event. The Canberra MCAs are counting dead-time internally on a per-channel basis, such that each of the detectors can be treated individually. For the MBS DAQ dead-time measurement is done in the TrLoII trigger logic along with the dead-time locking mechanism. Whenever a trigger is accepted, the dead-time signal is raised and stays active for the conversion and readout process. Only when the DAQ is finished the signal is reset and the next trigger can be accepted. The TrLoII counts all incoming (RAW) triggers, all generated high-level triggers before taking dead-time into account (BDT), and all accepted triggers (ADT, after dead-time), in addition also internal time-stamps with a precision of 10 ns are generated. From these values the MBS system dead-time for each high-level trigger can be calculated. To determine dead-time also in low count-rate situations and independent of detector electronics, an additional pulser signal with a

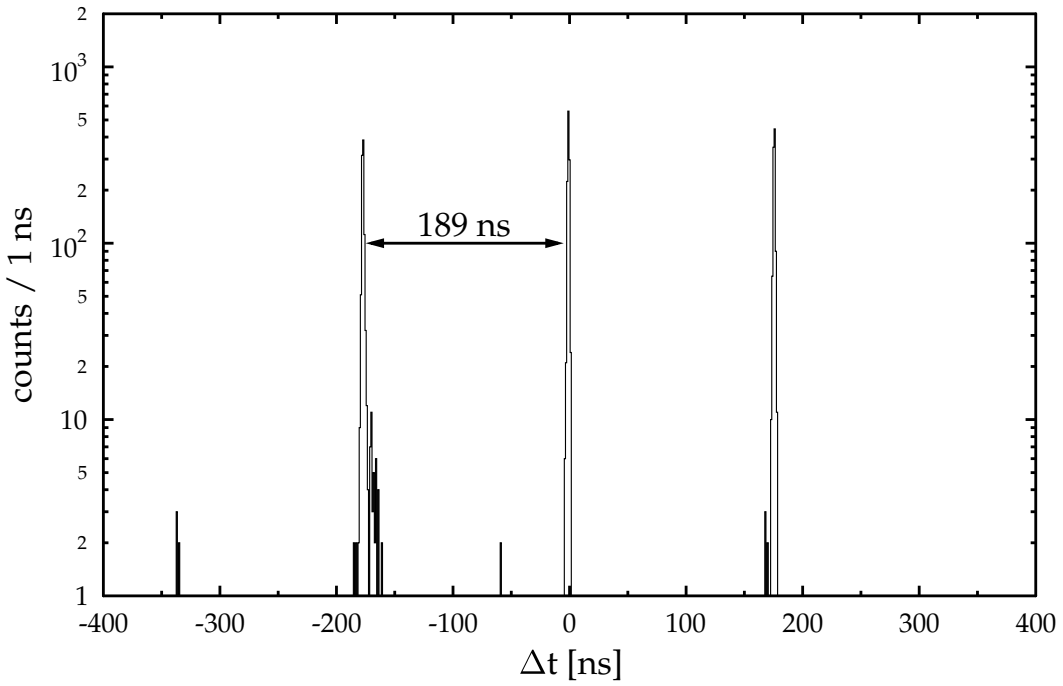

Figure 3.13: Time difference between LaBr detector 1 and beam pickup signal from the electron storage ring. The time interval between the peaks is 189 ns.

frequency of 100 kHz is used as a special *clock* trigger. A real-time measurement of the system dead-time is always available during the experiment through the DAQ software, such that either the beam intensity or the detector thresholds can be adjusted accordingly.

3.4.3 Beam pulse pickup

An inductive pulse pickup detector in the electron storage ring produces a time signal in a strict time relation to a burst of γ-rays from the FEL. The time interval between two beam bunches is about 187 ns. The timing signal from this detector is recorded by the TDC as well, which allows to measure the time difference between the reaction trigger and the photon beam, in order to suppress uncorrelated background events. Furthermore it prevents event mixing from adjacent beam bursts. Figure 3.13 shows this time difference histogram for LaBr detector 1 and the beam pulse pickup trigger. A large coincidence peak can be seen in the middle, surrounded by one smaller peak on the right, and two on the left. These smaller peaks correspond to coincidences stemming from two separate beam bunches. A complete discussion of the components in the time spectrum can be found in Section 4.1.4.

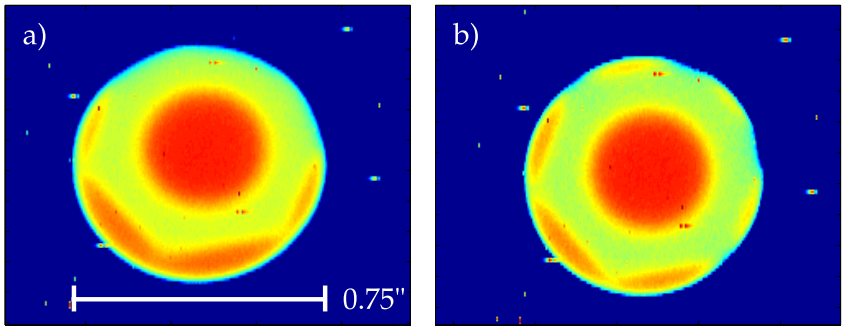

Figure 3.14: CCD image of the beam before (a) and after (b) alignment. For this particular imaging measurement a collimator with 0.75 inch diameter was used. The bright circle is the area illuminated by the beam. To achieve good contrast in the resulting image the target was replaced by a thick iron target.

3.4.4 Target alignment

For coarse alignment of the beam pipe and the target inside, a laser alignment system is used. To ensure that the beam also illuminates the full target area, an additional measurement using an X-ray CCD[5] camera with high spatial resolution is done [99]. Usually the target thickness of thin NRF targets is not high enough to produce sufficient contrast in the CCD image. Therefore this alignment step was done using a thick iron target. Figure 3.14 shows the CCD image before (left) and after (right) alignment. The bright circular area is illuminated by the beam. From these images it also is apparent, that the beam intensity falls off very rapidly at the edge, and that it is homogeneous within the illuminated area.

3.5 Experimental run

In 2012 and 2013 the γ^3 setup was used in two experimental campaigns with more than 1400 h of beam time. Twelve different isotopes in the low, medium and heavy mass region were investigated. The main objectives were the measurement of low-lying E1 strength and the decay of the PDR, the study of the fragmentation of the M1 scissors mode, as well as the measurement of the $[2^+ \otimes 3^-]$ 2-phonon state. A detailed list of the studied isotopes is shown in Table. 3.2.

During the commissioning phase for the γ^3 experiment in September 2012 the main properties of the complete experimental setup were determined to make final decisions for the following experiments. Measurements with radioactive sources for energy and efficiency calibration, as well as with the HIγS beam at

[5]Charge-Coupled Device

Table 3.2: Isotopes studied at γ^3 in 2012 and 2013.

Year	Isotope	Energy range [MeV]	Purpose
2012	^{40}Ca	5.9	2-phonon state
	^{76}Ge	2.2 – 4.1	Parities, E1 strength, collective modes
	^{124}Sn	5.2 – 8.6	Decay of PDR, parities
	^{140}Ce	3.64, 5.2 – 8.0	2-phonon state, Decay of PDR, parities
	^{154}Gd	3.07	Decay of Scissors Mode
	^{32}S	8.125	Commissioning Benchmark
2013	^{92,94}Zr	2.85 – 8.13	Parities
	^{128}Te	2.77 – 8.92	Decay of PDR
	^{140}Ce	7.7, 8.3	Decay of PDR
	^{152,156}Gd	2.88 – 3.18	Decay of Scissors Mode
	^{162,164}Dy	2.9 – 3.18	Decay of Scissors Mode to γ-band, E1 strength
	^{206}Pb	5.0 – 7.8	Decay of PDR

an energy of 8.125 MeV were done. The measurements with the beam helped to study the low-energy background from scattering on the target holder and the surrounding material. As a first feasibility test in 2011 had already shown, additional detector shielding was necessary to reduce the background contribution. In the commissioning phase the measured spectra show little to no background in the energy region of the beam (see Fig. 3.6), once the beam pipe was evacuated.

The measurement of the nucleus ^{32}S with the HIγS beam served as the main test case for the γ^3 setup and data acquisition. This isotope was chosen for two reasons: The level scheme of this nucleus is well investigated and includes a $J^\pi = 1^+$ state at 8.125 MeV, which is strongly excited in the (γ, γ') reaction. In addition, this state decays into the 2_1^+ state with a considerably large branching probability. A simplified level scheme with the relevant information of the 1^+ state is shown in Fig. 5.1.

3.6 Differences between the 2012 and 2013 beam time

Quite a number of modifications were made in the experimental setup of 2013 compared to the first campaign in 2012. Some for practical reasons such as the availability of detectors, other changes were made based on experience from the first set of experiments. These differences are important for the scope of this

thesis, since the ^{140}Ce data taken in 2012 was complemented by two additional measurements with beam energies of 7.7 MeV and 8.3 MeV in 2013.

Detector positions In 2013 four 3" x 3" $LaBr_3$:Ce detectors were used in the setup. The positions for the $LaBr_3$:Ce and HPGe detectors were changed according to the layout shown in the right part of Fig. 3.4. The main reason for this change was to have both types of detectors available at polar angles of 90° and 135°. This increases the sensitivity for parity measurements in the HPGe detectors for the price of reducing the $LaBr_3$:Ce efficiency (the minimum distance for the two backward $LaBr_3$:Ce was increased). This effect can be seen later in Section 4.1.3.

Electronics In 2013 a major effort was put into simplifying the experiment electronics. The reduced number of detectors helped to also reduce the number of CFDs and NIM electronics to generate low-level triggers. HPGe signals were only recorded using the Struck SIS3302 ADC instead of also using a second ADC, because the Struck ADC had shown superior performance at the cost of increased dead-time (see Section 3.3.4). These reductions allowed to fit all necessary electronics into two NIM bins and one VME crate.

Trigger logic Changes to the trigger logic involved mainly the removal of the triggers for the small $LaBr_3$:Ce detectors, leaving more trigger inputs available for the rest of the detectors and allowing a cleaner layout. In total eight different low-level triggers were created: For each detector type and for each of the low and high CFD thresholds an OR trigger an M2 (multiplicity 2) trigger were generated. Table B.2 shows how the high-level triggers were constructed.

Chapter 4

Data Analysis

Within the scope of this thesis two isotopes were studied in the (γ, γ') reaction. The experiments have been performed at the experimental setup described in the previous chapter. During the commissioning phase of this new setup, the isotope ^{32}S was investigated in order to study the experimental parameters of the setup. The pygmy dipole resonance, and in particular the decay behaviour of the states that are part of this low-lying E1 strength have been investigated in the nucleus ^{140}Ce as part of the γ^3 experimental campaigns in 2012 and 2013. The target properties and experimental parameters for the two targets are summarised in Table 4.1.

The following chapter describes the analysis steps that were performed on the measured data to yield the results shown in chapter 5 and chapter 6. At first the experimental procedure is explained including data calibration, event selection, the estimation of background radiation as well as the determination of the photon flux. Then the extraction of physical observables from the singles spectra and coincidence matrices is shown in detail.

4.1 Experimental procedure

Before any physical observables can be obtained from the measured data, several preparatory calibration steps have to be performed, which are presented in this section. Together with the common energy and time calibration, which allow the mapping from ADC or TDC channel values to measured energies and times, also a peak width calibration was done to aid in the peak fitting procedure. The non-linear behaviour of the $LaBr_3$:Ce detector electronics made a special treatment necessary that involved the unfolding of energy spectra to remove the detector response. This technique is used in several of the analysis steps, therefore it is explained first.

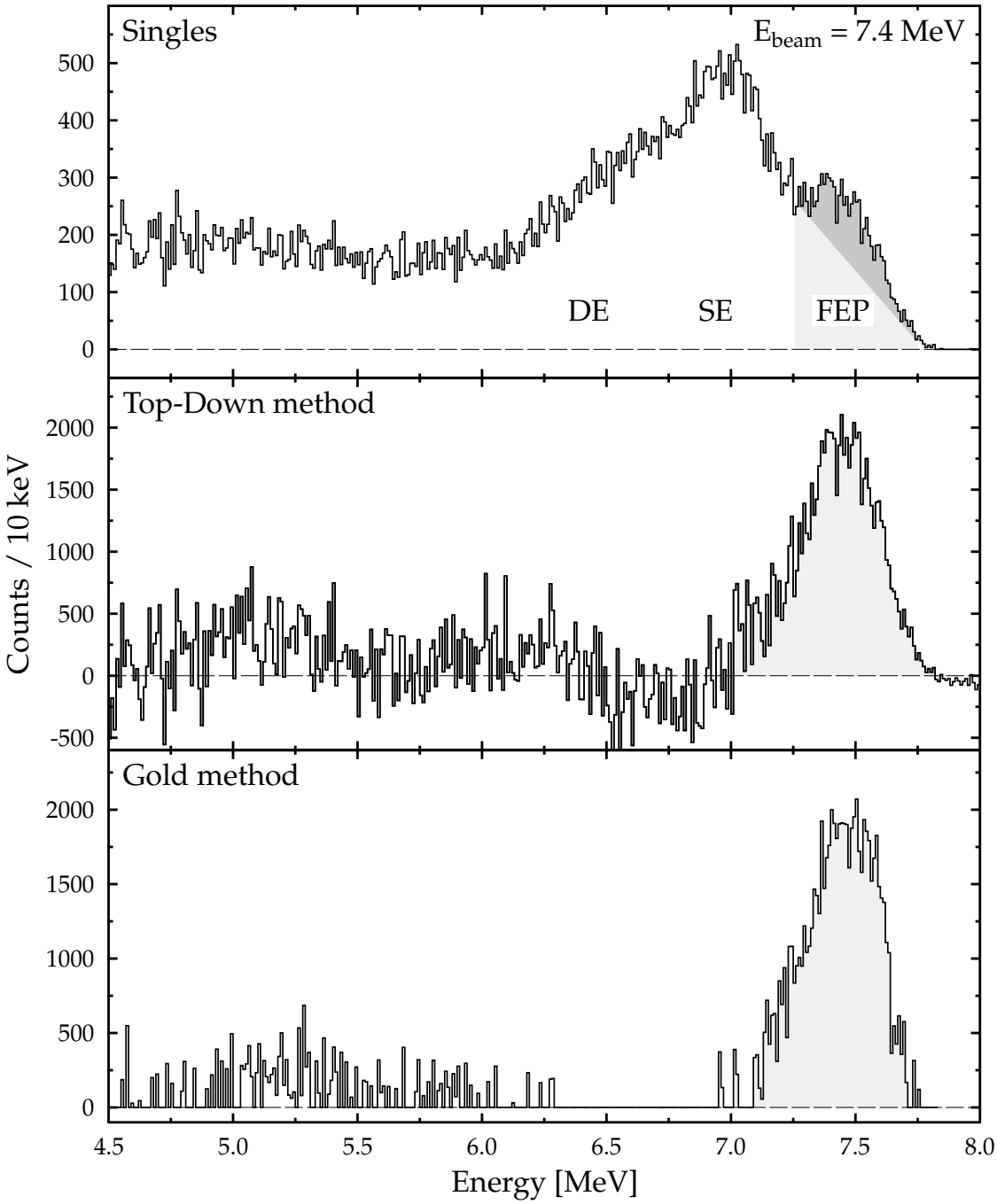

Figure 4.1: *Top:* Measured singles spectrum (summed $LaBr_3$:Ce detectors) with the ^{140}Ce target. Neither of the shaded areas are appropriate peak areas. Overlap with the SE region prevents a proper integration. *Middle:* Unfolded spectrum using Top-Down technique. *Bottom:* Spectrum unfolded using the Gold algorithm.

Table 4.1: Experimental properties for the measurements.

	^{32}S	^{140}Ce
Target thickness [mg/cm^2]	550(10)	320(9)
Isotopic enrichment [%]	95.02	99.72
Beam energy [MeV]	8.125	5.2, 5.4, 5.6, 5.9, 6.1, 6.3, 6.5, 6.8, 7.15, 7.4, 7.7, 8.0, 8.3
Electron ring current [mA]	80	45 – 80
Beam energy resolution [keV]	320	208 – 340
Average HPGe-trigger rate [kHz][a]	8 – 10	3 – 10
Average LaBr-trigger rate [kHz][b]	200 – 250	125 – 250
Average coincidence rate HPGe-LaBr [kHz][c]	0.03	0.03 – 0.5

[a] Single detector, from count rate meter
[b] Single detector, measured with scope
[c] Trigger: Coincidence High-Low, Before dead-time

4.1.1 Spectrum unfolding

As already introduced in chapter 2, it is possible to remove the effect of the detector response function from the measured detector energy spectra by the means of so-called *unfolding* algorithms. Two fundamentally different algorithms, the bin-wise Top-Down method and the Gold method, have been used to treat the data at hand.

In the current analysis the unfolding procedure has been done mainly for two related reasons: The measured $LaBr_3$:Ce spectra show – especially at higher beam energy settings – a large overlap of the full-energy peak range with the region of the single-escape peaks located 511 keV lower in energy. This impedes the direct integration of the full-energy peak area, because neither the integration limits can be chosen adequately, nor is the contribution from the overlap in the integration interval known. However, after properly applying the unfolding method the energy spectrum should only contain the full-energy peaks and the integration can be performed. The second case is to validate the correct energy calibration of the spectra. This is particularly necessary in the case of the $LaBr_3$:Ce detector, because of the strong non-linear component. In both cases the unfolding algorithm needs to know the detector response function of the detectors for the whole range of energies. These responses have been estimated using Monte-Carlo simulations (GEANT4) which are further explained in Section 4.1.3.

To illustrate the first problem, the upper part of Figure 4.1 shows the high energy part of a $LaBr_3$:Ce spectrum, where the full-energy peaks (FEP) clearly overlap with the regions of the single-escape (SEP) and double-escape (DEP)

peaks. From this spectrum alone it is difficult or unreasonable to integrate the FEP in either of the ways suggested by the shaded regions. The middle and the lower part of the figure show the same spectrum after applying either one of the unfolding algorithms. In both cases the contribution from the detector response is removed and only the FEP range remains. Integration of the peak area is now trivial, since integration limits can be chosen similar to the case of isolated peaks. The chosen interval is indicated by the shaded area in the figure. Both unfolding algorithms yield comparable results with an integral value of $78\,230(1300)$ counts for the Top-Down method and $73\,776(1000)$ for the Gold method. The scale on the y-axis changes, because unfolding restores all events from the detector response into the full-energy peak, and the number of events in the full-energy peak is increased.

The second problem is displayed in Fig. 4.2. The purpose of this figure is to highlight one important prerequisite that must be fulfilled before being able to apply the unfolding algorithm: The energy spectrum must be properly calibrated. However, without being able to unfold the spectrum it is difficult to measure the FEP energy for calibration, because of the strong overlap with other parts of the spectrum. This introduces a circular dependence between the validity of the applied energy calibration and the ability to properly unfold the spectrum. Such a dependency can be solved using either an iterative approach that converges towards the *best* energy calibration or by scanning the parameter space. Both methods require a convincing Figure of Merit (FOM) to judge the quality of the current iteration or parameter set. One FOM definition for each unfolding method will be discussed here. A simple method to define a FOM for the Top-Down unfolding method is apparent from the succession of unfolding results in Fig. 4.2. An incorrect calibration introduces artificial ripples in the spectrum below the FEP region (indicated with shaded areas in Fig. 4.2), because the SEP region in the measured spectrum does not line up with the simulated SEP region. Therefore whenever the calibration is not optimal, the wrong amount of counts is subtracted in the SEP region and subsequently added in the DEP region, or vice versa. This leads to increasing fluctuations towards lower energies. To define an FOM from this observation a measure for the *flatness* of the spectrum in the SEP and DEP region has to be defined. Under the assumption that the spectrum should be almost empty below the FEP, the easiest way to do this is to integrate the absolute values of the spectrum in the SEP region (as mentioned in Section 2.3.1 the Top-Down unfolding can also result in negative spectrum entries). This leads to the definition of the FOM as

$$\mathrm{FOM}_{\mathrm{TD}} = \sum_{i \in \mathrm{SEP}} |s_i| \,, \tag{4.1}$$

where s_i denotes the i-th bin in the spectrum. In Fig. 4.2 the SEP range is marked with vertical grey lines. The second FOM applicable to the Gold method involves

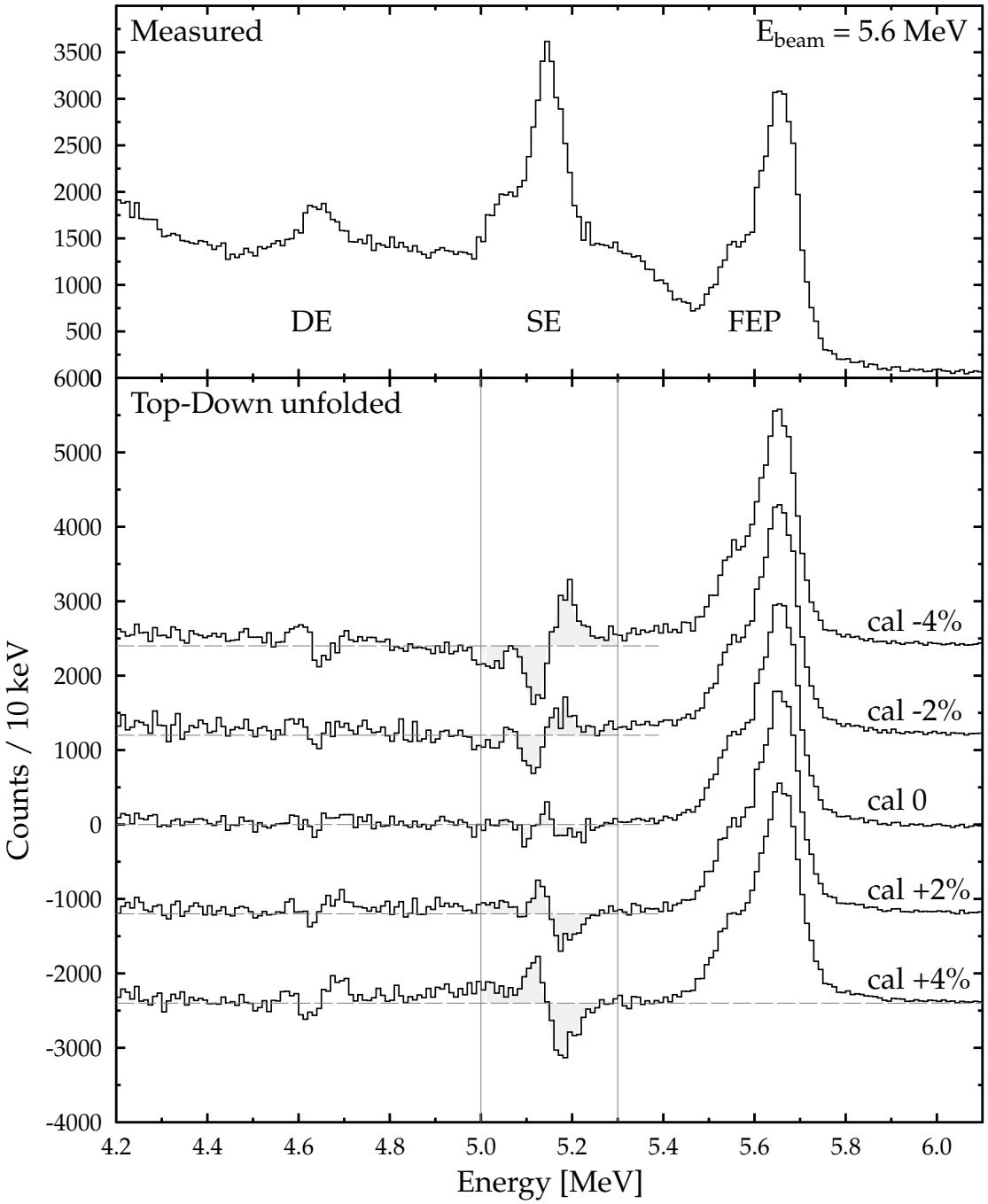

Figure 4.2: *Top:* Measured singles spectrum ($LaBr_3$:Ce detector) with beam energy 5.6 MeV and the ^{140}Ce target showing the typical detector response. *Bottom:* Unfolded spectra using the Top-Down method. Five different calibration settings were used before unfolding. The spectra are shifted along the y-axis for clarity. For each spectrum the respective zero is shown with dashed lines. The vertical grey lines mark the SEP range.

the comparison of the spectrum before unfolding to a re-folded spectrum of the unfolding result with a χ^2 test. This is possible, because the Gold method determines the unfolding result by minimising a global χ^2. Since the implementation of the algorithm does not provide this after convergence, it is computed afterwards:

$$\mathrm{FOM}_G = \chi^2(u, r)\,, \tag{4.2}$$

where the unfolded spectrum is called u and the spectrum after folding the detector response back in is denoted with r. The χ^2 value is computed according to

$$\chi^2(a, b) = \frac{1}{N}\sum_{i=0}^{N}\left(\frac{b_i - a_i}{\Delta a_i}\right)^2 \tag{4.3}$$

where a_i and b_i are i-th bins in the spectra and Δa_i is the uncertainty of a_i.

4.1.2 Energy calibration

To perform an energy calibration for the detectors, before and after each measured target, and in addition whenever the photon beam operation was suspended, measurements with calibration sources were done. For these measurements four different source materials (^{22}Na, ^{56}Co, ^{60}Co, and ^{137}Cs) were used to obtain a large number of calibration points both in energy and over the progression of the experiments. With these sources only energies up to 3.6 MeV can be reached. To obtain a good calibration also for higher energies it is possible to use well-known states excited in NRF experiments. Usually ^{11}B or ^{32}S are used for this purpose, because of strongly excited states at isolated energies (i.e. 4.444 MeV, 5.020 MeV, 7.285 MeV, 7.977 MeV and 8.125 MeV). Time-dependent effects can have an influence on the signal gain, and thus produce a change in the calibration. Since a calibration measurement at high energy is not feasible for every energy setting, the correction to the calibration has to be determined from the recorded data itself. Figure 4.3 shows the relative change of the slope parameter for the detectors over time as determined from the measured spectra. It is clear, that re-calibration for every beam energy is necessary, and that the continuous run time of 8 hours is the maximum in order to avoid severe degradation of energy resolution due to this effect.

At times also sudden jumps in the detector gain can arise during a single measurement. With the availability of list mode data it is possible to monitor the time-evolution of the detector calibration and to resolve this type of misbehaviour. The recorded data is split into several parts where each part has a constant calibration.

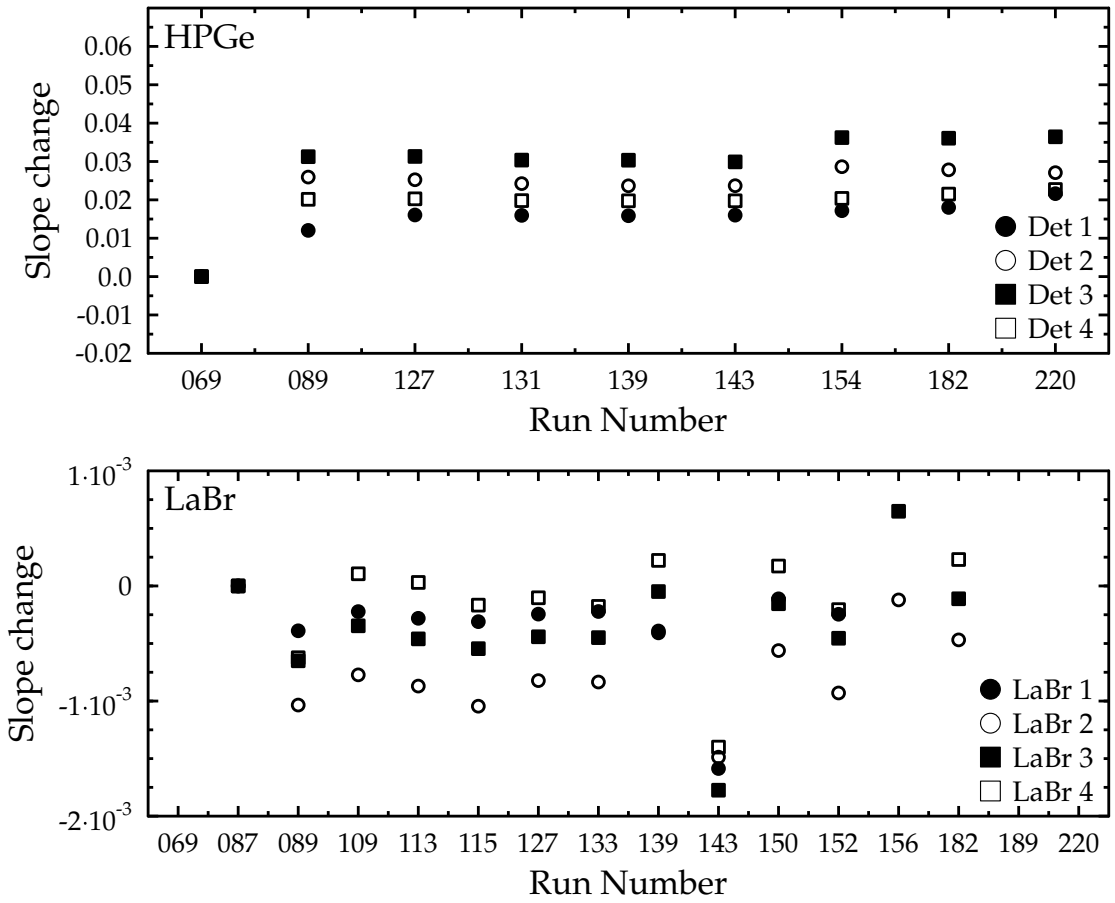

Figure 4.3: Slope parameter of the energy calibration as a function of the run number (i.e. time). *Top:* HPGe detectors. Normalised to run 069. *Bottom:* LaBr detectors. Normalised to run 087. The values for the first and the last two runs are well outside the plot range.

HPGe detectors

Mapping from ADC (or QDC) channels (x) to measured energy values (E) is usually done using a linear first order polynomial as a model function, such as:

$$E = ax + b\,, \tag{4.4}$$

with the slope parameter a and the offset b. This simple relationship can be used only in the case that the detector and all electronics are working in a linear fashion, where the output signal is proportional to the input. This is true for the HPGe detectors used in the γ^3 setup as was shown in Fig. 3.11.

Peak width calibration The peak fitting step of the analysis can be simplified, by providing a calibration of the peak widths (i.e. the energy resolution as

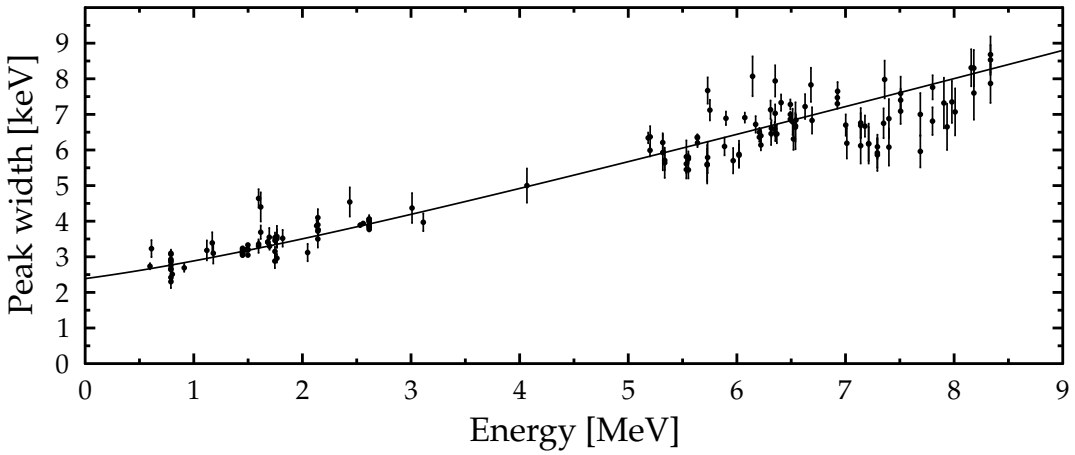

Figure 4.4: Measured peak widths as a function of the peak energy for the HPGe detectors. Shown together with a quadratic model fit (solid line).

a function of energy) for each detector. This allows to perform peak fitting with less parameters. Figure 4.4 displays the determined peaks widths for the complete energy range together with the fitted model curve. From Gilmore [78] the best model for this purpose is the square root quadratic model:

$$\omega = \sqrt{a^2 + b^2 x + c^2 x^2}\,, \tag{4.5}$$

with three fit parameters a, b, and c corresponding to different contributions to the total uncertainty of the peak position.

LaBr detectors

Normally the procedure of energy calibration for the $LaBr_3$:Ce detectors should be the same as for the HPGe detectors. During the experiment commissioning phase it was found that some components in the read-out introduce strong non-linear effects, such that a simple linear model can not be used for energy calibration. Instead, a third order polynomial is used:

$$E = ax^3 + bx^2 + cx + d\,, \tag{4.6}$$

with four fit parameters $a - d$. Naturally, compared to the linear model it is not advisable to fit such a function only at low energies and extrapolate the calibration to higher energies. Consequently, the calibration of the $LaBr_3$:Ce detectors requires the use of high energy calibration points such as from calibration standards like ^{32}S or ^{11}B or directly from the measured data. The upper part of Figure 4.5 shows an exemplary set of calibration data for an $LaBr_3$:Ce detector together with a linear model fitted to the lowest four data points and the cubic model fitted to all data points simultaneously. The strong deviation from the

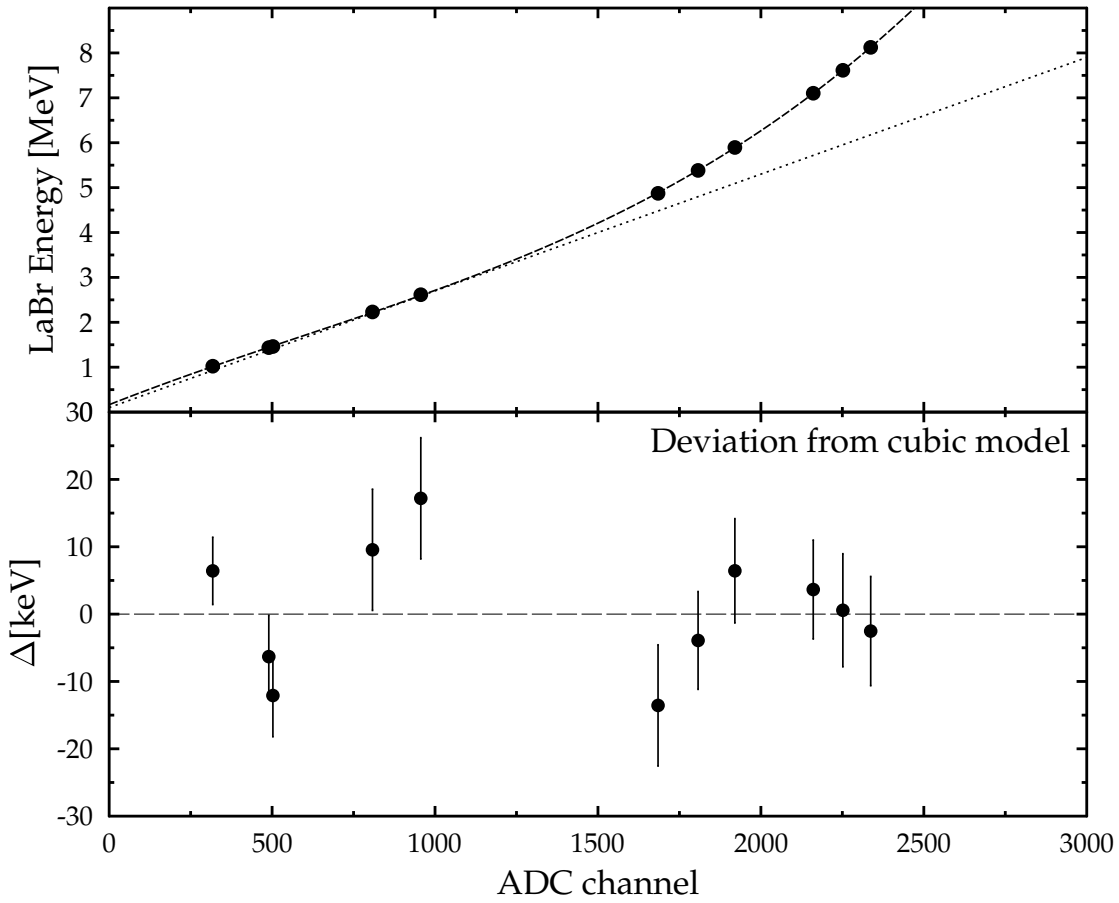

Figure 4.5: *Top:* $LaBr_3$:Ce energy calibration data shown together with a linear fit (dotted) to the lowest four data points and a cubic model fitted to all points (dashed). Error bars are smaller than the plot markers. *Bottom:* Deviation Δ of measured data from the cubic model.

linear model at higher energy is clearly visible. In the lower part of the figure the deviation from the cubic model is shown. It is apparent that the cubic model describes the data much better. Applying this mapping to the data will result in a seemingly correctly calibrated spectrum, but the local deviations from a perfect calibration lead to problems when trying to unfold the detector response. This problem was already described above and illustrated in Figure 4.2. An improper calibration shows up as nonphysical oscillations in the spectrum after the unfolding step. Using the different FOM values defined above it is possible to judge on the quality of a given calibration and select the one resulting in the best Figure of Merit. The exact peak area in the $LaBr_3$:Ce spectra is later only important in the context of determining the average branching ratio (see Section 4.3.3), such that only the energy region around the beam energy is of importance. Therefore only a local variation of the calibration is necessary to improve the unfolding

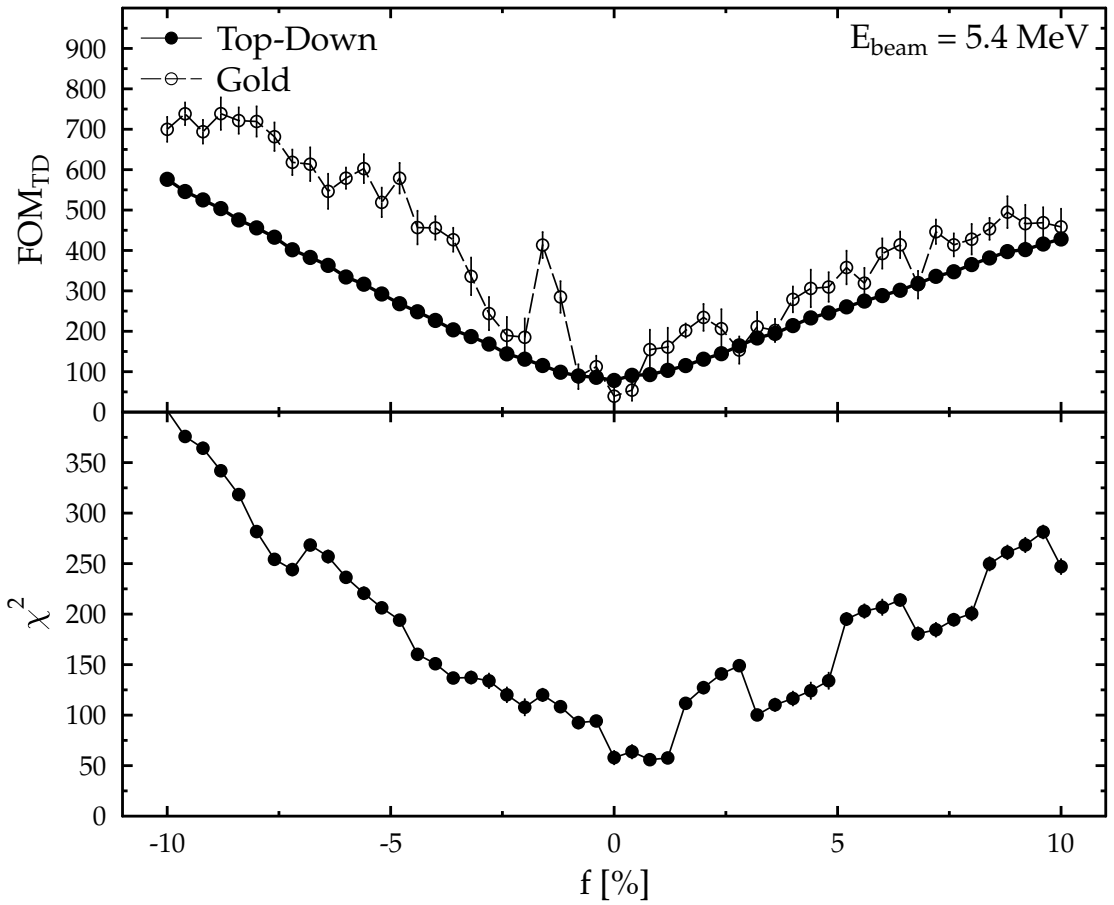

Figure 4.6: Different indicators for correct calibration. The errors are determined from varying the spectrum within its statistical errors and repeating the unfolding procedure. *Top:* Figure of Merit from the integration of the single-escape region of the spectrum. Applied to results from both the Top-Down and the Gold method. *Bottom:* χ^2 test comparing the Gold unfolded and re-folded spectrum with the original.

result. This is done by stretching or compressing the spectrum locally around the mean beam energy. The different FOM values are shown in Figure 4.6 over the stretching parameter f. In order to estimate uncertainties for this procedure, the initial spectrum is varied within its statistical uncertainties, stretched with the parameter f, unfolded, and then the FOM values are determined. This procedure is repeated 50 times. Apparently FOM_{TD} shows the clearest indication of a minimum, but the different FOM values agree closely with each other.

4.1.3 Efficiency calibration

The energy dependence of the detection efficiency for the different detectors has to be determined in order to derive absolute values for cross-sections in the

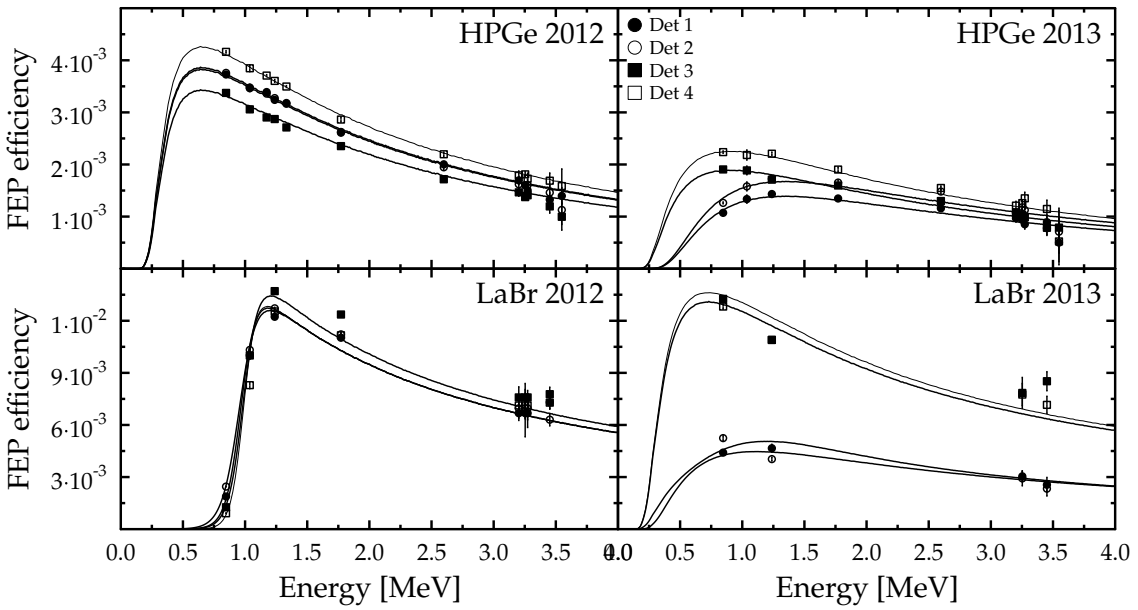

Figure 4.7: Full energy peak inefficiencies of both detector types during the ^{140}Ce beam times in 2012 and 2013. Show in solid lines are the results from the GEANT4 simulations.

analysis. Radioactive sources with a known activity can only be used up to an energy of 3.6 MeV. Therefore the efficiency is determined by using a combination of radioactive sources for the low-energy efficiency calibration and extrapolating to higher energies with the help of Monte-Carlo simulations (GEANT4). The absolute photo peak efficiency depends on the detector geometry (including any filters and shielding) and the intrinsic efficiency of the detector type, and can be expressed as:

$$\epsilon_{tot}(E) = \epsilon_{geo}(E) \cdot \epsilon_{intr}(E) \cdot \epsilon_{shield}(E)\,, \tag{4.7}$$

to stress that the different influences in the total efficiency can be factorised into independent parts. However, this separation is in fact not necessary in the current analysis, because for each detector geometry and for each set of shielding and filters a separate measurement with radioactive sources was done. The total efficiency for a specific peak in the source spectrum with energy E_i is thus determined with the following equation:

$$\epsilon_{tot}(E_i) = \frac{A_i}{\dot{N} \cdot I_i \cdot t_{meas}}\,, \tag{4.8}$$

with the measured peak area A_i, the source activity at the time of measurement $\dot{N}$, the relative emission probability for a photon of this energy I_i and the measurement time corrected for dead-time t_{meas}. For efficiency calibration of the data taken in the 2012 and 2013 experimental periods, source measurements with both a ^{56}Co and a ^{60}Co source were done. The efficiency was determined

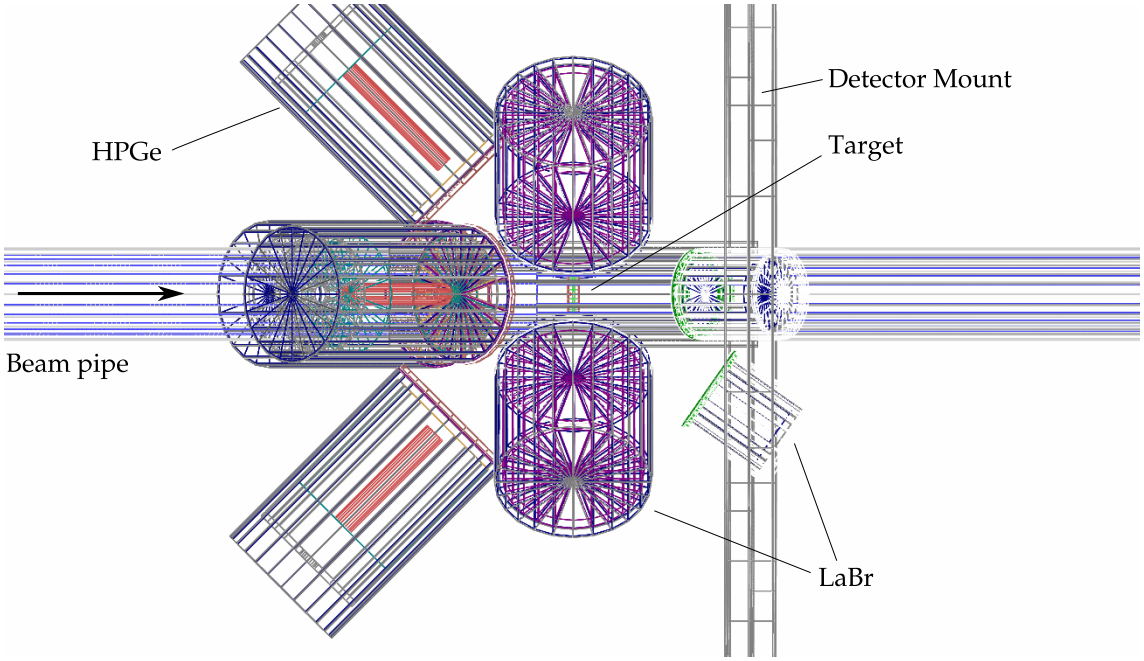

Figure 4.8: Wireframe model of the geometry used for the GEANT4 simulations.

for each detector separately and the results are shown in Figure 4.7 (on the left for 2012 and on the right for 2013). To allow for correct interpolation at energies in between the data points and for extrapolation to higher energies up to 10 MeV, Monte-Carlo simulations with the simulation framework GEANT4 [93] were done. Evidence for validity of this procedure was already given for this kind of experimental setup in [100]. The simulation results are shown as solid lines in the figure. In the 2012 measurements the 1.77 MeV data point in the $LaBr_3$:Ce data was systematically higher than predicted by the simulation, because of indistinguishable contributions from background radiation. The large difference between the deficiencies for the 2012 and the 2013 data is mainly due to the changes in the detector geometry (see Section 3.6).

Figure 4.8 shows a wireframe model of the geometry implemented for the simulation. Special care was taken to reproduce the geometry close to the target, i.e. the target holder and the beam pipe as well as lead shielding and the radiation filters in front of the detectors. To avoid possible alterations of the simulated efficiency shape no analytic function was fitted to the simulated curve. Instead the simulation was performed with a sufficient granularity of 1 keV for the generated photons. For each energy 1×10^8 photons were generated to be able to neglect the statistical uncertainty on the simulated spectra. Figure 2.3 shows a simulated HPGe spectrum for three different photon energies (511 keV, 2000 keV and 5000 keV). The change in the shape of the detector response function can be seen clearly. For each simulated spectrum the counts registered in the full energy

peak were counted and divided by the number of simulated photons to calculate the detector efficiency. The simulation results are shown in Fig 4.7 together with the measured data. To take into account the effect of a finite detector threshold the simulated efficiency curve was truncated at the threshold energy E_{thr} by weighting it with a washed-out step function with a variable diffuse parameter d:

$$\epsilon_{sim,thr}(E_i) = \frac{1}{1 - e^{\frac{E_{thr} - E_i}{d}}} \cdot \epsilon_{sim}(E_i)\,. \tag{4.9}$$

The two parameters E_{thr} and d were fitted using iteratively scanning the parameter space and minimising χ^2. Due to the good accuracy of the simulation the measured efficiency was reproduced very well. Deviations from the measured efficiency could be attributed to the measurement uncertainty for the distance of the detectors from the target.

4.1.4 Event selection

The list mode data acquired with the MBS system allows for selecting subsets of the recorded events by requiring restrictive conditions (often called 'cuts') for an event. The condition can extend to any of the recorded energies, times, and additional information. Two selections are particularly useful in the current analysis, namely the trigger selection as well as the detector timing selection.

Trigger selection Trigger selection involves constraining the recorded trigger pattern (TPAT) to all values that include the wanted trigger condition. If for example only those events with a coincidence between $LaBr_3$:Ce and HPGe detectors are of interest, then TPAT is constrained to all values where the second bit is set to logic '1'. This is done efficiently by testing whether or not this bit is set using a bit-wise AND operation:

$$(\mathrm{TPAT}\&4) == 4\,. \tag{4.10}$$

In the ROOT framework the resulting event numbers that satisfy this selection can be easily saved to disk as an `EntryList` using the `TTree::Draw` method. In subsequent analysis passes over the same data the list of entries can be reloaded and applied to the same `TTree` again using the `TTree::SetEntryList` method.

Detector Timing selection In addition to trigger selection it is also possible to put constraints on the relative timing between detector signals. This creates a proper coincidence condition yielding in a reduced amount of random background radiation or intrinsic radiation from the $LaBr_3$:Ce detectors. Also a selection of a proper timing relation to the beam pickup monitor allows to select events in coincidence to the incoming photon beam (i.e. with a cut on the

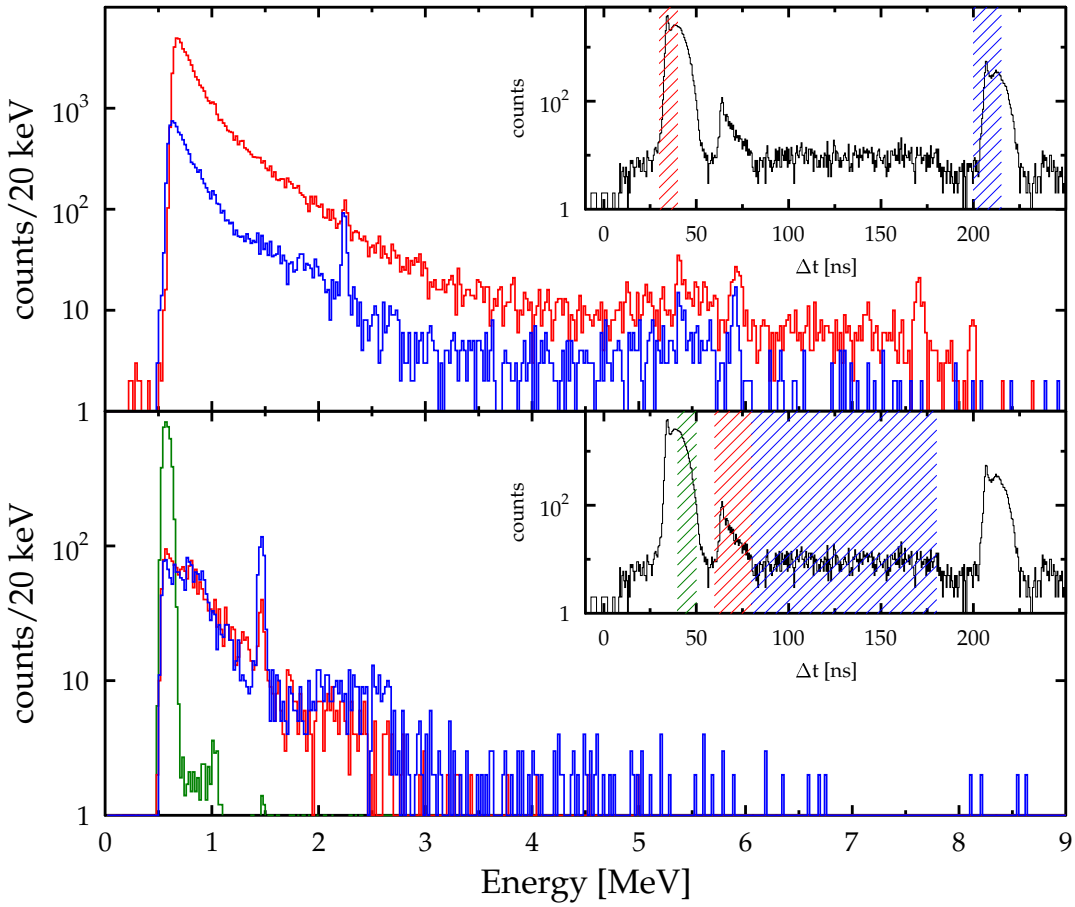

Figure 4.9: Energy spectra of LaBr3 resulting from different conditions on the beam pickup time spectrum for this detector ($t_{bpu} - t_{labr3}$). The respective ranges are marked in the inset. *Top:* Cuts on the prominent coincidence peaks yield the events stemming from reactions of the beam with the target. *Bottom:* Several sources of background can be identified with cuts on other parts of the time spectrum: (Green) Compton scattered photons from the reaction, (Red) Scattered photons from surrounding geometry, (Blue) Natural background.

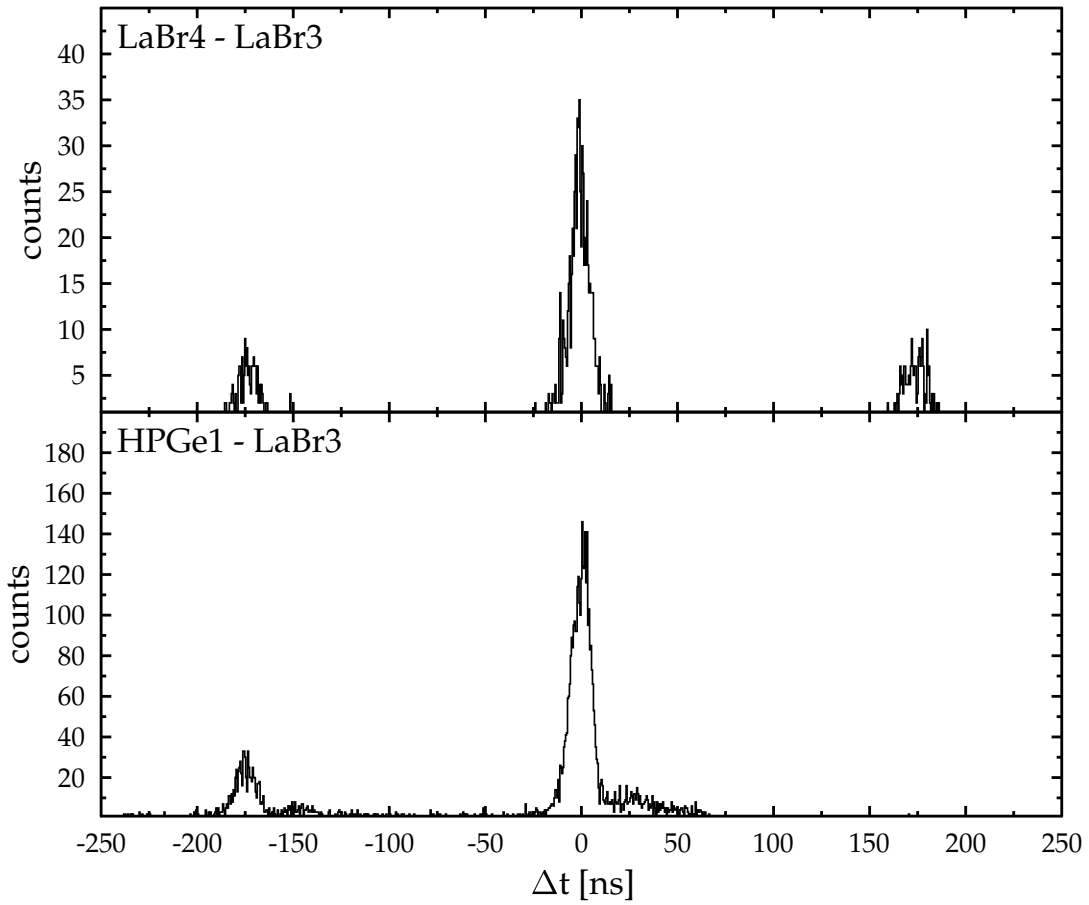

Figure 4.10: Time difference spectra for an HPGe and an $LaBr_3$:Ce detector with respect to the time measured in the LaBr3.

"prompt" peak in the spectrum). The inverse condition on the other hand produces a spectrum containing mainly background radiation and only a very small amount of beam related events. This effect is shown in the spectra in Figure 4.9. The top part shows the recorded ^{32}S data (2013, run 150) for one of the $LaBr_3$:Ce detectors (LaBr3), while the lower part shows the same data with complementary conditions. These allow to identify several different sources of background in the ungated spectra. Unfortunately, due to a failure in the electronics, the BPM signal was not available for the ^{140}Ce measurement and this kind of selection is not possible in the current analysis. The failure was discovered shortly after the ^{140}Ce measurement and the BPM signal is present in all data recorded afterwards.

A coincidence between two detectors is defined by using the time difference spectrum between the signals of the corresponding detectors (LaBr4 and HPGe3). Figure 4.10 shows a timing histogram for two detectors with respect to LaBr3. The detector times are plotted with respect to the time of the LaBr3 detec-

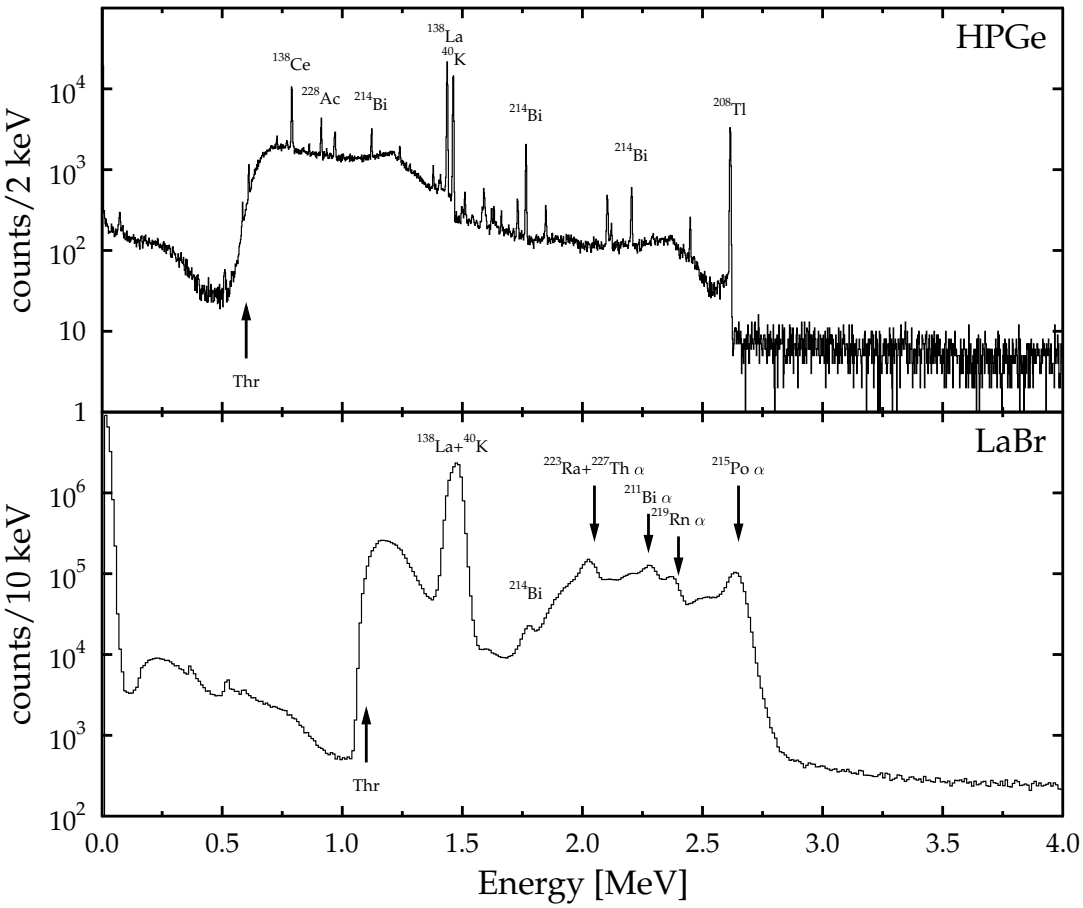

Figure 4.11: Natural background energy spectrum as measured with the $LaBr_3$:Ce and HPGe detectors over the course of 24 h.

tor. In both cases the prompt peak containing the coincidences is well separated from the peaks stemming from random coincidences of adjacent beam bunches. Applying a condition that only selects the main peak avoids bunch mixing and suppresses random coincidences.

4.1.5 Background estimation

Contributions in the recorded spectra which do not stem from the NRF reaction are typically regarded as 'background' radiation. The most prominent types of background encountered in the measurements are discussed here and are treated as part of the analysis.

Natural random background radiation First the background radiation originating from the immediate surrounding of the γ^3 setup is considered. Figure 4.11 shows an energy spectrum of the background radiation recorded over

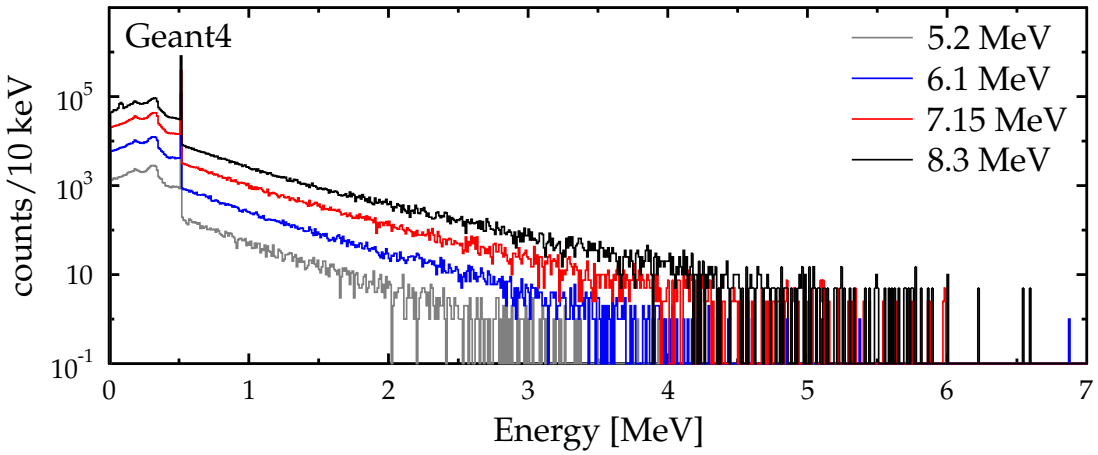

Figure 4.12: Simulation of the non-resonantly scattered radiation for four different beam energies. The shape of the beam profile has been taken into account.

the course of 24 h in logarithmic scale (Top: HPGe, bottom: $LaBr_3$:Ce). The most prominent peaks are labelled with the corresponding isotope. Due to the limited resolution and the large contribution of intrinsic radiation in the $LaBr_3$:Ce spectrum most of the peaks visible in the HPGe spectrum can not be distinguished. The approximate energy of the CFD thresholds are marked with an arrow in both cases. The intrinsic background radiation in $LaBr_3$:Ce is due to the decay of the isotope ^{138}La with a natural abundance of 0.09 % via electron capture and beta decay [101]. Additional contribution to the background at higher energies is due to the decay of ^{227}Ac impurities in the crystal [102]. At energies above 2.7 MeV the spectra contain only events due to interaction of cosmic radiation with the detectors. This background contribution is only important in singles spectra, because a coincidence condition very effectively suppresses natural background.

Non-resonant beam background The second important source of background radiation is the photon beam itself. Since only a small amount of the photons passing through the target participate in the NRF reaction, the fraction of photons which are scattered in the target by means of non-resonant processes (Thomson or Compton scattering) is quite substantial and constitutes a large percentage of the events in the recorded spectrum. Since this type of background is correlated to the photon beam and is stemming from the target, it cannot be distinguished from the photons emitted in the NRF reaction. However, with the help of GEANT4 it is possible to simulate exclusively this sort of background contribution. Examples are shown in Figure 4.12 for four different energies (5.2 MeV, 6.1 MeV, 7.15 MeV and 8.3 MeV). The simulations take into account the spectral distribution of incident photons and the detector geometry

of the γ^3-setup. From these examples it is apparent that the main contribution from non-resonant background is located at low energies and extends in an exponential manner up to slightly below the energy of the beam energy.

Fully synthetic spectrum When all considered sources of background are taken into account and all other sources are comparatively less relevant, it should be possible to fully reconstruct the measured spectrum. In this procedure for each of the known states the simulated detector response is added up in accordance with Equ. 2.8 including the transition strength, the number of target nuclei, the detector efficiency and the measurement time. This spectrum is folded with a Gaussian distribution of variable width corresponding to the detector resolution that was determined as described in Section 4.1.2. To this spectrum the different background contributions are added. The natural background is scaled according to the measurement time. The non-resonant background scales with the photon flux. Figure 4.13 shows the measured spectrum in the top part, the synthetic spectrum in the middle part together with all constituents, and the relative difference between the two in the bottom part. The difference is usually below 15 % for an energy above the threshold at 1 MeV, which means that all major features in the spectrum can be explained and have been taken into account for the reconstruction. This shows convincingly that other sources of background must be small. They have been reduced to a minimum by proper beam collimation, detector shielding, and the evacuation of the beam pipe as shown in Section 3.2.1.

4.1.6 Determination of the photon flux

The number of photons available for a reaction during the experiment is typically called the photon flux N_γ. Equation 2.8 requires the knowledge of the photon flux in order to determine absolute cross-sections. In NRF experiments with a photon beam produced via bremsstrahlung the photon flux can usually be measured directly using a calibration standard such as ^{11}B as a secondary target (see e.g. [29, 103]). At the HIγS facility this procedure is not possible, because in most cases the nuclear levels used for calibration are not excited with the same energy setting that is used for the measurement. Thus, other ways for obtaining the photon flux have to be pursued. These methods have already been mentioned before in Section 3.4.1. Here the analysis is described in detail, and the results that are used for the ^{140}Ce experiment are determined.

Several techniques to determine the photon flux can be employed. The simplest method is applicable, if the ground-state transition strengths of the prominent states in the measured energy region and the energy profile of the beam are already known to a good precision. In this case the beam profile can be fitted to the measured peak areas, weighted by the known strengths. The resulting scal-

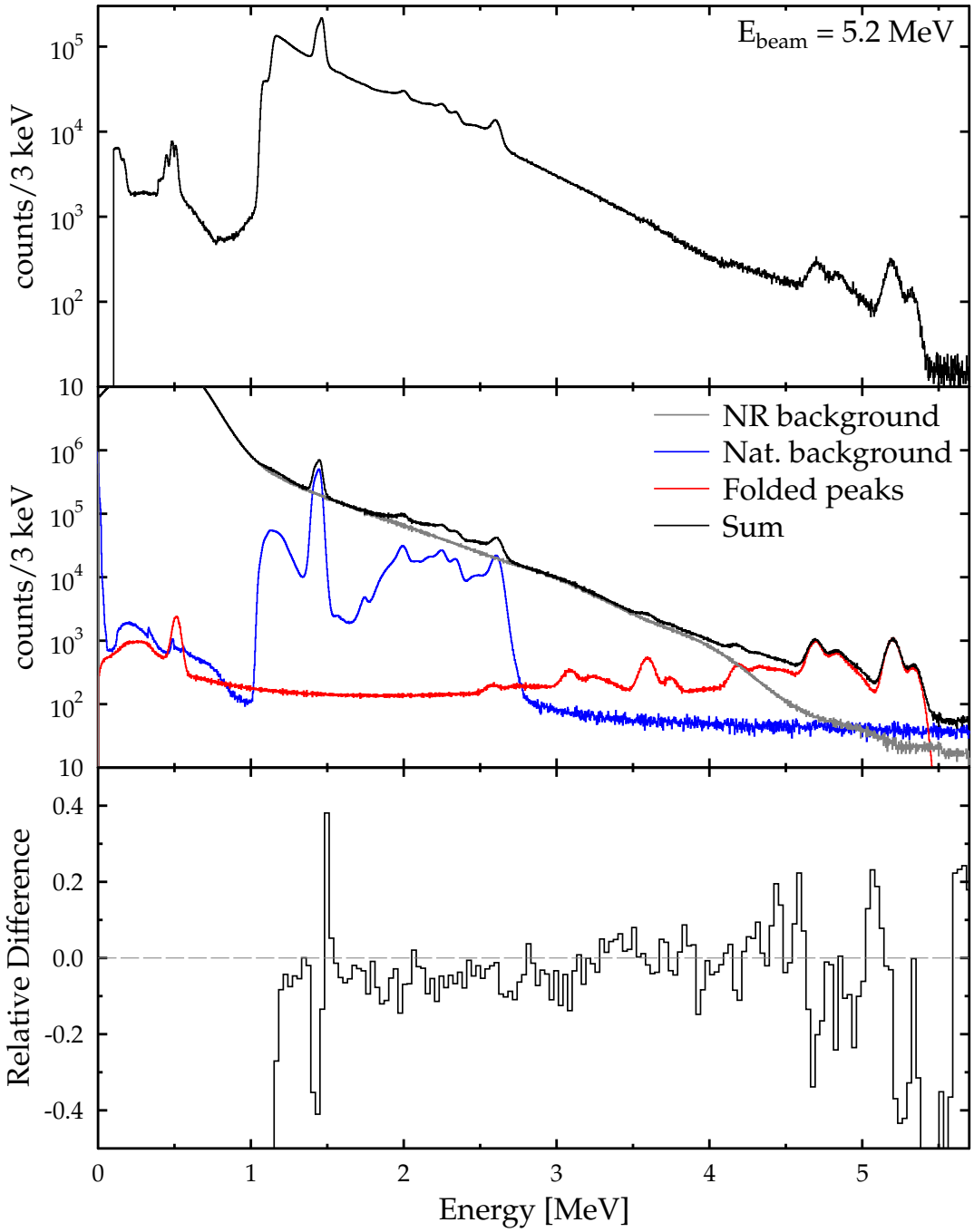

Figure 4.13: Spectrum reconstruction. *Top:* Measured $LaBr_3$:Ce energy spectrum at 5.2 MeV. *Middle:* Reconstructed spectrum (black) and its constituents (red, blue, and grey). See text for details. *Bottom:* Relative difference between measured and reconstructed spectrum.

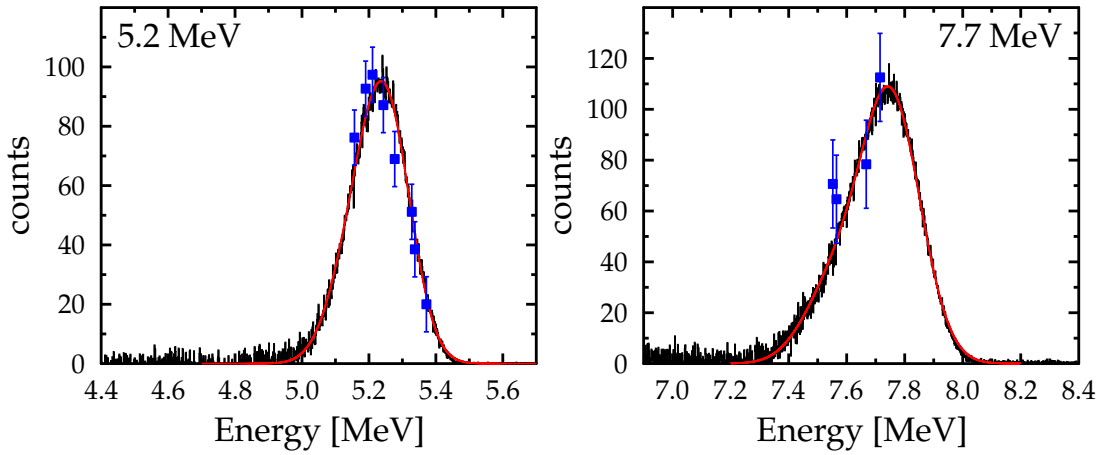

Figure 4.14: Unfolded beam shape (black) together with the fitted model function (red). The beam shape for the lowest and the highest energy are shown. Data points for the normalisation are displayed in blue.

ing factor represents the photon flux. The second method uses the information from the first method, but allows to extend the energy range to regions where no strengths are known beforehand. The beam intensity is measured behind the collimator using a thin (2 mm) plastic scintillator paddle. From the count rate on the paddle and the energy dependent energy loss it is possible to determine a relative scaling factor for two different beam energy settings. Care must be taken at higher intensities where the count rate on the paddle approaches 200 kHz, since then pile-up effects start to play a role and artificially decrease the measured count rate. The last method is based on the fact that only a negligible fraction of the photons in the beam participate in a reaction in the target material, while the rest continues until the end of the beam line. A 1 mm thick Cu plate is placed in the beam at a distance of 110 cm behind the target. The elastically scattered photons from this plate are then detected by an HPGe detector placed at a scattering angle of 7°. With the help of Monte Carlo simulations it is possible to derive the absolute photon flux of the incident beam from the number of scattered photons. This method can be used as a cross-check for the other two methods, however this analysis it was not used.

Normalisation to known transitions

As described in Section 3.4.1 the energy distribution of the incoming photon beam can be determined using the zero degree detector (ZDD). If the integrated cross-section for at least one transition in the measured spectrum is known, the normalisation can be performed. To obtain an absolute normalisation of the photon flux, the energy distribution is scaled to this cross-section. In the case of ^{140}Ce this is possible in the energy range from 3.6 MeV to 7.7 MeV, where tabu-

lated values from experiments with bremsstrahlung are available [63, 104]. The normalisation procedure is as follows: The spectral shape of the photon beam is measured using the ZDD and unfolded using the DET_RESP_CORR program to yield the pure beam spectrum (see Section 3.4.1). For further calculations a model function is fitted to the unfolded beam shape, in order to have a suitable analytic description for a fitting procedure. This function is expressed as the sum of two Gaussian distributions with similar width separated by a small energy difference. Figure 4.14 shows the unfolded beam shape (black) together with the fitted model (red) for the lowest (5.2 MeV) and the highest (7.7 MeV) energy setting where experimental data are available. It is clear that the chosen model represents the data very well independent of beam energy. The model beam shape is normalised, such that the area under the Gaussians is unity. This allows to separate the photon flux into a scaling factor $N_{\gamma,0}$ and an energy dependent shape:

$$N_\gamma = N_{\gamma,0} \cdot n_\gamma(E) \tag{4.11}$$

For each energy setting all tabulated values for known cross-sections I_i within the beam energy range are selected. The corresponding peak areas A_i in the measured spectra are used to determine the scaling factor for the specific beam energy setting via least-squares optimisation:

$$N_{\gamma,0} \cdot n_\gamma(E_i) = \frac{A_i}{I_i \cdot \epsilon(E_i) \cdot N_T} \tag{4.12}$$

Using this technique the photon flux at the beam energy settings from 5.2 MeV to 7.7 MeV is determined. The resulting values for the photon flux for all energies are summarised in Table 4.2.

Normalisation to the incoming photon beam

As mentioned in Sec. 4.1.6, a thin scintillator paddle is placed in the photon beam behind the collimator. The total count rate observed in this detector is therefore proportional to the integrated photon flux. However, in order to provide an absolute calibration, the proportionality factor has to be determined. This is done using the values for the absolute photon flux at lower energies, determined via known cross-sections as explained above and extrapolate this calibration to higher energies. Figure 4.15 shows the measured paddle counts as a function of the beam energy and also the ratio of the counts over the flux $N_{\gamma,0}$ as determined from known transitions. Data from [63] as well as from [104] have been used. Fitting a linear function to the two data sets allows to extrapolate to higher energies. From the figure it is clear, that a systematic difference between the two data sets exists. Using the extrapolation it is possible to determine the photon flux in the complete energy range. The result is shown in the lower part of Fig. 4.15. Filled squares mark the values determined from [63], and open squares

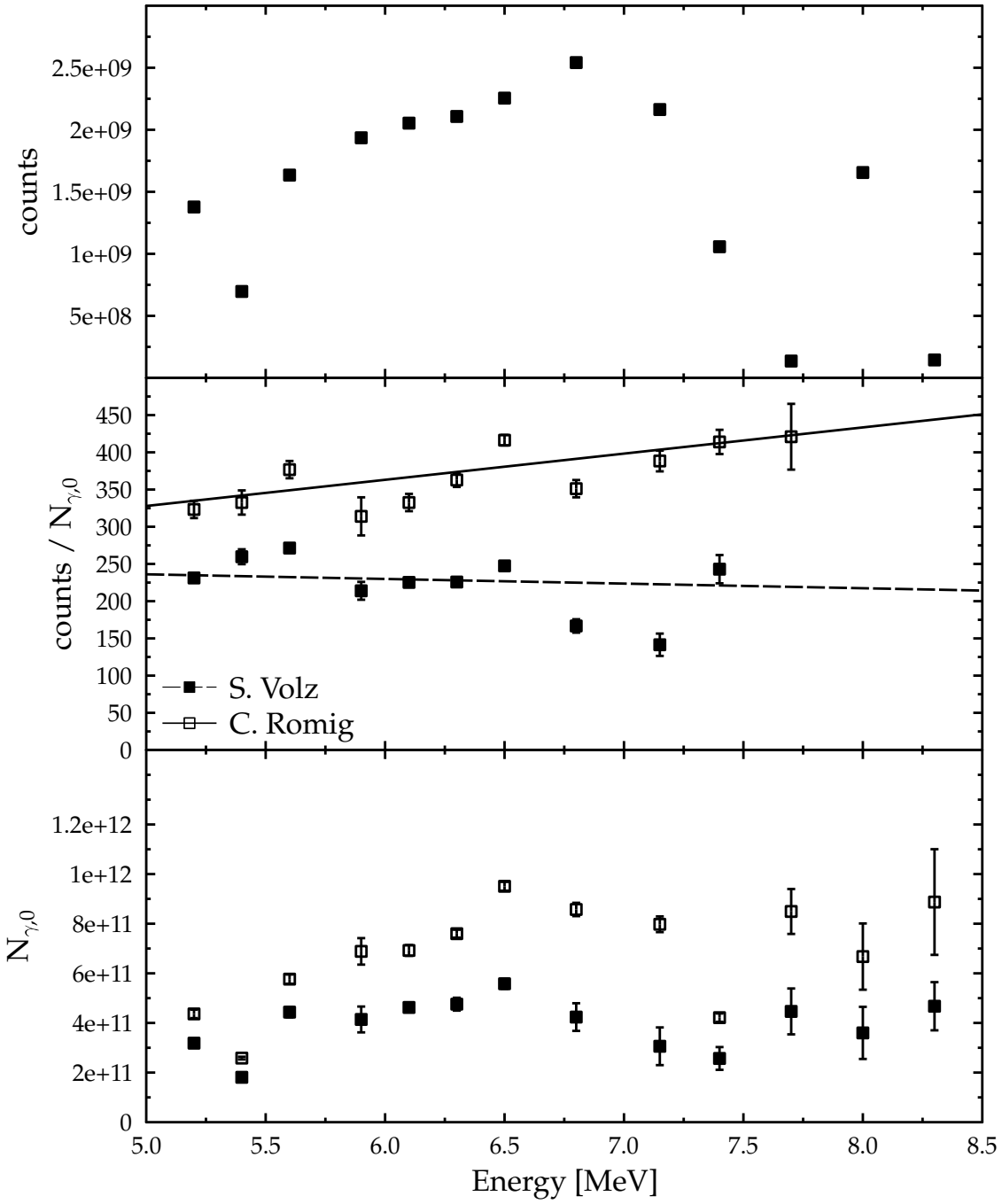

Figure 4.15: *Top:* Measured counts from the paddle scintillator as a function of the beam energy. *Middle:* Ratio of paddle counts and $N_{\gamma,0}$ from known transitions. Solid (open) squares indicate that data from [63] ([104]) was used. The lines show the result of a linear fit to the data points. *Bottom:* Determined scaling factor $N_{\gamma,0}$. The data points at high energy (marked in Table. 4.2) are determined by extrapolation. An additional uncertainty of 20% has been assigned.

Table 4.2: Determined values for the photon flux $N_{\gamma,0}$ for each energy setting. Values have been calculated using known cross-sections from [63] and [104]. Values at high energy (as indicated) have been extrapolated as described in Sec.4.1.6.

E_{beam} [MeV]	$N_{\gamma,0}$ $[1 \times 10^{10}\gamma]$[a]	$N_{\gamma,0}$ $[1 \times 10^{10}\gamma]$[b]
5.2	31.8(6)	43.6(17)
5.4	18.1(16)	25.8(5)
5.6	44.4(21)	57.7(19)
5.9	41.4(52)	68.8(53)
6.1	46.2(18)	69.2(22)
6.3	47.6(26)	76.0(16)
6.5	55.8(20)	95.1(18)
6.8	42.4(56)	85.7(27)
7.15	30.6(76)	79.8(32)
7.4	25.7(46)	42.1(17)
7.7	44.6(92)[c]	84.9(91)
8.0	36.0(105)[c]	66.8(134)[c]
8.3	46.7(97)[c]	88.7(213)[c]

[a] Determined with data from S. Volz [63]
[b] Determined with data from C. Romig [104]
[c] Extrapolated values

indicate the values extrapolated from [104]. Since the data from [104] extends to slightly higher energies, and includes more transitions in the full energy range, they will be used for the photon flux in the following analysis.

4.2 Singles spectra

Singles spectra for the HPGe detectors were recorded with the GENIE data acquisition. In addition, $LaBr_3$:Ce singles spectra are produced from the recorded MBS list mode data. They have been used for the determination of the ground state branching ratio, and for energy calibration of these detectors.

4.2.1 Angular distributions

In Chapter 2 the analytic description for angular distribution of a γ-ray emitted from a nuclear state was introduced. To be able to sum up spectra from different detectors and to obtain parities and total cross-sections, the angular distributions have to be taken into account. The probability to detect a photon γ_1 in the direc-

tion (θ_1, φ_1) from an excited state J_0 is given by Equation (2.16). This equation can be simplified for the transitions that occur during the analysis:

$$W_{0^+\to1^+\to0^+}(\theta,\varphi) = 1 + \frac{Q_2}{4}\left[\left(3\cdot\cos^2\theta - 1\right) + \cos 2\varphi \cdot 3 \cdot \left(1 - \cos^2\theta\right)\right] \quad (4.13)$$

$$W_{0^+\to1^-\to0^+}(\theta,\varphi) = 1 + \frac{Q_2}{4}\left[\left(3\cdot\cos^2\theta - 1\right) - \cos 2\varphi \cdot 3 \cdot \left(1 - \cos^2\theta\right)\right] \quad (4.14)$$

$$W_{0^+\to1^+\to2^+}(\theta,\varphi) = 1 + \frac{Q_2}{40}\left[\left(3\cdot\cos^2\theta - 1\right) + \cos 2\varphi \cdot 3 \cdot \left(1 - \cos^2\theta\right)\right] \quad (4.15)$$

$$W_{0^+\to1^-\to2^+}(\theta,\varphi) = 1 + \frac{Q_2}{40}\left[\left(3\cdot\cos^2\theta - 1\right) - \cos 2\varphi \cdot 3 \cdot \left(1 - \cos^2\theta\right)\right] \quad (4.16)$$

Attenuation factors Q_2 (see below in Section 4.3.2) have been introduced to take into account the finite opening angle of the detector. It is clear from the equations that the angular distribution in the case of a decay to an excited 2^+ state is much more isotropic compared to the case of a decay to the ground state or an excited 0^+ state. This fact can be useful in the analysis, when separating the decays to the 0_2^+ and the 2_1^+ state, which have an energy difference of only 307 keV.

4.2.2 Extraction of cross-sections

The energy integrated cross-sections I_i for each investigated transition are obtained directly from Equ. (2.8), when the detection efficiency is determined as described in Section 4.1.3, the number of photons as shown in Section 4.1.6, and the angular correlation is taken from Section 4.2.1. The number of target nuclei N_T is determined from the target thickness shown in Table 4.1. The energy integrated cross-section is determined according to:

$$I_{j\to k}(E_i) = \frac{A_i}{N_T \cdot \epsilon_{tot}(E_i) \cdot N_\gamma \cdot W_{eff}(\theta,\varphi,\Delta\Omega)}\,. \quad (4.17)$$

In addition it is possible to determine the total photo-absorption cross-section from the HPGe singles data, when the sum of all integrated cross-sections determined from individual states is calculated:

$$\sigma(E) = \frac{1}{\Delta E}\sum_{E_i\in\Delta E} I(E_i) \quad (4.18)$$

The sum is normalised by dividing by the energy interval ΔE that contains the states that have been taken into account for the sum. For each particular beam energy setting, one value for σ is determined.

4.2.3 Parity measurement

A standard technique for parity measurement involves measuring the emitted radiation from several different angles. It is clear from equations 4.14 and 4.13,

that measuring the emitted radiation from the two angles (θ, φ) of $(\pi, 0)$ and (π, π) is sufficient to distinguish between positive ($0_1^+ \rightarrow 1^+ \rightarrow 0_1^+$) and negative parity ($0_1^+ \rightarrow 1^- \rightarrow 0_1^+$) for the excited state. The respective angular distributions are displayed in the top row of Figure 2.2. The experimental asymmetry

$$\epsilon = \frac{N_H - N_V}{N_H + N_V} \tag{4.19}$$

with the efficiency corrected peak areas from the horizontal (N_H) and the vertical (N_V) detectors is an optimal discriminator for the two cases. For the two positions mentioned before the asymmetry is ± 1 for $J^\pi = 1^\pm$ states in case of infinitesimally small detectors at $(\pi, 0)$ and (π, π). In the γ^3 setup the detectors were positioned at different angles for the two different beam times in 2012 and 2013 as illustrated in Figure 3.4. The placement of the HPGe detectors at backward angles ($\theta = \frac{3}{2}\pi$) reduces the asymmetry from ± 1 to $\pm 1/3$. The finite opening angle of the detectors ($Q_2 > 1$) further reduces the the asymmetry to ± 0.70 for the 2013 data and ± 0.3 for the data from 2012.

4.2.4 Branching ratios to excited states

From the singles spectra it is not only possible to investigate direct transitions back to the ground state (shown in red in Fig. 4.16), but in addition the fraction of inelastic transitions, which populate the low-lying excited states (shown in blue in Fig. 4.16), can be determined. The extraction of branching ratios for individual states is difficult, because the sensitivity for these transitions is usually not sufficient in the singles data. The low-lying excited states show a strong population, even though they are not directly excited in the HIγS experiments. In most cases these states themselves decay with a high probability to the 2_1^+ state. Therefore, the population intensity of the 2_1^+ can be used to measure the average branching ratio from the excitation energy region to other excited states. In recent experiments [30, 32, 66] this method was used to determine the inelastic part of the photo-absorption cross-section. The average branching ratios to excited states are determined from the peak areas of the decays of the low-lying excited 2^+ states. The obtained numbers can only be an estimate, because these 2^+ states need not necessarily be populated directly from the initial state, but can also be part of a multi-step cascade. This leads to systematically higher values for the obtained average branching ratios.

4.3 Analysis of γ-γ coincidence data

From the MBS list mode data it is possible to select only events that satisfy the coincidence condition (see Section 4.1.4) and create 2D energy histograms

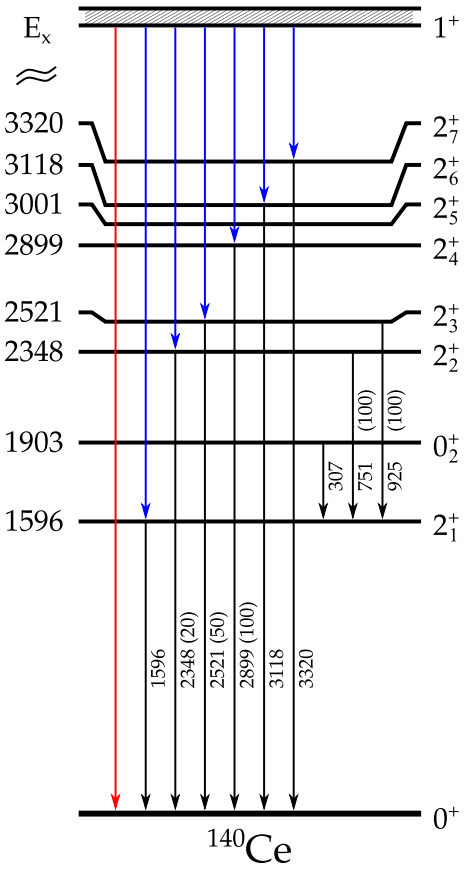

Figure 4.16: Simplified level scheme of ^{140}Ce, showing the important transitions encountered in the analysis. Coloured arrows indicate primary transitions from the excitation region (E_x) to the ground state (red) and to excited states (blue). Secondary transitions are shown as black arrows with the associated photon energy and their relative intensity (from NNDC [105]).

(or coincidence matrices) for any pair of detectors. Combinations of the type HPGe-HPGe, HPGe-LaBr, and LaBr-LaBr are possible. Figure 4.17 shows such matrices for the sum of coincidences between any HPGe detector and any LaBr detector on the left, and the corresponding matrices for coincidences between any two LaBr detectors. The beam energy progresses from 5.2 MeV to 8.3 MeV. These energies will serve as an example to illustrate the following analysis steps, which have been performed in an analogue manner with all measured energies. In the 8.3 MeV energy setting the CFD thresholds at about 500 keV for the HPGe detectors and at 1 MeV for the LaBr detectors suppress the low-energy signals. Concentrations of events are visible as vertical and horizontal lines in the matrix. These usually correspond to the decay of a low-lying state in coincidence with the detection of a primary photon emitted from a state in the excitation region. The most prominent lines are at an energy of 1.596 MeV, i.e. the energy of the 2_1^+ state (see Fig. 4.16 for reference). In the direction of the x-axis the lines are thinner compared to those in the direction of the y-axis, which is due to the different energy resolution of the two detector types. The main differences in the LaBr-LaBr matrices compared to the HPGe-LaBr case are directly visible: The energy resolution of the $LaBr_3$:Ce detectors is much lower resulting in broad lines in both directions. On the other hand the high detection efficiency results in

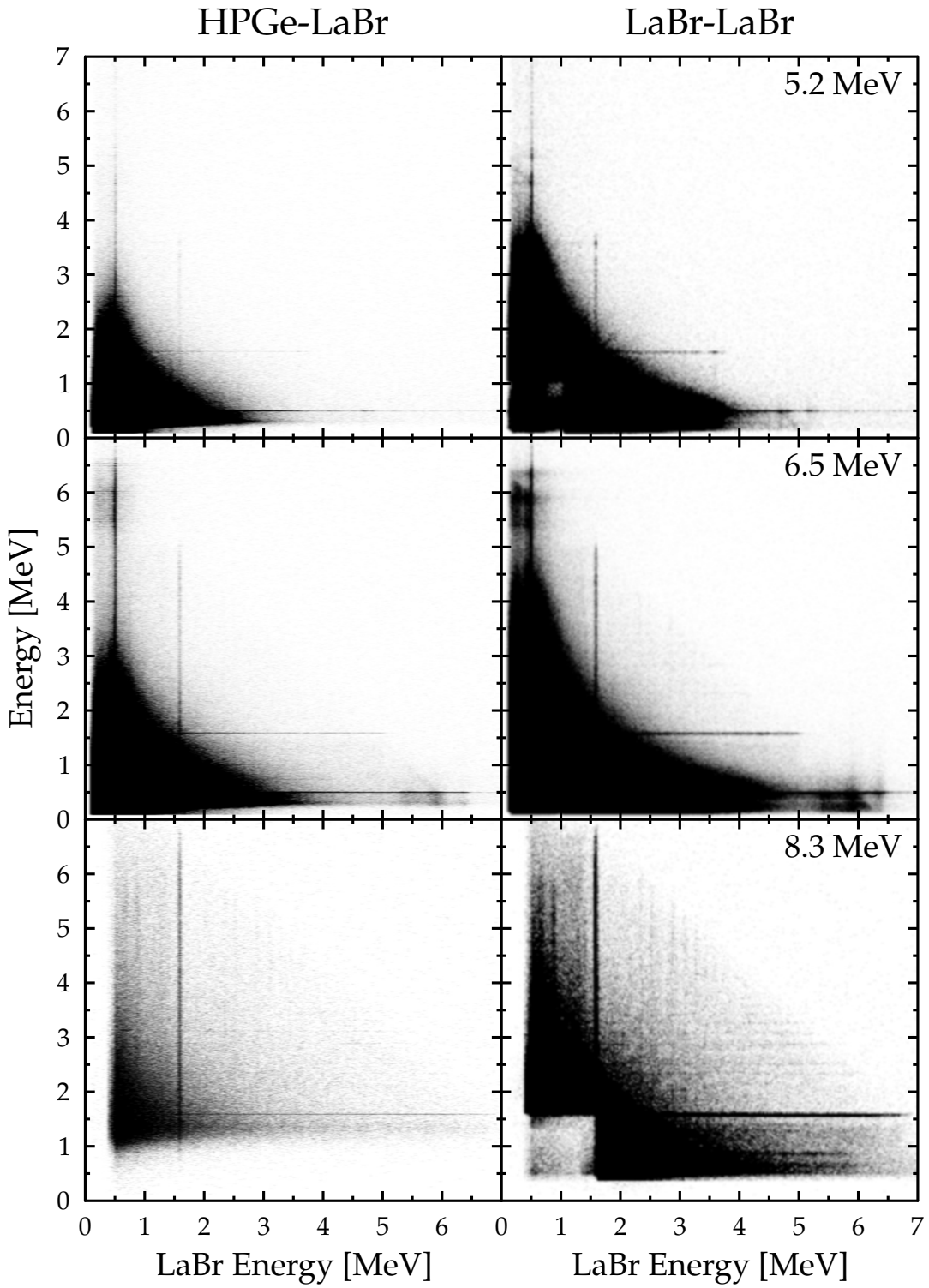

Figure 4.17: Matrices containing coincident events between any HPGe and LaBr detector (left) and between LaBr and LaBr detectors (right). The beam energy is 5.2 MeV (top), 6.5 MeV (middle), and 8.3 MeV (bottom).

better statistics, especially at higher photon energies. At higher beam energies, this leads to a better visibility of many more lines that correspond to the decay from other low-lying (2^+) states.

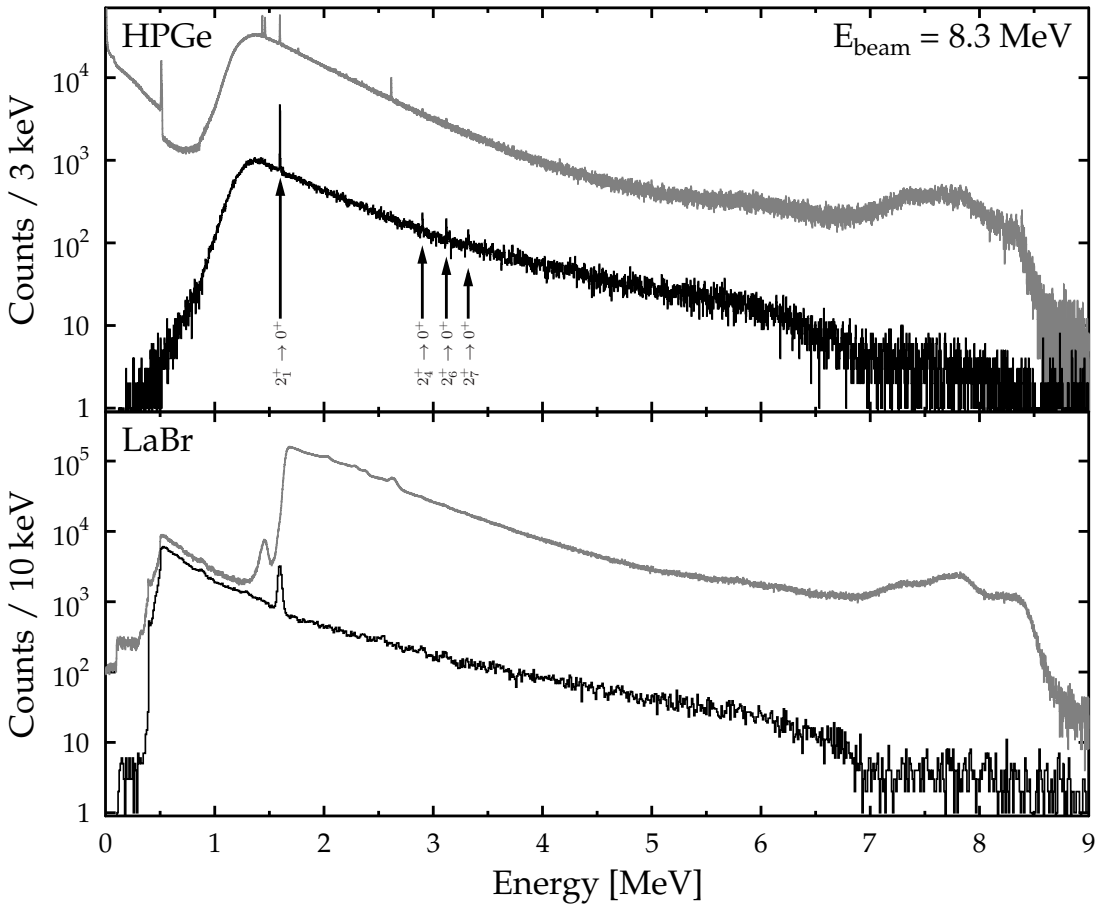

Figure 4.18: Projections of the coincidence matrix from Fig. 4.17 at 8.3 MeV on the y-axis (HPGe, Top), and on the x-axis (LaBr, Bottom). Singles spectra are shown in grey as a reference. A few of the transitions from low-lying states to the ground state are visible.

4.3.1 Projected spectra

From the data in the coincidence matrix a slice is projected out into a new energy-gated spectrum. If the matrices from Fig. 4.17 are considered, two possible projections are meaningful: At first the projection can be done over the complete x- or y-axis, thus summing up all the entries in the matrix, and producing the spectra shown in Fig. 4.18. In comparison to the singles spectra (drawn in grey colour), the peaks from elastic decays are suppressed and the continuous background contribution is greatly reduced. In the HPGe spectrum some low-

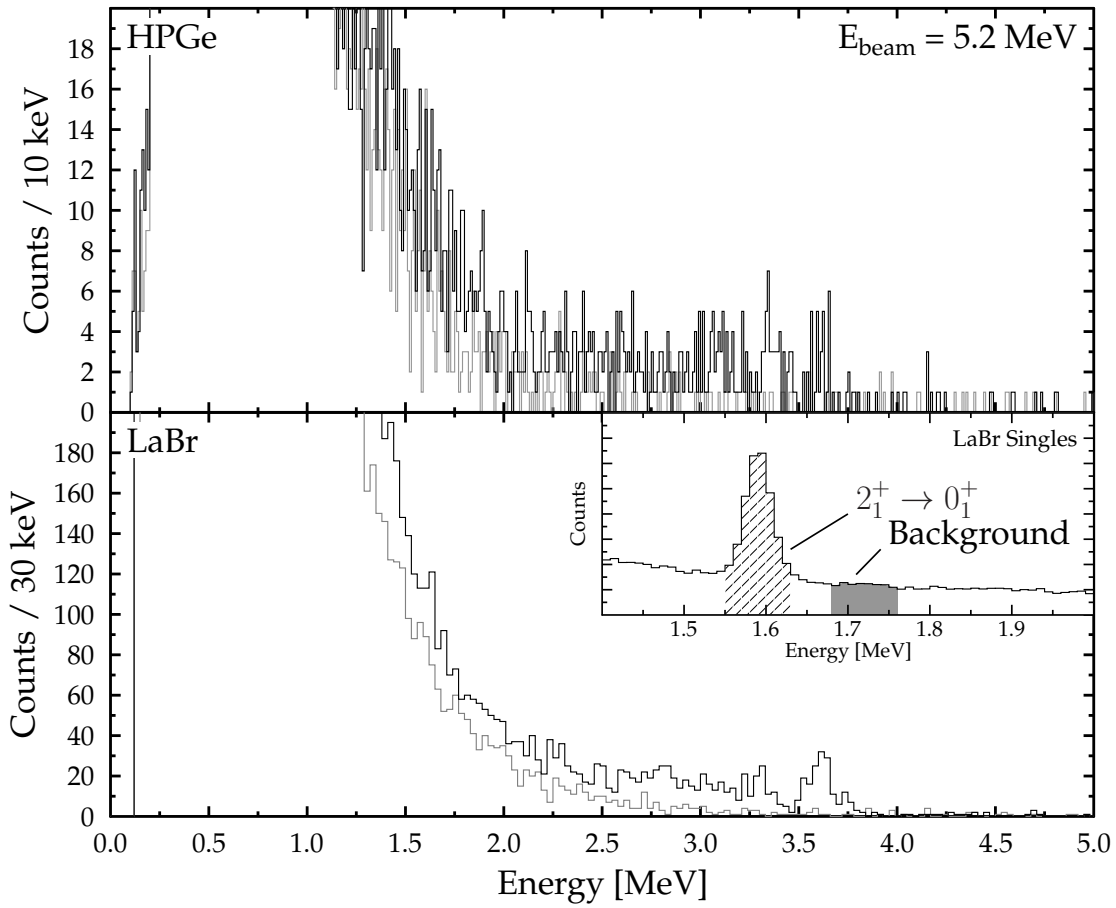

Figure 4.19: Energy gated spectra from a cut on the decay of the first 2^+ in the coincidence matrices at a beam energy of 5200 keV. The resulting spectrum after the cut (black) and the spectrum with a cut in the background region next to the peak are shown (grey). The inset shows the two different cut ranges to produce the spectrum corresponding to the coincidence (shaded), and the background spectrum (solid grey).

energy transitions are visible that were indistinguishable from the background in the singles spectrum.

A projection on the y-axis (HPGe) over only a small energy interval in the x-direction (LaBr) acts as a more restrictive condition on the energy that was detected in the LaBr detector. The same can be done for the HPGe detector. If the selected energy range corresponds to the energy of a low-energy transition, such as for example from the first 2^+ excited state, the projected spectrum contains almost exclusively peaks at energies corresponding to the transitions that populate this specific low-energy state. Such projected spectra are shown in Figs. 4.19 and 4.20. The energy selection was done by selecting all events in a 2σ region around the mean energy of the first 2^+ state in the HPGe-LaBr matrix and the LaBr-LaBr matrix, respectively. The black spectra are the result of the cut, and

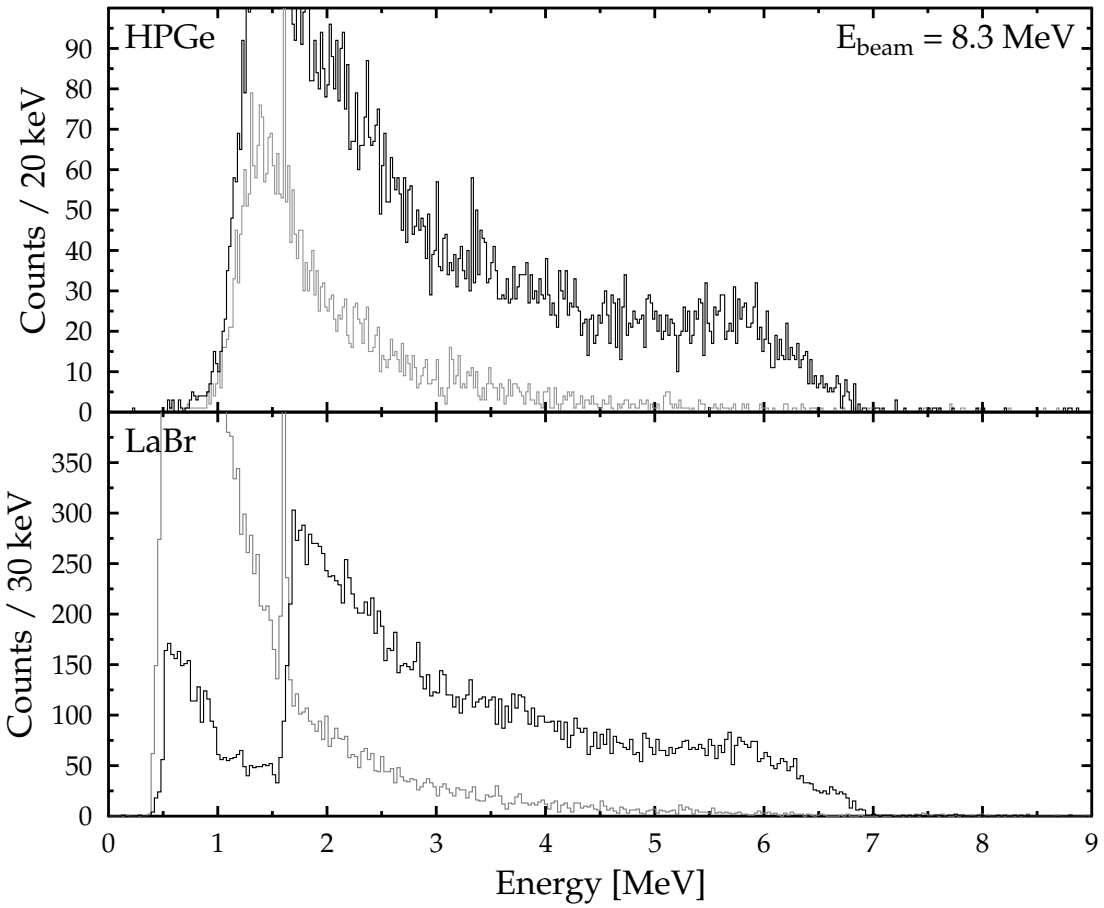

Figure 4.20: Energy gated spectra from a cut on the decay of the first 2^+ in the coincidence matrices at a beam energy of 8300 keV. The resulting spectrum after the cut (black) and the spectrum with a cut in the background region next to the peak are shown (grey).

the grey spectra are the result of a cut on the background. The background cut was done with an additional energy cut on the same matrix, but 4σ higher in energy, next to the 2^+ peak (see inset in Fig. 4.19 to see the different cut ranges). Low energy events are suppressed using a CFD threshold at about 1.6 MeV in the $LaBr_3$:Ce spectrum in the lower part of Fig. 4.20, leading to a different structure in the low-energy part of the energy-gated spectrum. From the figures it is apparent that the background contribution in the excitation region is very small compared to the contribution from the primary decays into the low-lying excited states. The spectra contain mainly the primary decays including the detector response. In Fig 4.19 the structure of the detector response with a full-energy peak and single-escape peak is clearly visible. Due to the high level density and low statistics, single states can only be resolved in a few cases, even in the HPGe spectra. Average values are determined otherwise.

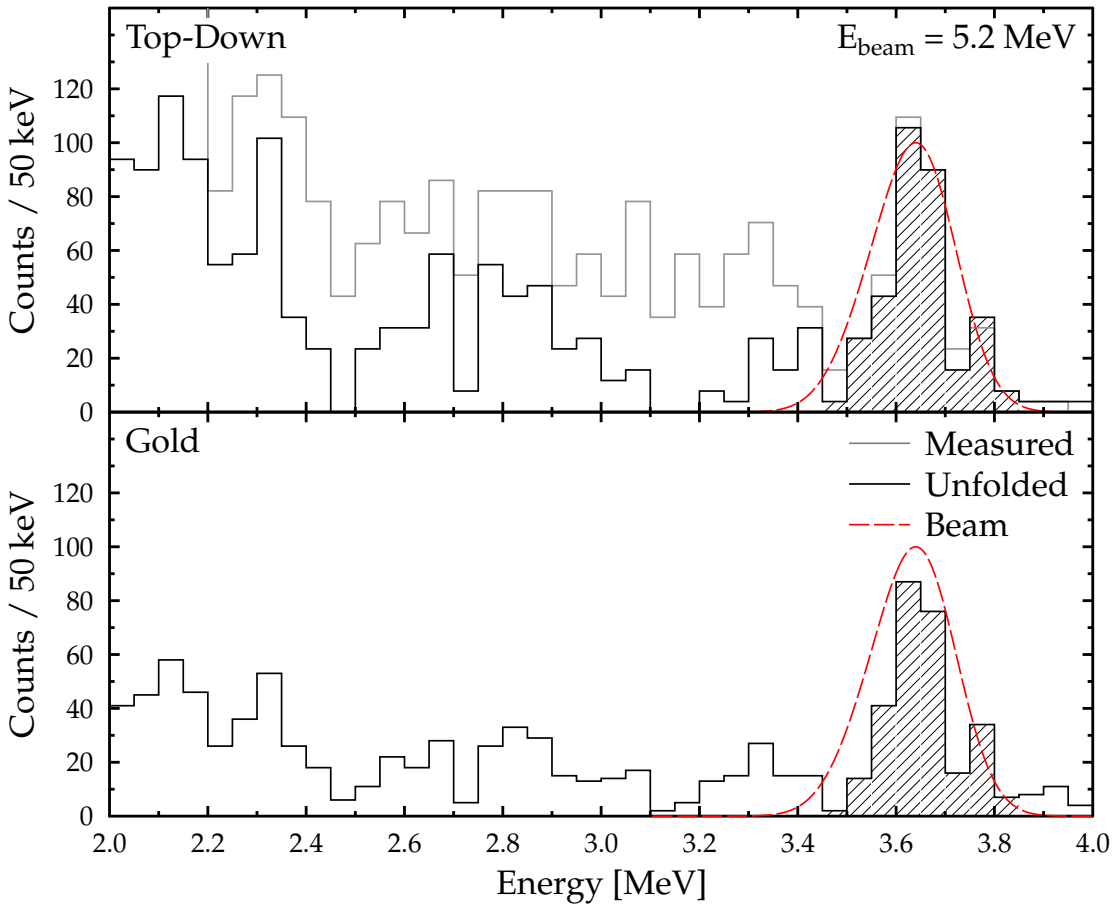

Figure 4.21: Unfolded energy gated spectra for the beam energy 5.2 MeV. *Top:* Measured spectrum (grey) shown together with unfolded spectrum using the Top-Down method (black) and the beam shape (red,dashed) shifted by the energy of the first 2^+ state. *Bottom:* Same spectrum, but unfolded using the Gold method.

To be able to integrate the full-energy peak region in the energy gated spectra, the detector response has to be removed by spectrum unfolding. The appropriate methods were already described in Section 4.1.1. After applying the two different unfolding methods to the $LaBr_3$:Ce spectra from Fig. 4.19, the resulting unfolded spectra are shown together with the measured spectra in Fig. 4.21. The red dashed line indicates the energy profile of the photon beam, shifted by the energy of the first 2^+. A clear peak at the energy corresponding to the energy of the primary transitions (marked with blue arrows in Fig. 4.16) is visible. From these unfolded spectra the integrated cross-section for the decay to the first 2^+, averaged over the excitation energy region, is determined by integrating this peak. For this purpose the spectra are integrated in the region marked in Fig. 4.21 with the red dashed line. The resulting peak areas are in this case

321(36) for the Top-Down unfolded spectrum, and 270(34) for the Gold unfolded spectrum.

4.3.2 Angular correlation

In Chapter 2 the analytic description for angular correlations of two γ-rays emitted from the same nuclear state was introduced. To obtain branching ratios and cross-sections for the inelastic decays, the angular correlations have to be taken into account. The probability to detect a photon γ_1 in the direction (θ_1, φ_1) from an excited state J_0 is given by Equ. (2.16). However, in the case of coincidence measurements, the directional distribution of the second photon γ_2 emitted in a cascade strongly depends on the emission direction of the primary photon (as illustrated in Fig. 2.2). Therefore the angular correlation function from Equ. (2.19) must be used. For each pair of detectors at the angles (θ_1, φ_1) and (θ_2, φ_2) a value for the angular correlation is calculated and used in the analysis. To take into account the finite solid angle of the detectors, the angular correlation is attenuated using the formalism adopted from [76] (Chapter 14, Section 2). Attenuation coefficients Q_{λ_i} are introduced in the angular correlation (Equ. (2.19)), which leads to

$$W(\theta_1\varphi_1\theta_2\varphi_2) = \frac{d\Omega_1\, d\Omega_2}{4\pi} \sum_{\substack{\lambda_0 q_0 \lambda_1 q_1 \lambda_2 q_2 \\ \lambda_1,\lambda_2=\text{even}}} (-1)^{\lambda_1+\lambda_2}(2J_0+1)^{1/2}\rho^{\lambda_0}_{q_0}(J_0)A^{\lambda_2\lambda_0}_{\lambda_1}(\gamma_1)Q_{\lambda_1} \times A_{\lambda_2}(\gamma_2)Q_{\lambda_2}\begin{pmatrix}\lambda_2 & \lambda_1 & \lambda \\ q_2 & q_1 & q\end{pmatrix}(2\lambda_2+1)^{-1/2}Y_{\lambda_1 q_1}(\theta_1\varphi_1)Y_{\lambda_2 q_2}(\theta_2\varphi_2). \tag{4.20}$$

The attenuation coefficients are calculated according to

$$Q_\lambda = J_\lambda / J_0 \tag{4.21}$$

where the coefficients J_λ depend on the maximum angle γ of a photon that enters the detector with respect to the detector axis:

$$J_0 = (1 - \cos\gamma) \tag{4.22}$$

$$J_2 = \frac{1}{2}\cos\gamma(1 - \cos^2\gamma) \tag{4.23}$$

$$J_4 = \frac{1}{8}(-3\cos\gamma + 10\cos^3\gamma - 7\cos^5\gamma) \tag{4.24}$$

Table A.3 in Appendix A.2 summarises the calculated values for all detector combinations for the transitions $(0^+ \to 1^- \to 2^+ \to 0^+)$ and $(0^+ \to 1^+ \to 2^+ \to 0^+)$.

4.3.3 Extraction of branching ratios

The ratio of the radiation width Γ_i for the decay to a final excited state J_f to the total radiation width Γ of a state at energy E (abbreviated simply as *branching ratio*) is defined for single states as

$$b_i(J_f, E) = \frac{\Gamma_i}{\Gamma} = \frac{\Gamma_i \frac{\Gamma_0}{\Gamma}}{\Gamma \frac{\Gamma_0}{\Gamma}} = \frac{\Gamma_0 \Gamma_i / \Gamma}{\sum_j \Gamma_0 \Gamma_j / \Gamma} \,. \tag{4.25}$$

Only the relative radiation widths $\Gamma_0\Gamma_i/\Gamma$ are experimentally accessible, such that the branching ratio has to be expressed in terms of these quantities. Since the energy integrated cross-section is proportional to the relative radiation width $\Gamma_0\Gamma_i/\Gamma$, b_i can be expressed in terms of these cross-sections as well:

$$b_i(J_f, E) = \frac{I_{\text{inelastic}}(J_f, E)}{I_{\text{total}}(E)} \,. \tag{4.26}$$

If the detector resolution does not allow separating peaks belonging to single transitions, only average branching ratios can be extracted. This applies for example to the projected $LaBr_3$:Ce spectra. In this case the average branching ratio over an energy interval ΔE represents the ratio of the sum of the relative radiation widths, and also the ratio of the averaged inelastic and total integrated cross-section:

$$\langle b_i(J_f, E)\rangle_{\Delta E} = \frac{\langle \Gamma_0 \Gamma_j / \Gamma \rangle_{\Delta E}}{\langle \Gamma \rangle_{\Delta E}} = \frac{\sum_{E_i \in \Delta E} \Gamma_{0,i} \Gamma_{j,i} / \Gamma_i}{\sum_{E_i \in \Delta E} \Gamma_i} = \frac{\langle I_{\text{inelastic}}(J_f, E)\rangle_{\Delta E}}{\langle I_{\text{total}}(E)\rangle_{\Delta E}} \tag{4.27}$$

This quantity can not be determined directly from the singles data. Only the average integrated cross-section to the ground state $\langle I_{gs}(E)\rangle$ is determined either from the unfolded $LaBr_3$:Ce singles spectra (see e.g. Fig. 4.1) or from the HPGe singles data. The average integrated cross-section to excited states $\langle I_{\text{inelastic}}(E)\rangle$ can be estimated from the decay of low-lying excited states (see Sec.4.2.4). This allows to determine the average total integrated cross-section to the ground state $\langle I_{\text{total}}(E)\rangle$ from the sum of the former two quantities. Together with the inelastic part the average ground state branching ratio

$$\langle b_0 \rangle = \frac{\langle I_{gs}(E)\rangle}{\langle I_{gs}(E)\rangle + \langle I_{\text{inelastic}}(E)\rangle} \tag{4.28}$$

is determined.

From the coincidence data it is possible to directly determine branching ratios of the states in the excitation region to individual low-lying states, and investigate the decay behaviour of these states. The quantity

$$\langle b_i(J_f, E)\rangle_{\Delta E} = \frac{\langle I_{\text{inelastic}}(J_f, E)\rangle_{\Delta E}}{\langle I_{\text{total}}(E)\rangle_{\Delta E}} \tag{4.29}$$

is directly accessible. The average integrated cross-section to individual excited states $\langle I_{inelastic}(J_f, E)\rangle$ is determined from the unfolded energy-gated spectra (see Fig. 4.19).

Chapter 5

Experimental results for ^{32}S

In this chapter the results from the analysis of the ^{32}S data are presented. Using the data set recorded during the commissioning beam times in 2012 and 2013 it was possible to determine the branching ratio of the 1^+ state at 8.125 MeV in a direct way and to unprecedented precision. The results from both measurements can be compared, to check that the analysis has been carried out in a consistent way.

The branching ratio is determined in a number of ways, due to the use of different detector types and the comparatively large amount of data collected. Comparison of the determined values from different detector combinations yields important information about the performance of the γ^3 setup and shows in addition which level of sensitivity can be expected in the investigation of other nuclei.

5.1 Branching ratio

At first the branching ratio of the 1^+ state at 8.125 MeV can be determined directly from the singles spectra, since the 1^+ state shows a rather strong branching transition to the 2_1^+ state [106]. A simplified level scheme for ^{32}S is shown in Fig. 5.1, which illustrates the important transitions: The nucleus is excited with a beam energy of 8.125 MeV to the 1^+ state. It can then decay either directly back to the ground state, or with a probability of 14 % via a cascade through the first excited state ($1^+ \rightarrow 2_1^+ \rightarrow 0_1^+$). The decay via the 0_2^+ state and higher excited states is less probable. Figure 5.2 shows the recorded HPGe spectrum in the top part, and the peaks corresponding to the transitions of interest are marked. Since the transition energies are well-separated, the singles spectra from the $LaBr_3$:Ce detectors (top part of Fig. 5.3) can be analysed in a similar way. As a measure for the branching ratio b the intensity of the transition to the 2_1^+ state relative to the strongest transition to the ground state was determined. Taking into account the detector efficiency and the angular correlation of the emitted radiation, the

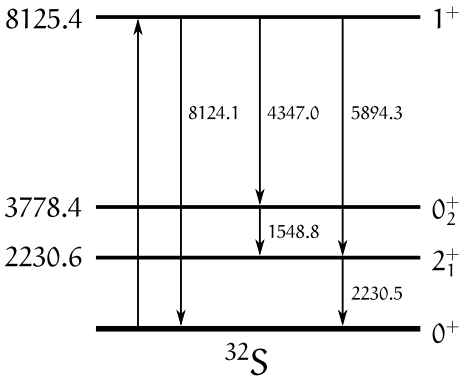

Figure 5.1: Simplified level scheme of ^{32}S, showing the important transitions which are discussed. Energies are displayed in keV.

Table 5.1: Values for the branching ratio for the transition $1^+ \rightarrow 2^+_1$ in ^{32}S determined from singles spectra and coincidences from the data taken in 2012 and 2013. Values are given relative to the intensity of the ground state transition. The errors in brackets are of pure statistical nature.

b [%]	E_γ [keV]	2012	2013	Babilon *et al.*	ENSDF
HPGe Singles	5894	17.5(13)	16.8(6)	16(4)	18(6)
$LaBr_3$:Ce Singles	5894	17.1(3)	16.4(7)		
HPGe-LaBr Coinc	5894	–	18.0(3)		
LaBr-LaBr Coinc	5894	16.6(10)	22.7(5)		

values for the relative branching ratio b in Table 5.1 are determined according to:

$$b = \frac{A(5894)}{A(8125)} \cdot \frac{\epsilon(8125)\, W(\theta, \varphi, 1^+ \rightarrow 0^+_1)}{\epsilon(5894)\, W(\theta, \varphi, 1^+ \rightarrow 2^+_1)} \tag{5.1}$$

These values agree with each other within their statistical error margins, such that any systematical uncertainties seem to play only a minor role. As a comparison the values determined by Babilon *et al.* [106] and from the evaluated nuclear structure data file (ENSDF) [107] are also shown in the table.

The determination of the branching ratio from singles spectra is in many cases not feasible, because the involved transition probabilities are much smaller than for this test case. In addition, a higher level density in the energy range, where the nucleus is excited, leads to a higher background from the detector response in the energy range of the inelastic transitions. Therefore the experimental sensitivity for measuring the inelastic transitions in singles spectra is usually not sufficient.

The method of γ-γ coincidences increases the experimental sensitivity, because ground state transitions are removed from the spectrum and background contributions are strongly suppressed. In the γ^3 experimental setup three different detector configurations for coincidence measurements are possible: Coincidences between any two $LaBr_3$:Ce detectors, or between any two HPGe de-

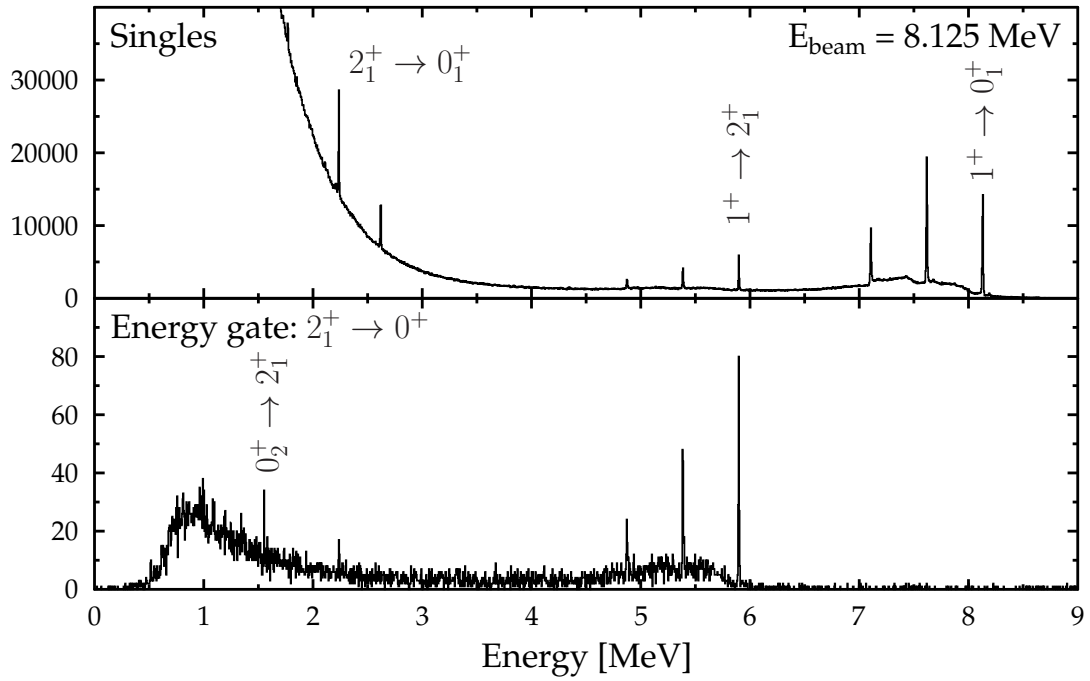

Figure 5.2: HPGe detector energy spectra of ^{32}S at a beam energy of 8.125 MeV. *Top:* Measured HPGe singles spectrum with ^{32}S target. *Bottom:* Coincidence spectrum (HPGe-LaBr) with energy gate condition on the transition $2_1^+ \rightarrow 0_1^+$.

tectors, or using any combination of $LaBr_3$:Ce and HPGe detectors. The coincidence requirement is such, that the energy of one of the detected photons must equal the energy difference of the $2_1^+ \rightarrow 0_1^+$ transition. The resulting HPGe and $LaBr_3$:Ce spectra are shown in the bottom part of the Figs. 5.2 and 5.3. These are almost background free spectra, showing exclusively the decay from the 1^+ to the 2_1^+. In addition, both energy gated spectra show another transition that was invisible in the singles spectra because of the large background contribution. This transition at an energy of 1.548 MeV corresponds to the decay of the 0_2^+ level to the 2_1^+ state. A small peak at the energy of the 2_1^+ is still visible in the energy gated spectra, because a certain amount of background is present within the energy gate below the peak. Those events are mainly part of the Compton continuum of transitions at higher energies, which are in coincidence with the decay of the 2_1^+. The values for the branching ratio determined from coincidence data are also summarised in Table 5.1. The results from the measurements in 2012 and 2013 are comparable within their statistical errors, which shows that the analysis has been performed in a consistent way. This fact is important for the analysis of the ^{140}Ce data, because the final result is based on data from both experimental campaigns.

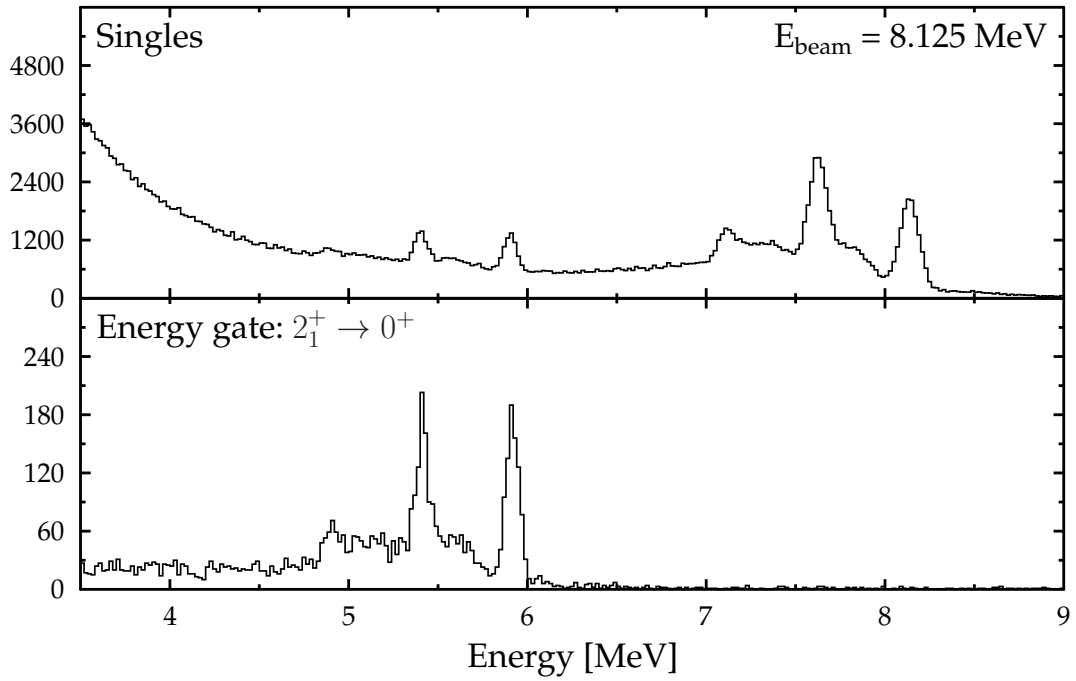

Figure 5.3: $LaBr_3$:Ce detector energy spectra of ^{32}S at a beam energy of 8.125 MeV. *Top:* Measured $LaBr_3$:Ce singles spectrum with ^{32}S target. *Bottom:* Coincidence spectrum (LaBr-LaBr) with energy gate condition on the transition $2_1^+ \rightarrow 0_1^+$.

5.2 Angular distributions

The angular distribution of the emitted photons in a specific transition is directly measured from the ratio of the efficiency corrected peak areas in the spectra. Taking any two detectors i and j, the ratio R is defined as

$$R = \frac{W(\theta_i, \varphi_i)}{W(\theta_j, \varphi_j)} = \frac{A_i}{A_j} \cdot \frac{\epsilon_j}{\epsilon_i} \tag{5.2}$$

with the peak areas A_i and full-energy peak efficiency ϵ_i. The measured ratio is compared to the theoretical ratio that is expected for the transition and the positions of the two detectors. In Fig. 5.4 the ratio R is plotted over the polar angle of the second detector φ for 5 different cases encountered in the singles spectra from 2012. The upper row shows the ratio measured with the backwards (HPGe) detectors at an angle $\theta = \pi/4$. The data for the transition at 8.125 MeV is shown in (a), for the one at 5.894 MeV in (b), and for the transition at 2.230 MeV in (c). The lower row shows the ratio for the $LaBr_3$:Ce detectors at $\theta = \pi/2$ for the first two transitions. Here the transition at 2.230 MeV ($2_1^+ \rightarrow 0_1^+$) was not analysed, because of the large background contribution in the spectra in this energy range. In each of the five cases the corresponding theoretical ratio of the angular distribution for the transition is shown as a solid line (see also Fig. 2.2).

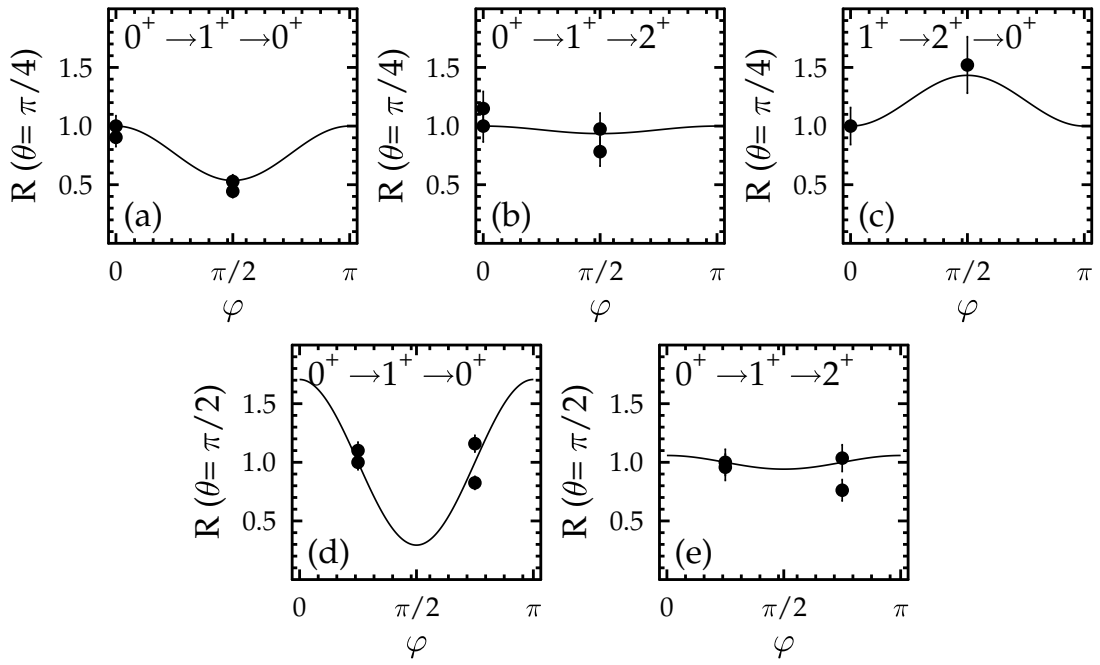

Figure 5.4: Measured angular distribution of emitted photons from ^{32}S in singles spectra. Shown is the ratio R = W_1/W_i over the angle φ between the two detectors. (a), (b) and (c) show R for azimuthal angle θ = $\pi/4$, while (e) and (f) show R for θ = $\pi/2$.

This analysis shows, that the using the data from the backwards detectors the three different angular distributions can be distinguished, while the $LaBr_3$:Ce detectors were positioned in such a way that the data fits any of the distributions.

The availability of γ-γ coincidences allows a more in-depth study of the angular correlations of two emitted photons in a cascade. As shown in Sec. 2.2.3, the angular distribution of the second photon depends strongly on the direction of the primary photon (see panels (e) and (f) in Fig. 2.2). This effect can now be studied by investigating the ($0_1^+ \rightarrow 1^+ \rightarrow 2_1^+ \rightarrow 0_1^+$) transition in the coincidence spectra. The direction of the first photon from the transition ($1^+ \rightarrow 2_1^+$) is determined by observing it in one of the detectors at θ = $\pi/2$. In the analysis this is done by creating an energy gate condition for the energy corresponding to this transition (5.894 MeV). Four cases are discussed here, namely the detection of the first photon at an angle φ = 0 or at φ = $\pi/2$, and the detection of the second photon either at θ = $\pi/2$ or at θ = $\pi/4$. The secondary transitions ($2_1^+ \rightarrow 0_1^+$) observed in the energy-gated spectra of the other detectors reflect the angular correlation. The efficiency corrected peak areas corresponding to this transition are used to determine the angular correlation. In Fig. 5.5 the resulting value of the angular distribution W for these cases is shown. The solid line indicates the theoretical calculation according to Equ. 2.19. For the measured values the energy gate was done with the LaBr3 and LaBr4 detectors, observing the pri-

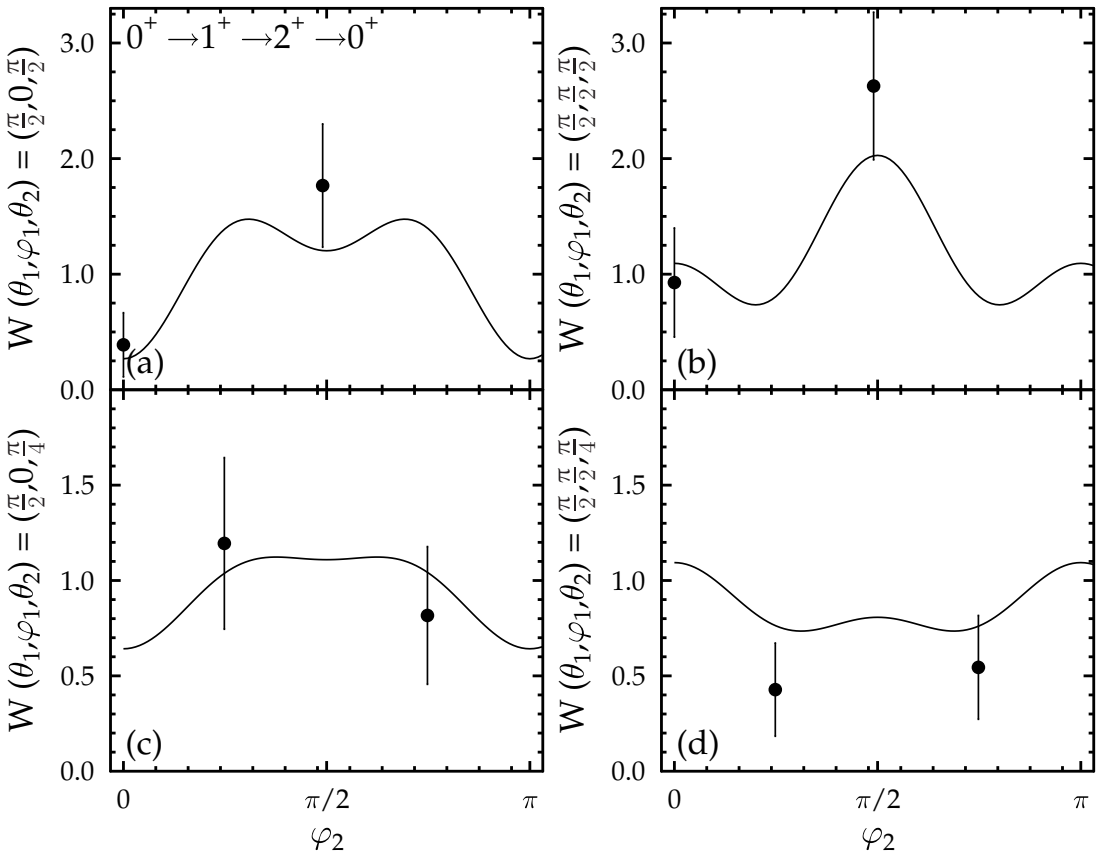

Figure 5.5: Measured angular distribution of emitted photons from ^{32}S in coincidence spectra, with the condition that the primary photon was detected at $(\theta, \varphi) = (\pi/2, 0)$ and $(\theta, \varphi) = (\pi/2, \pi/2)$. Shown is the angular distribution $W(\theta_1, \varphi_1, \theta_2, \varphi_2)$ as a function of the polar angle φ_2 of the second detector.

mary transition (θ_1, φ_1) at an angle of $\varphi_1 = 0$ (left column) and at an angle of $\varphi_1 = \pi/2$ (right column), while the secondary transition was observed in the HPGe detectors (θ_2, φ_2) at an angle of $\theta_2 = \pi/2$ (top row) and at an angle of $\theta_2 = \pi/4$ (bottom row). Even though only two data points were determined for each case, a clear difference is observed. In addition, the resulting values are close to the expected value from the theoretical calculation. The investigation of the coincidence data shows, that it is necessary to take angular correlations of the emitted photons into account. However, this is only feasible, if sufficient statistics are accumulated in coincidence spectra.

Chapter 6

Experimental results for ^{140}Ce

The experimental results presented in this chapter are based on the measurements carried out during the γ^3 campaigns in 2012 and 2013. At the HIγS facility the 2.3 g ^{140}Ce target was irradiated with photons at 13 different beam energy settings covering an energy range from 5.2 MeV to 8.3 MeV. Singles data as well as coincidence data were recorded with the γ^3 setup as described in Chapter 3. The analysis performed on the data to yield the results below is described in detail in Chapter 4. This chapter first focuses on the results from the singles data. New electric dipole states have been discovered throughout the complete energy range due to the increased sensitivity and the comparatively long measurement time. Parities for most of these states and B(E1) strengths have been determined. The coincidence data allows to extract discrete as well as average branching ratios for the transitions to low-lying excited states.

6.1 Nuclear levels

In the analysis of the singles data from the GENIE data acquisition system ground state transitions from a total of 210 distinct $J = 1$ states were measured. So far, 42 of these states were already known and are published in [63]. Table A.1 in Appendix A.1 lists all states in detail. Figure 6.1 shows the individual B(E1) strengths in comparison to the values from Volz *et al.* [63] as a function of the excitation energy. As described in Sec. 4.1.6, the known values of [104] are used in the present analysis for the absolute normalisation. In Tab. A.1 the states used for the normalisation are marked. The total B(E1) transition strength is calculated according to Equ. 2.9 as the sum of the B(E1) strengths of the individual transitions:

$$\sum \mathrm{B(E1)} \uparrow = 421(5) \times 10^{-3} \mathrm{e^2 fm^2}\,, \tag{6.1}$$

corresponding to 0.57 % of the energy-weighted sum rule (EWSR) for isovector dipole excitations [108], if a branching ratio to excited states is neglected (i.e.

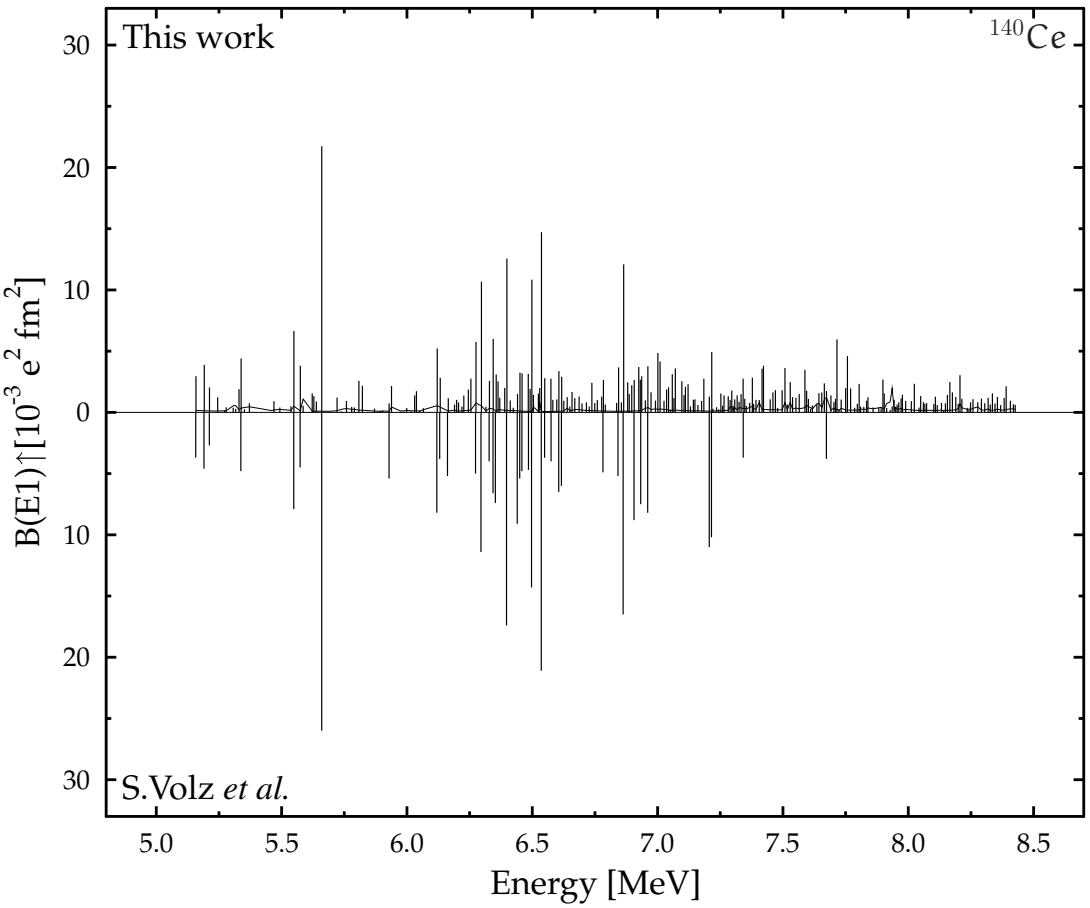

Figure 6.1: B(E1) strength determined for the dipole excited states in ^{140}Ce. The figure shows the data from this work in the upper half, and the known strengths from [63] in the lower half. The black line marks the sensitivity limit.

$\Gamma_0/\Gamma = 1$). This assumption was used for many experiments in the past, because it was not possible to directly measure the branching ratio. It is shown below that with the new γ^3 setup such measurements are now possible and have a considerable impact on the magnitude of the B(E1) transition strength. The summed B(E1) strength in the energy range from 3 MeV to 8.5 MeV can be compared to the previously measured value of $308(59) \times 10^{-3}$ e^2 fm^2 from [63]. The newly determined value includes only statistical uncertainties. Systematic errors introduced by the photon flux calibration amount to 20 % for the states above 7.5 MeV, i.e. 21×10^{-3} e^2 fm^2. Figure 6.2 compares the B(E1) strength to the values predicted by a QPM calculation [65]. The distribution of the levels is very similar, and the magnitude of the strength is also comparable. The calculation predicts a summed B(E1) strength of 797×10^{-3} e^2 fm^2, which is about 90 % more than what was measured. The amount of missing strength can be attributed to the fact that peaks below the sensitivity limit could not be taken

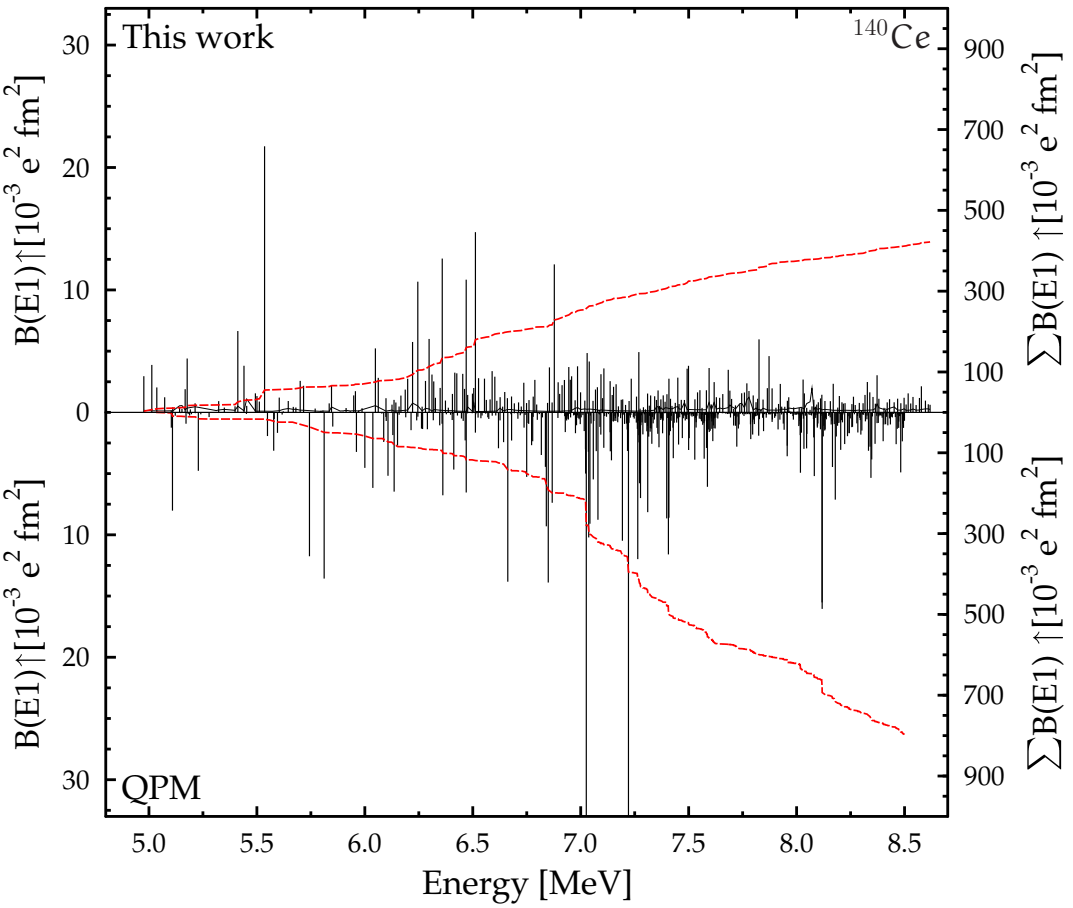

Figure 6.2: The B(E1) strength determined for the dipole excited states in ^{140}Ce shown together with the values predicted by a QPM calculation from V.Yu. Ponomarev [65]. The red lines show the accumulated strength as a function of the energy.

into account. Also the branching ratio to excited states was neglected. The accumulated strength as a function of the energy (red lines in Fig. 6.2) indicates that the strength distribution predicted by the QPM is also shifted to higher energy.

6.2 Parity measurements

Parity measurements of the investigated states can be performed with the help of the experimental asymmetry ϵ (Equ. 4.2.3) introduced in Section 4.2.3. Figure 6.3 shows the measured asymmetries for all investigated states above the sensitivity limit. The finite opening angle for the detectors has been taken into account in the asymmetry, such that a value of -0.3 ($+0.3$) indicates negative (positive) parity for the data from 2012. In 2013 the different geometry increased the experimental asymmetry to ± 0.75. Prior to this measurement only few pari-

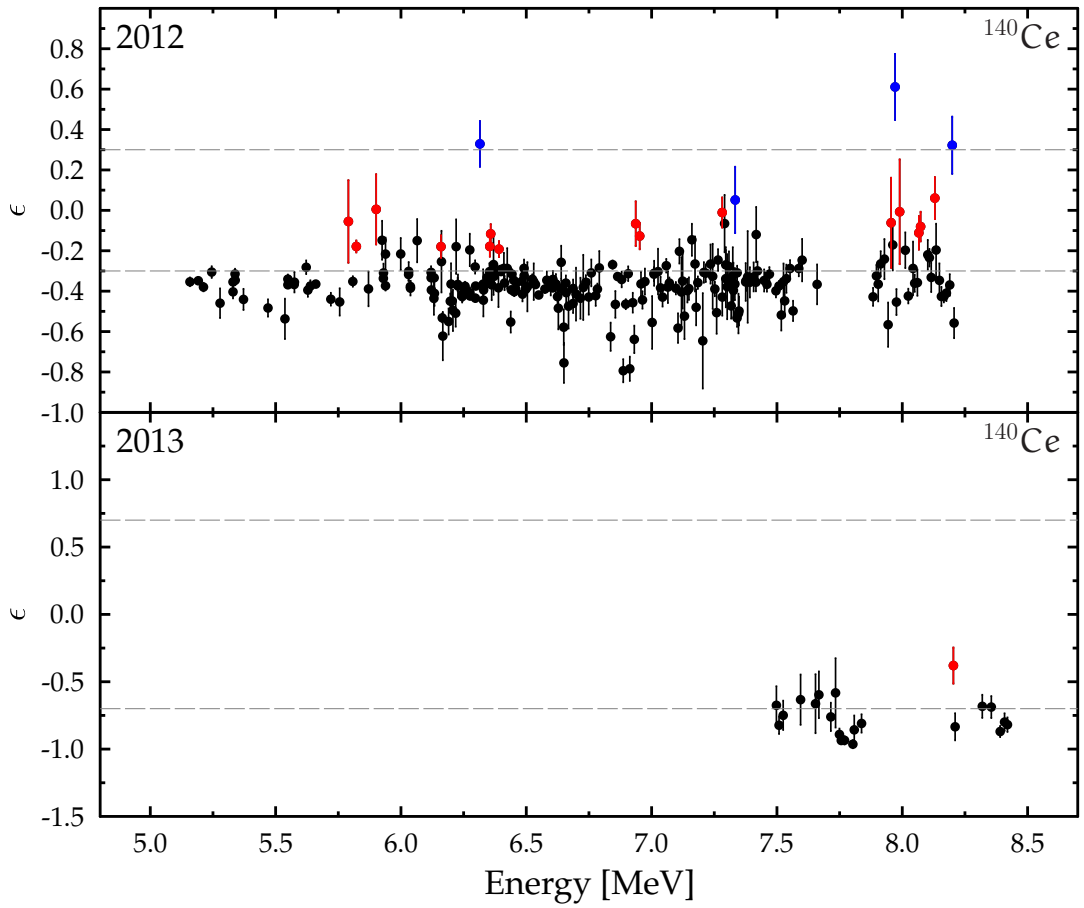

Figure 6.3: Asymmetry for investigated states in ^{140}Ce and parity assignments. Due to the difference in detector geometry different values for the asymmetry are expected for the 2012 and 2013 data. Parity assignments are indicated by the colour: E1 transitions are black, M1 transitions blue. Ambiguous results are marked in red.

ties were known from Compton-polarimetry measurements [109]. No M1 states have been identified previously. To assign a parity, the determined value for the asymmetry must be closer than 2σ to the theoretical value, as well as 2σ away from the value for the opposite parity. For most of the investigated states negative parity was assigned (black points), five states were assigned positive parity (blue), but for some states (shown in red) no unambiguous assignment was possible. This is likely due to the fact that overlapping peaks could not be resolved. This result shows that the strength located in this energy region is mostly electric dipole strength, and thus can be attributed to the Pygmy Dipole Resonance.

6.3 Branching ratios from singles data

In Figure 4.16 a simplified level scheme for ^{140}Ce is shown, emphasising the distribution of the low-energy levels, which play a role in the following discussion. Due to the narrow energy distribution of the photon beam the low-lying levels were not directly excited, but instead are populated by the inelastic decay of the states in the excitation energy range (feeding effect). The low-lying states in turn mostly decay to the 2_1^+. Therefore it is possible to derive from the population of the 2_1^+ an average branching ratio of the states in the excitation energy range to other excited states. Since no information about the populating transition (the primary decay) is available, it is impossible to determine the exact decay pattern using this method. However, contributions from the decay of all states, particularly from weakly excited states (with a small radiation width Γ_0), are included in the population of the 2_1^+. The resulting value is a good approximation for the average ground state branching ratio $\langle b_0 \rangle$. From the singles data the total strength from all transitions that populate the low-lying states up to the 2_7^+ state at 3320 keV are determined. These are shown relative to the ground state transition strength in the top part of Fig. 6.4. The decay of the 2_5^+ at an energy of 3.001 MeV was never observed in the data. Judging from [105], this state should either decay to the 2_1^+ or to the 0_2^+, but neither of these transitions has been observed. In Fig. 6.4 it can be seen, that the probability for inelastic transitions to take place increases strongly with increasing excitation energy. The strongest component is the decay of the 2_1^+, because it is the lowest excited state and other excited states decay via the 2_1^+ state. Higher excited states are populated with successively decreasing probability. This pattern is especially noticeable above an excitation energy of 6.5 MeV, indicating that below this energy either the sensitivity is too low to observe the transitions, or that structural effects have an influence on the population probabilities.

The lower part of Fig. 6.4 shows the photo-absorption cross-section determined for ^{140}Ce. The elastic cross-section $\sigma_{\gamma\gamma}$ is directly determined from the sum of the energy-integrated cross-sections at each beam energy setting. Each integrated cross-section is proportional to the peak areas A_i of the transitions to the ground state. Combining Equations 2.6, 2.7 and 2.8 yields

$$\sigma_{\gamma\gamma} = \frac{1}{N_\gamma \cdot N_T} \sum_i \frac{A_i}{\epsilon_i \cdot W_i(\theta, \varphi, \Delta\Omega)} \,. \tag{6.2}$$

The inelastic part of the cross-section as a function of the excitation energy is determined from the amount of feeding transitions to the 2_1^+ state. As discussed above the population probability the 2_1^+ is a measure for the amount of inelastic transitions in comparison to direct ground state transitions. The average

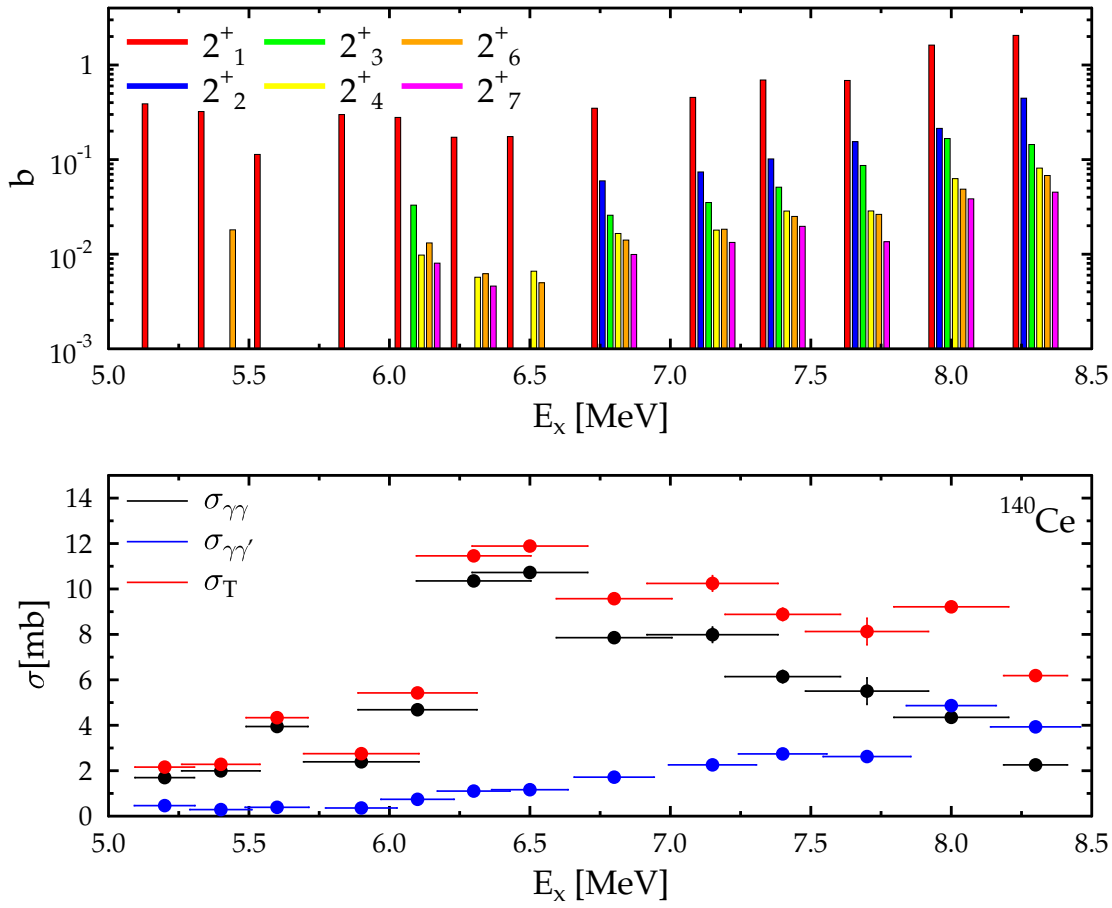

Figure 6.4: *Top:* Feeding intensity of low-lying excited states in ^{140}Ce determined from singles spectra as a function of excitation energy. The different colours indicate the different excited states. Values are shown relative to the ground state decay intensity. *Bottom:* Elastic ($\sigma_{\gamma\gamma}$), inelastic ($\sigma_{\gamma\gamma'}$), and total (σ_T) photo-absorption cross-section as a function of the energy in the PDR region in ^{140}Ce.

branching ratio of the states in the excitation energy range to other excited states is defined as:

$$\sigma_{\gamma\gamma'} = \frac{1}{N_\gamma \cdot N_T} \frac{A_{2^+_1}}{\epsilon_{2^+_1} \cdot W_i(\theta, \varphi, \Delta\Omega)} \,. \tag{6.3}$$

Since the populating state for the 2^+_1 is not known, the angular distribution is assumed to be 1 (isotropic). The total cross-section is just the sum of the elastic and the inelastic part

$$\sigma_T = \sigma_{\gamma\gamma} + \sigma_{\gamma\gamma'} \,. \tag{6.4}$$

The the centre of mass and the magnitude of the photo-absorption cross-section as well as the ratio of the inelastic to the elastic cross-section are similar to the results from other nuclei in the same region (see [30, 32, 66]).

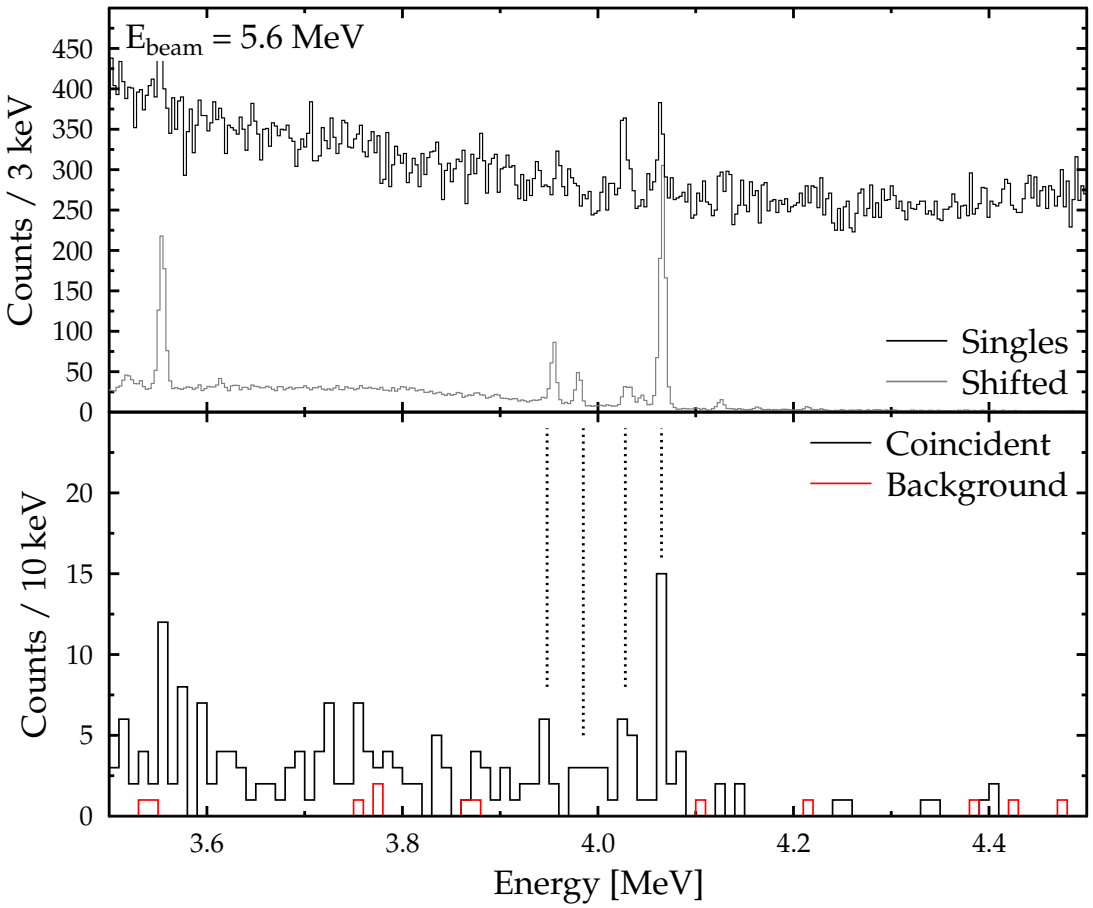

Figure 6.5: *Top:* Summed HPGe singles spectrum at a beam energy of 5.6 MeV in the region of the decays to the 2_1^+ state. The shifted grey spectrum shows the ground state transitions as a reference. *Bottom:* HPGe coincidence spectrum with an energy gate on the transition from the 2_1^+ state, selecting the primary inelastic transitions. The red spectrum shows the background obtained from an energy gate next to the peak.

6.4 Branching ratios for single states

The determination of the decay branching ratio of single $J = 1^-$ states in the PDR region with energy E_i to low-lying excited states with energy E_j is only possible using the singles data in combination with the coincidence data. The branching ratio is determined according to

$$b_{i\to j}(E_i) = \frac{A_{i\to j}}{A_{i\to 0}} \frac{\epsilon_{i\to 0}(E_i)}{\epsilon_{i\to j}(E_i - E_j) \cdot \epsilon_{j\to 0}(E_j)} \tag{6.5}$$

The summed spectra are used in the analysis, which requires that also the summed efficiency are used in ϵ. In the singles spectra the peak to background ratio is too small to allow for proper investigation of the peak area, except for

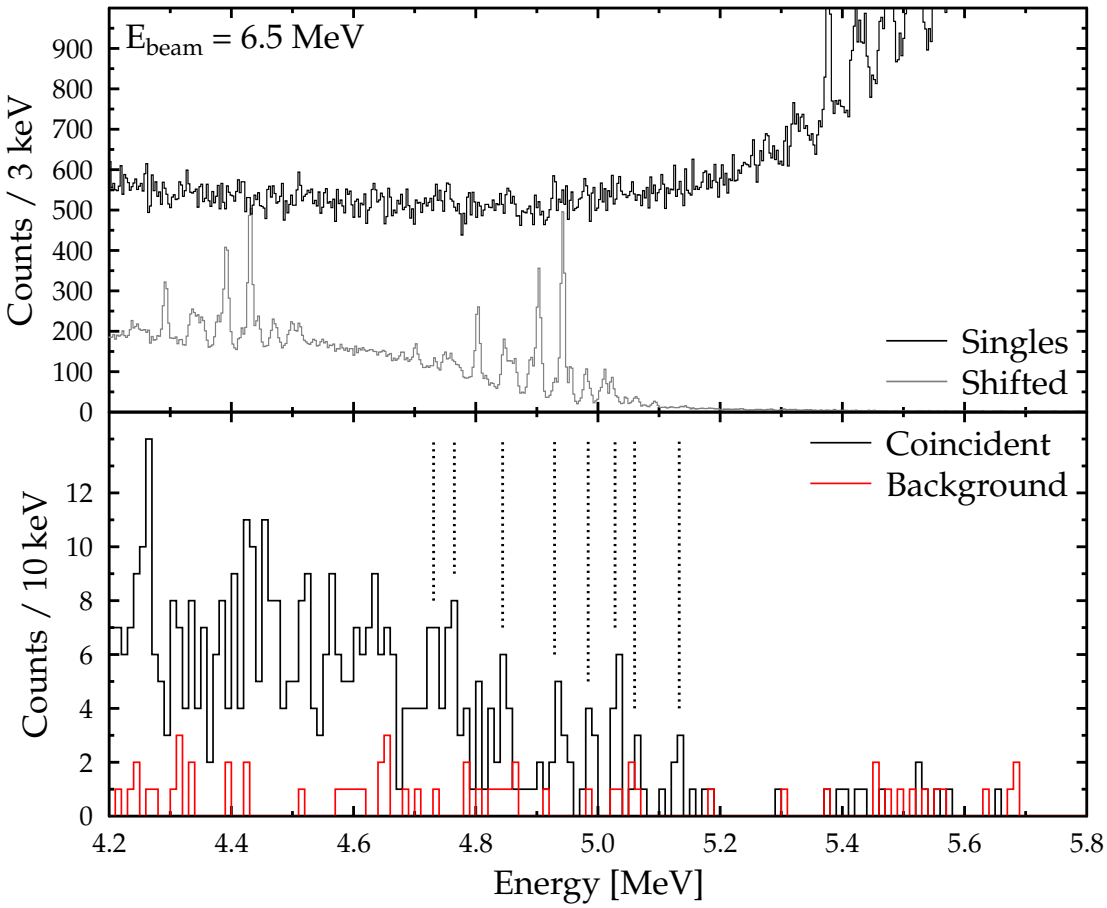

Figure 6.6: *Top:* Summed HPGe singles spectrum at a beam energy of 6.5 MeV in the region of the decays to the 2_1^+ state. The shifted grey spectrum shows the ground state transitions as a reference. *Bottom:* HPGe coincidence spectrum with an energy gate on the transition from the 2_1^+ state, selecting the primary inelastic transitions.

very few cases. The upper part of Fig. 6.5 shows a summed HPGe spectrum at 5.6 MeV beam energy in the energy range where the transitions to the first 2^+ state are expected. The grey spectrum shows the ground state transitions as a reference, shifted by the energy of the 2_1^+ transition. The presence of peaks in that region of the spectrum is clear, but the analysis of singles peaks difficult, because of the small peak to background ratio. The HPGe-LaBr coincidence matrices allow to select events corresponding to two-step decays that take place via one of the low-lying states. The lower part of Fig. 6.5 shows such an HPGe spectrum in coincidence with the detection of a photon with the energy of the first 2^+ state in one of the $LaBr_3$:Ce detectors. The comparison to the upper part shows that the number of events is drastically reduced when the coincidence condition is used, but the peak to background ratio is strongly improved, resulting in a nearly background-free spectrum. The background indicated by the red spec-

Table 6.1: Values for the branching ratio for the transition $1^+ \rightarrow 2_1^+$ in ^{140}Ce determined from singles spectra and HPGe-LaBr coincidences. Values are given relative to the intensity of the ground state transition. The errors in brackets are of pure statistical nature.

E_x [keV]	E_γ [keV]	$b_{2_1^+}$	E_x [keV]	E_γ [keV]	$b_{2_1^+}$
5537	3938	0.33(13)	6206	4606	0.05(2)
5574	3981	0.042(18)	6219	4620	0.07(2)
5622	4024	0.11(4)	6245	4646	0.030(15)
5660	4063	0.013(3)	6329	4733	0.040(13)
5721	4126	0.29(13)	6363	4764	0.020(8)
5870	4271	0.14(8)	6424	4826	0.015(13)
5902	4303	0.13(8)	6441	4844	0.013(6)
5920	4324	0.40(19)	6491	4891	0.023(15)
5999	4395	0.04(3)	6524	4921	0.042(14)
6016	4413	0.09(8)	6574	4977	0.014(7)
6038	4443	0.019(14)	6617	5023	0.026(10)
6133	4534	0.031(10)	6716	5122	0.6(4)
6165	4565	0.028(14)			

trum is obtained by selecting an energy gate 2σ above the peak from the decay of the 2_1^+. The coincidence spectrum allows to directly determine the branching ratios for single states, even with the available limited statistics in the spectra. For the given example the analysis of the largest peak at 4.06 MeV (corresponding to a ground state transition of 5.660 MeV) via Equ. (6.4) yields a branching ratio of 1.3(3) %. This proves the excellent sensitivity of the method. However, even with this highly improved sensitivity, only for a few $J = 1^-$ states a transition to the 2_1^+ state was observed, i.e. for most strongly excited states this decay branch must be very small. These are marked with dotted lines in Figs. 6.5 and 6.6. Figure 6.6 shows the same spectra for the higher excitation energy range of 6.5 MeV. Here the background contribution in the coincidence spectrum is slightly more pronounced, and the level density is higher. This makes the assignment of the corresponding peaks in the two spectra more difficult. At higher energy a one-to-one assignment is not possible for single states. Figure 6.6 also shows examples for transitions that decay only weakly to the ground state, but instead rather strongly to the 2_1^+ (see e.g. at 5.122 MeV). In Table 6.1 the transitions with the determined branching ratios are listed. The smallest branching ratio was measured for the already mentioned state with the ground state transition of 5.660 MeV. For a few states that decay weakly to the ground state, such as the the one at an excitation energy of 5.537 MeV, the branching to the excited state is substantially higher.

6.5 Averaged branching ratios

While the observation of the $2_1^+ \rightarrow 0_1^+$ transition provides a good approximation of the average ground state branching b (see Section 6.3), the clear advantage of the coincidence data is the definite identification of the decay path from a primary excited state, via an intermediate low-lying state, back to the ground state. The singles data do not contain this complete information, and the branching ratio determined from singles data additionally contains the strength of all possible transitions that populate the 2_1^+ state. Therefore, the branching ratios determined using singles data are enhanced. The drawback of using the coincidence method is the strongly reduced amount of statistics, due to the fact that two photons have to be detected in different detectors. However, the LaBr-LaBr coincidences are best suited to determine the average branching ratios. The superior energy resolution of the HPGe detectors is sacrificed in favour of improved detection efficiency provided by the $LaBr_3$:Ce detectors. The average branching ratios are determined from unfolded singles and coincidence spectra. The two unfolding methods discussed in Sec. 4.1.1 have been applied to the measured spectra according to the procedure described in Sec. 4.3.1 in order to allow proper integration of the full-energy peak range. In Figs. 6.7 and 6.8 the projected spectra obtained from the LaBr-LaBr coincidence matrices are shown after unfolding for four different excitation energies (5.2 MeV,6.5 MeV,7.15 MeV, and 8.3 MeV). The decay of the 2_1^+ state is selected with the energy gate. The top row shows the result after unfolding with the Top-Down method, while the bottom row shows the result after application of the Gold unfolding method. In addition, the top row displays the original spectra in grey colour. The energy range corresponding to the energies of primary decays is marked with the red dashed line. This range has the same width as the excitation energy region, shifted towards lower energy by the energy of the 2_1^+ state. In the progression from low to high excitation energy the low-energy contributions in the unfolded spectra increase as well. The black arrows indicate energies corresponding to primary transitions in coincidence with the low-lying excited states (such as 2^+1, 0_2^+, 2_2^+, 2_3^+,...). The low-energy contributions in the unfolded spectra can be attributed to some of these coincidences. As seen above in the singles spectra (see Fig. 6.4) the branching ratio to higher excited states increases strongly with increasing excitation energy. The same pattern is now also visible in the coincidences.

From these unfolded coincidence spectra the averaged branching ratio to the first two excited 2^+ states is determined. In this case no enhancement is present, because the coincidence condition does not allow any other decay channels, besides the selected two-step cascade. As discussed in Sec. 4.2.1, the angular distribution of the primary decay allows in principle to distinguish between the transitions $(1^- \rightarrow 0_2^+)$ and $(1^- \rightarrow 2_1^+)$ which are very close in energy (307 keV),

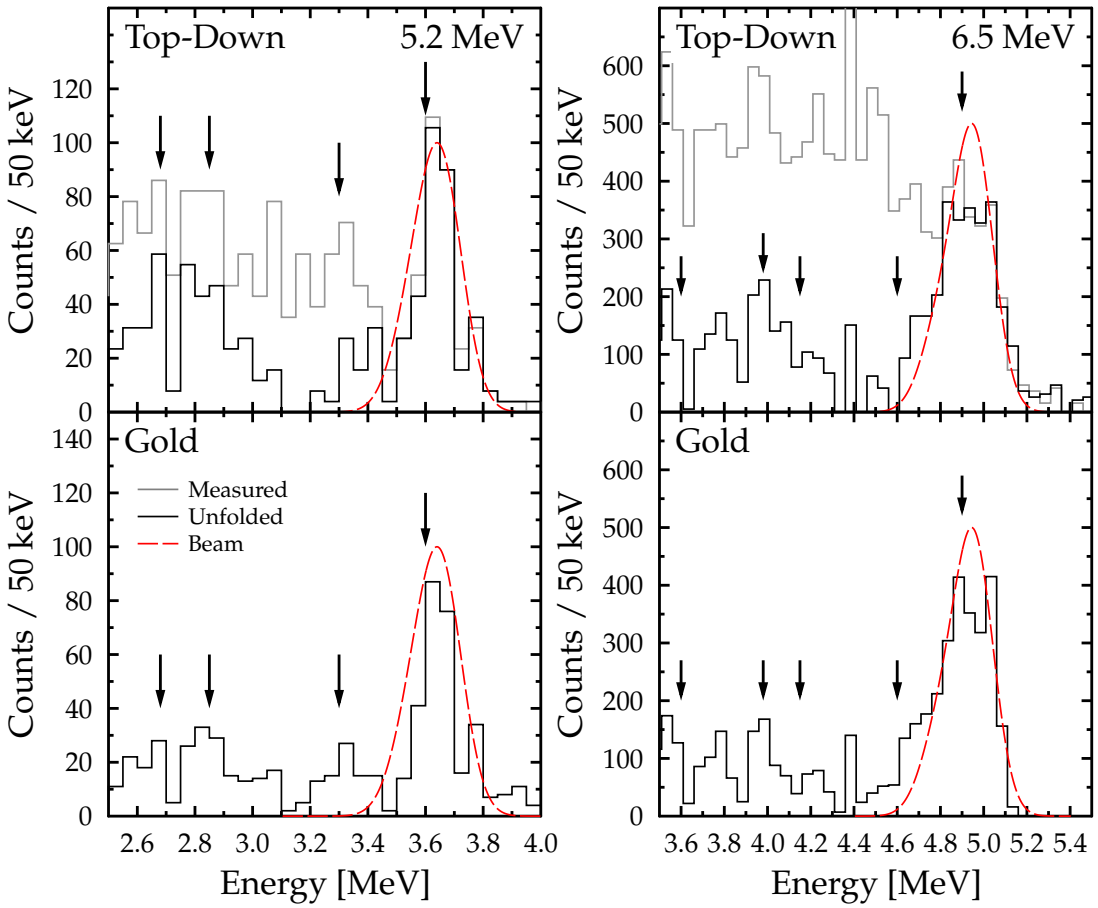

Figure 6.7: Unfolded energy gated spectra for the beam energies 5.2 MeV and 6.5 MeV. Black arrows indicate energies corresponding to transitions to excited states. *Top:* Measured spectrum (grey) shown together with unfolded spectrum using the Top-Down method (black) and the beam shape (red,dashed). *Bottom:* Same spectrum, but unfolded using the Gold method.

but due to the low amount of statistics no significant difference was found. Therefore a possible admixture of the $(1^- \rightarrow 0_2^+)$ transition might be present in the results shown in Figs. 6.9 and 6.10. The data in Fig. 6.9 is obtained from Top-Down unfolded spectra, while the data in Fig. 6.10 is obtained from Gold unfolded spectra. The solid line represents results for the branching ratio to the 2_1^+ state from a QPM calculation [65] taking into account coupling to complex configurations of up to three phonons. As already observed in Sec. 6.1, the QPM calculation results are shifted to higher energy. The results after Gold unfolding are systematically lower by about 10 % in comparison to the Top-Down unfolded results, but show the same pattern.

Comparison of the experimental findings to the QPM calculation (indicated in the figure as a solid line) shows a good agreement over the whole energy range

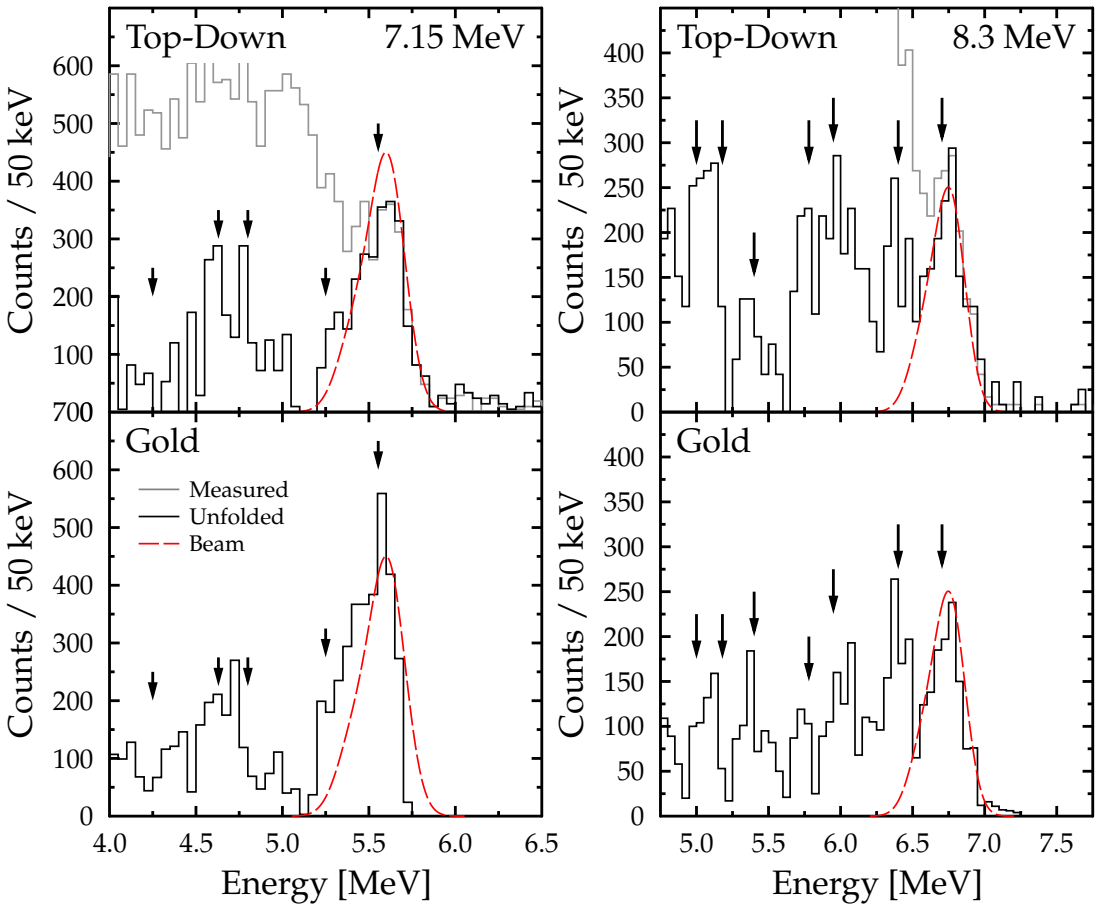

Figure 6.8: Unfolded energy gated spectra for the beam energies 7.15 MeV and 8.3 MeV. Black arrows indicate energies corresponding to transitions to excited states. *Top:* Measured spectrum (grey) shown together with unfolded spectrum using the Top-Down method (black) and the beam shape (red,dashed). *Bottom:* Same spectrum, but unfolded using the Gold method.

of the PDR. This is a clear indication that the coupling to complex configurations in the QPM leads not only to an adequate description of the strength fragmentation, but in addition describes the transition probabilities to excited states with high accuracy.

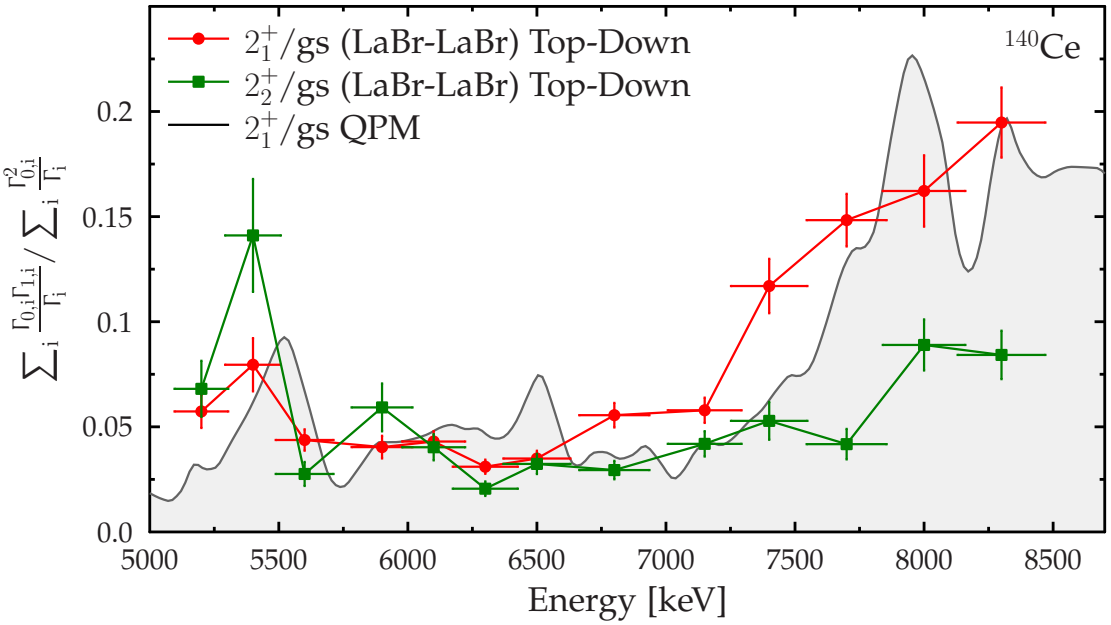

Figure 6.9: Averaged branching ratios to the first excited states in ^{140}Ce obtained after unfolding with the Top-Down method. Values from the QPM calculation were folded with a Lorentzian distribution of 300 keV width. The resulting distribution is shown as a solid line.

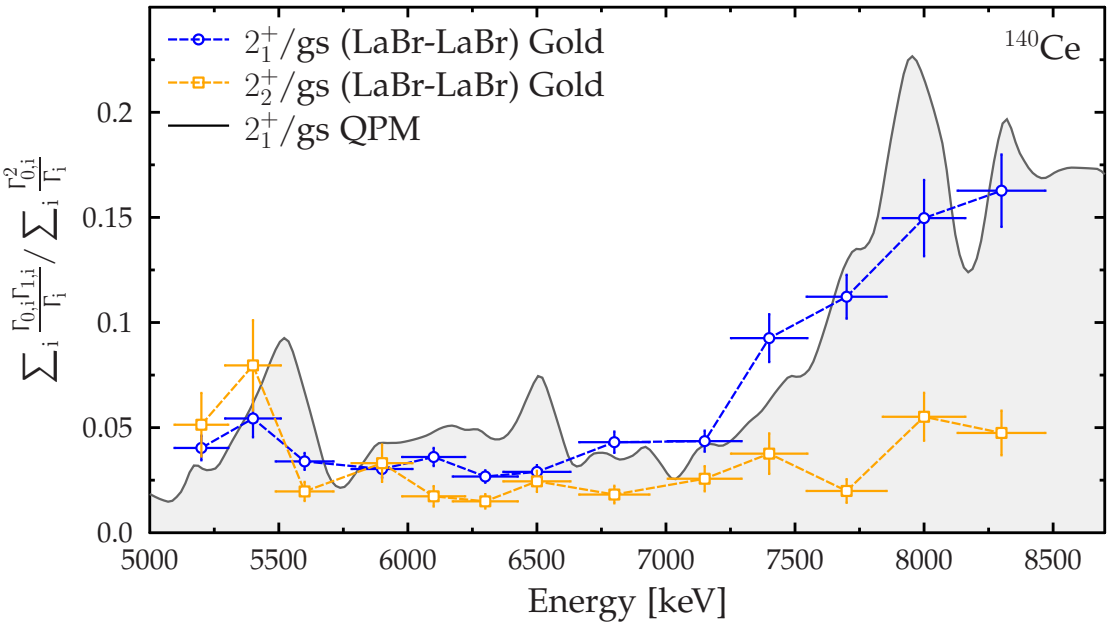

Figure 6.10: Averaged branching ratios to the first excited states in ^{140}Ce obtained after unfolding with the Gold method. Values from the QPM calculation were folded with a Lorentzian distribution of 300 keV width. The resulting distribution is shown as a solid line.

Chapter 7

Summary and Outlook

Within the scope of this thesis two main points have been addressed: A new experimental setup, the γ^3 setup, was installed at the HIγS facility, that permits for the first time the study of NRF reactions with γ-γ-coincidence decay spectroscopy. Using this new setup, the decay pattern of the Pygmy Dipole Resonance was investigated for the first time in the nucleus ^{140}Ce using the $(\gamma, \gamma'\gamma'')$ coincidence method.

The new experimental setup consists of high-resolution high-purity Germanium detectors and highly efficient $LaBr_3$:Ce scintillation detectors. In combination with the linearly polarised quasi-monochromatic photon beam, which allows for the highly selective excitation of $J = 1$ states in a narrow energy band, it is possible to significantly increase the experimental sensitivity for weak transitions. Compared to earlier experiments with pure singles readout, a new domain of observables is now accessible in the NRF reaction: The direct and non-ambiguous measurement of two-step γ-cascades from the decay of $J = 1$ states is possible with this new installation. The decay pattern of dipole excited states below the particle separation threshold can be measured in a model-independent way and with high precision. The experimental data shows, that the new setup is sensitive enough to measure branching ratios to excited states of only a few percent for discrete transitions, and with a sensitivity better than 1 % for average branching ratios.

Two experimental campaigns in 2012 and 2013 have successfully used the γ^3 setup to investigate the dipole response of neutron-rich nuclei in the medium and heavy mass region. Of particular interest was the decay pattern of the states participating in the Pygmy Dipole Resonance, the fragmentation of the M1 scissors mode, and the structure of the 2-phonon state. In the commissioning phase for the experimental setup the nucleus ^{32}S was investigated to test the experiment, measure important properties, such as the detector efficiency, and to investigate the best practices for suppressing background radiation.

The nucleus ^{140}Ce was investigated as part of the experimental campaigns. The main focus was the study of the decay pattern of the dipole excited states, to measure parities and the total B(E1) strength with higher accuracy, and to extend the energy range. The high intensity of the photon beam paired with the relatively long measurement time of 8 h per beam energy setting allowed to increase the sensitivity for weak ground state transitions.

The analysis of singles spectra allowed to determine the population probabilities of low-lying excited states from the excitation energy range. From these values a good approximation of the total photo-absorption cross-section of ^{140}Ce was possible. The branching ratios of the states in the PDR region to the first excited 2^+ states were determined in a direct and model-independent way from coincidence data. Comparison of the results to QPM calculations show a striking similarity over the whole energy range of the PDR. This is a clear indication that the coupling to complex configurations in the QPM leads not only to an adequate description of the strength fragmentation, but in addition describes the transition probabilities to excited states with high accuracy. This is especially important for a nucleus such as ^{140}Ce in the transition region, where neither methods based purely on single-particle excitations nor purely statistical methods provide an accurate description. The similarity in the increase of the branching ratio to either of the low-lying excited states as a function of the energy of the emitted photon might be an indication for the validity of the Brink-Axel hypothesis. At excitation energies above 6 MeV the increase in the level density leads to a transition region, where a description of the decay pattern in the context of the statistical model might be applicable.

7.1 Future experiments

So far a number of different nuclei, – light and heavy, spherical as well as deformed – have been investigated at the γ^3 setup, but data analysis has not yet caught up with all of them. Especially the investigation of ^{128}Te will be of interest, which is an ideal candidate to be treated within the context of the statistical model, because of the high level density.

The γ^3 setup an the HIγS facility is an ideal location for future measurement campaigns. The investigation of stable nuclei with γ-γ-coincidence measurements has proven to be feasible and should be extended in a systematical way to many more isotopes. Especially experiments that have been performed in the past either with poor statistics or under inadequate experimental conditions should be repeated. Also complementary measurements of nuclei previously investigated only with other probes will yield new information. The Sn isotopic chain in combination with the Mo or Zr chain are ideal candidates to study the evolution of the decay behaviour of the dipole excited states across a large part of the nuclear chart.

The planned future facility for anti-proton and ion research (FAIR) in Darmstadt as well as the extreme light infrastructure for nuclear physics (ELI-NP) in Bucharest will provide interesting new experimental conditions for the study of stable and exotic isotopes. At FAIR [110] higher energies and new production mechanisms will push back the driplines and allow the investigation of highly-exotic radioactive ion beams in inverse kinematics. The LCB photon source at ELI-NP [111] increases the instantaneous photon flux available at the target to new dimensions, and in combination with the next generation of the γ^3 detector setup will allow the investigation of stable targets in greater detail than it is possible today.

Appendix A

Experimental data

A.1 Levels of ^{140}Ce

Table A.1: Results from the analysis of the ^{140}Ce singles data. Listed are the energy of the emitted photon E_γ, the assigned spin and parity J^π, the determined branching product of ground state transition width and branching ratio to the ground state Γ_0^2/Γ, as well as the reduced transition strengths B(E1)↑ for an electric dipole transition or B(M1)↑ for a magnetic dipole transition.

E_γ [keV]	J^π	Γ_0^2/Γ [meV]	B(E1)↑ [$10^{-3}e^2fm^2$]	B(M1)↑ [μ_N^2]
5158.25[a]	1^-	142(9)	3.0(2)	–
5191.43[a]	1^-	189(8)	3.9(2)	–
5212.19[a]	1^-	101(6)	2.04(12)	–
5244.92	1	62(5)	1.23(10)	0.110(9)
5278.6	1	21(4)	0.41(8)	0.040(8)
5330.02[a]	1^-	101(9)	1.9(2)	–
5338.43[a]	1^-	222(13)	4.4(3)	–
5371.35[a]	1^-	45(7)	0.7(2)	–
5469.4	1	52(6)	0.92(11)	0.080(10)
5492.9	1^-	23(5)	0.40(9)	–
5537.4	1^-	33(8)	0.50(14)	–
5548.95[a]	1^-	454(16)	6.6(4)	–
5574.59[a]	1^-	220(11)	3.8(2)	–
5621.99	1	96(9)	1.55(14)	0.140(12)
5628.52	1	83(8)	1.33(12)	0.120(11)
5638.46[a]	1	55(6)	0.88(9)	0.080(8)
5660.17[a]	1^-	1375(20)	21.7(3)	–
5721.19	1^-	77(7)	1.21(11)	–
5758.65	1	34(8)	0.9(3)	0.08(3)
5779.5	1^-	30(15)	0.5(2)	–

Table A.1 – Results from ^{140}Ce *continued*

E_γ [keV]	J^π	Γ_0^2/Γ [meV]	B(E1)↑ [$10^{-3}e^2fm^2$]	B(M1)↑ [μ_N^2]
5808.26[a]	1	176(14)	2.6(2)	0.23(2)
5822.29[a]	1	149(13)	2.2(2)	0.20(2)
5870.51	1^-	22(5)	0.31(7)	–
5894.4	1^-	10(4)	0.14(5)	–
5902.75	1^+	11(5)	–	0.010(6)
5928.81[a]	1	172(15)	0.7(2)	0.07(2)
5938.42[a]	1^-	104(7)	2.2(5)	–
5999.04	1^-	21(5)	0.4(2)	–
6030.71	1^-	113(9)	1.39(12)	–
6037.8[a]	1^-	144(11)	1.73(14)	–
6065.35	1^-	20(6)	0.34(10)	–
6120.81[a]	1^-	505(15)	5.2(4)	–
6132.78[a]	1^+	258(12)	–	0.26(6)
6164.86	1^-	174(15)	1.2(2)	–
6189.9	1^-	41(7)	0.6(3)	–
6198.33[a]	1^-	85(9)	1.02(11)	–
6205.95[a]	1^-	69(9)	0.81(11)	–
6219.3	1^-	42(8)	0.48(9)	–
6226.89[a]	1^-	119(11)	1.37(13)	–
6244.9	1^-	160(13)	1.9(2)	–
6255.04[a]	1^-	252(16)	2.8(2)	–
6275.37[a]	1^-	314(16)	5.8(13)	–
6297.16[a]	1	803(21)	10.7(10)	0.97(9)
6315.09	1^-	41(12)	0.47(13)	–
6329.07[a]	1^-	213(12)	2.6(5)	–
6344.06[a]	1^-	475(17)	6.0(5)	–
6356.01	1	300(38)	3.1(4)	0.28(4)
6363.39	1^-	207(17)	2.5(5)	–
6370.28	1^-	109(14)	1.2(5)	–
6390.05	1	203(24)	2.0(7)	0.18(6)
6398.74[a]	1	1235(34)	12.6(7)	1.14(7)
6412.03	1^-	108(12)	1.0(2)	–
6424	1^-	35(10)	0.38(11)	–
6441.11[a]	1^-	415(22)	1.5(3)	–
6450.91[a]	1^-	315(19)	3.2(2)	–
6459.25[a]	1^-	309(18)	3.2(2)	–
6483.95	1^-	295(19)	3.1(2)	–
6491.25	1^-	191(22)	1.9(2)	–
6498.3[a]	1^-	1033(29)	10.8(3)	–

Table A.1 – Results from ^{140}Ce *continued*

E_γ [keV]	J^π	Γ_0^2/Γ [meV]	B(E1)↑ [$10^{-3}e^2fm^2$]	B(M1)↑ [μ_N^2]
6504.4	1^-	137(57)	1.4(6)	–
6524.33	1^-	148(10)	1.53(11)	–
6529.7	1^-	194(50)	2.0(5)	–
6536.65[a]	1^-	1434(23)	14.7(2)	–
6549.69	1^-	274(12)	2.79(12)	–
6574.33[a]	1^-	273(14)	2.76(15)	–
6581.91[a]	1^-	101(12)	1.02(12)	–
6597.64[a]	1	109(12)	1.06(12)	0.100(11)
6606.08[a]	1	348(16)	3.4(2)	0.300(15)
6617.32[a]	1	301(16)	2.9(2)	0.260(14)
6625.7	1	98(12)	0.95(12)	0.090(11)
6639.33	1	102(12)	1.2(5)	0.11(5)
6649.85	1^-	59(14)	0.47(13)	–
6658.53[a]	1^-	190(19)	1.7(2)	–
6669.55	1^-	49(13)	1.2(4)	–
6686.77	1^-	168(19)	1.3(2)	–
6698.4	1^-	77(28)	0.7(3)	–
6716	1^-	86(24)	0.8(2)	–
6727.3	1^-	51(23)	0.5(2)	–
6737.73	1^-	258(26)	2.4(2)	–
6749.2	1^-	82(20)	0.8(2)	–
6759.4	1^-	108(20)	1.0(2)	–
6776.94	1^-	140(21)	1.3(2)	–
6783.74	1^-	289(23)	2.6(2)	–
6791.3	1^-	70(17)	0.6(2)	–
6836.5	1^-	86(17)	0.8(2)	–
6844.32	1	411(24)	3.7(2)	0.33(2)
6855.4	1^-	91(16)	0.81(15)	–
6864.58[a]	1	1364(32)	12.1(3)	1.09(3)
6880.58	1^-	280(28)	2.5(2)	–
6886.8	1^-	172(21)	1.5(2)	–
6896.83[a]	1^-	254(18)	2.2(2)	–
6906.63[a]	1^-	304(29)	2.6(3)	–
6924.8[a]	1^-	429(48)	3.7(4)	–
6930.9	1^-	309(63)	2.7(5)	–
6936.5	1	343(105)	3.0(9)	0.27(8)
6951.09	1	178(38)	1.0(5)	0.09(4)
6961.14	1^-	206(21)	3.8(6)	–
6973.75[a]	1^-	169(33)	1.6(3)	–

Table A.1 – Results from ^{140}Ce *continued*

E_γ [keV]	J^π	Γ_0^2/Γ [meV]	B(E1)↑ [$10^{-3}e^2fm^2$]	B(M1)↑ [μ_N^2]
6985.15	1	64(22)	1.0(4)	0.09(3)
7001.05	1^-	327(40)	4.8(4)	–
7009.8[a]	1^-	410(49)	4.2(4)	–
7025.5	1^-	114(37)	0.9(3)	–
7035.76	1^-	227(36)	1.9(3)	–
7043.66	1^-	251(34)	2.1(3)	–
7058.55[a]	1	383(37)	3.1(3)	0.28(3)
7065	1^-	143(32)	1.2(3)	–
7070.69[a]	1^-	443(34)	3.6(3)	–
7096.64[a]	1^-	318(28)	2.5(2)	–
7105.3	1^-	178(44)	1.4(4)	–
7110.9	1	262(46)	2.1(4)	0.19(3)
7131.1	1	62(21)	0.5(2)	0.040(15)
7142.8	1^-	131(21)	1.0(2)	–
7148.9	1^-	135(21)	1.1(2)	–
7160.73	1^-	78(17)	0.61(14)	–
7175.4	1^-	145(35)	0.9(3)	–
7184.42[a]	1^-	356(33)	2.8(3)	–
7215.96[a]	1^-	646(72)	4.9(6)	–
7235.1	1^-	55(15)	0.42(12)	–
7243.6	1^-	33(15)	0.25(12)	–
7252.32	1^-	205(21)	1.5(2)	–
7259.4	1^-	73(21)	0.6(2)	–
7265.01[a]	1^-	185(28)	1.4(2)	–
7281.74	1^-	194(35)	1.3(3)	–
7289.25	1^-	116(42)	1.0(4)	–
7295.9	1^-	124(34)	1.8(4)	–
7301.5	1^-	72(33)	0.5(2)	–
7307.6	1^-	120(24)	1.1(3)	–
7317.38	1^-	209(25)	1.4(2)	–
7325.05	1^-	87(33)	0.9(3)	–
7332.8	1^+	146(41)	–	0.13(3)
7341.07[a]	1^-	394(42)	2.8(3)	–
7347.55	1^-	147(32)	1.1(3)	–
7353.7	1^-	73(32)	0.5(2)	–
7367.4	1^-	109(44)	0.8(3)	–
7377.93	1^-	333(76)	2.8(7)	–
7392.45	1^-	129(31)	1.0(2)	–
7405.45	1^-	144(30)	1.0(4)	–

Table A.1 – Results from ^{140}Ce *continued*

E_γ [keV]	J^π	Γ_0^2/Γ [meV]	B(E1)↑ [$10^{-3}e^2fm^2$]	B(M1)↑ [μ_N^2]
7416.71	1^-	493(75)	3.6(5)	–
7422.35	1^-	543(79)	3.8(6)	–
7449.1	1^-	154(25)	1.1(2)	–
7460.03	1^-	237(26)	1.6(2)	–
7469.85	1^-	264(28)	1.8(2)	–
7478.8	1^-	53(20)	0.37(14)	–
7496.82[a]	1^-	266(26)	1.8(2)	–
7508.07	1^-	429(33)	3.6(12)	–
7517.4	1^-	96(25)	0.6(2)	–
7538.3	1^-	156(42)	1.2(3)	–
7551.9[a]	1^-	252(34)	1.2(3)	–
7564.9[a]	1^-	192(33)	1.5(2)	–
7587.64[a]	1^-	442(57)	3.5(4)	–
7601.55	1^-	110(36)	1.1(3)	–
7617.7	1^-	118(36)	0.6(2)	–
7643.5	1^-	195(38)	1.6(4)	–
7665.01[a]	1^-	357(61)	2.4(6)	–
7673.76	1^-	206(36)	1.7(6)	–
7691.4	1^-	217(28)	1.4(2)	–
7709.7	1^-	178(74)	1.1(5)	–
7715.53[a]	1^-	956(192)	6.0(12)	–
7732.3	1^-	169(69)	1.1(4)	–
7750.17	1^-	321(84)	2.0(5)	–
7757.25	1^-	748(88)	4.6(5)	–
7769.93	1^-	321(42)	2.0(3)	–
7785.9	1^-	63(22)	0.38(13)	–
7796.7	1^-	114(48)	0.7(3)	–
7804	1^-	385(108)	2.3(7)	–
7822.6	1^-	77(37)	0.5(2)	–
7833.5	1^-	159(73)	0.9(4)	–
7859.6	1^-	69(25)	0.41(15)	–
7898.81	1^-	126(26)	2.7(4)	–
7904	1^-	267(64)	1.6(4)	–
7943.5	1^-	181(58)	1.0(3)	–
7962	1^-	146(52)	0.8(3)	–
7971.3	1^+	202(73)	–	0.10(4)
7976.7	1^-	255(47)	1.4(3)	–
8012.1	1^-	165(41)	0.9(2)	–
8024.08	1^-	421(43)	2.3(2)	–

Table A.1 – Results from ^{140}Ce *continued*

E_γ [keV]	J^π	Γ_0^2/Γ [meV]	B(E1)↑ [$10^{-3}e^2fm^2$]	B(M1)↑ [μ_N^2]
8042.9	1^-	71(27)	0.39(15)	–
8049.5	1^-	243(30)	1.3(2)	–
8060.3	1^-	151(29)	0.8(2)	–
8066.1	1	131(30)	0.7(2)	0.06(2)
8073.13	1	138(28)	0.8(2)	0.070(14)
8101.72	1^-	126(26)	0.68(14)	–
8108.15	1	238(30)	1.3(2)	0.120(14)
8115.48	1^-	112(23)	0.60(13)	–
8132.45	1	109(32)	0.8(2)	0.07(2)
8148.1	1^-	141(33)	0.8(2)	–
8156.1	1^-	270(35)	1.4(2)	–
8165.88	1^-	471(38)	2.5(2)	–
8175.99	1^-	312(35)	1.6(2)	–
8189.4	1^-	242(36)	1.3(2)	–
8199.18	1^+	164(67)	–	0.06(3)
8206.26	1	262(50)	3.0(9)	0.27(9)
8213.78	1^-	142(39)	1.1(4)	–
8235.15	1^-	80(29)	0.4(2)	–
8248.45	1^-	144(40)	0.8(2)	–
8258.17	1^-	215(42)	1.1(2)	–
8277.26	1^-	170(48)	0.8(2)	–
8291.76	1^-	205(35)	1.1(2)	–
8305.07	1^-	149(31)	0.8(2)	–
8318.6	1^-	240(70)	1.2(3)	–
8327	1^-	130(32)	0.7(2)	–
8335.56	1^-	314(37)	1.6(2)	–
8346.1	1^-	148(46)	0.7(2)	–
8355.6	1^-	257(64)	1.3(3)	–
8368.57	1^-	123(27)	0.60(13)	–
8382.48	1^-	242(49)	1.2(2)	–
8390.49	1^-	439(67)	2.1(3)	–
8407.3	1^-	199(54)	1.0(3)	–
8419.2	1^-	138(58)	0.7(3)	–
8426.6	1^-	129(35)	0.6(2)	–

[a]Used for normalisation

A.2 Angular distributions

Tables A.2 and A.3 show the calculated values for the angular distribution coefficients $W(J^\pi, \theta, \varphi)$ for all detector combinations that are important for the analysis of the HPGe-LaBr and LaBr-LaBr coincidence data from the 2012 and 2013 beam times. Values are calculated using Equ. 2.19.

Table A.2: Angular correlations encountered in the γ^3 setup for the excitation of a $J^\pi = 1^\pm$ state and the subsequent decay through a 2^+ state. The values are given for all combinations of detectors encountered in the 2012 setup. The finite detector size has been taken into account for detector distances of $d = 6$ cm, $d = 10$ cm, and $d = \infty$ (point detector). The detector radius is 4 cm in all cases.

Setup	Det 1	Det 2	$W(J_1^\pi = 1^+)$			$W(J_1^\pi = 1^-)$		
	(θ_1, φ_1)	(θ_2, φ_2)	∞	10 cm	6 cm	∞	10 cm	6 cm
2012	LaBr1	LaBr2	1.158	1.152	1.136	1.158	1.152	1.136
		LaBr3	1.158	1.088	1.033	1.158	1.088	1.033
		LaBr4	1.158	1.152	1.136	1.158	1.152	1.136
	LaBr2	LaBr1	1.158	1.152	1.136	1.158	1.152	1.136
		LaBr3	1.158	1.152	1.136	1.158	1.152	1.136
		LaBr4	1.158	1.088	1.033	1.158	1.088	1.033
	LaBr3	LaBr1	1.158	1.088	1.033	1.158	1.088	1.033
		LaBr2	1.158	1.152	1.136	1.158	1.152	1.136
		LaBr4	1.158	1.152	1.136	1.158	1.152	1.136
	LaBr4	LaBr1	1.158	1.152	1.136	1.158	1.152	1.136
		LaBr2	1.158	1.088	1.033	1.158	1.088	1.033
		LaBr3	1.158	1.152	1.136	1.158	1.152	1.136
	HPGe1	LaBr1	1.342	1.248	1.161	0.867	0.967	1.045
		LaBr2	1.342	1.248	1.161	0.867	0.967	1.045
		LaBr3	1.342	1.248	1.161	0.867	0.967	1.045
		LaBr4	1.342	1.248	1.161	0.867	0.967	1.045
	HPGe2	LaBr1	0.867	0.967	1.045	1.342	1.248	1.161
		LaBr2	0.867	0.967	1.045	1.342	1.248	1.161
		LaBr3	0.867	0.967	1.045	1.342	1.248	1.161
		LaBr4	0.867	0.967	1.045	1.342	1.248	1.161
	HPGe3	LaBr1	1.342	1.248	1.161	0.867	0.967	1.045
		LaBr2	1.342	1.248	1.161	0.867	0.967	1.045
		LaBr3	1.342	1.248	1.161	0.867	0.967	1.045
		LaBr4	1.342	1.248	1.161	0.867	0.967	1.045
	HPGe4	LaBr1	0.867	0.967	1.045	1.342	1.248	1.161
		LaBr2	0.867	0.967	1.045	1.342	1.248	1.161
		LaBr3	0.867	0.967	1.045	1.342	1.248	1.161
		LaBr4	0.867	0.967	1.045	1.342	1.248	1.161

Table A.3: Angular correlations encountered in the γ^3 setup for the excitation of a $J^\pi = 1^\pm$ state and the subsequent decay through a 2^+ state. The values are given for all combinations of detectors encountered in the 2013 setup. The finite detector size has been taken into account for detector distances of $d = 6$ cm, $d = 10$ cm, and $d = \infty$ (point detector). The detector radius is 4 cm in all cases.

Setup	Det 1	Det 2	$W(J_1^\pi = 1^+)$			$W(J_1^\pi = 1^-)$		
	(θ_1, φ_1)	(θ_2, φ_2)	∞	10 cm	6 cm	∞	10 cm	6 cm
2013	LaBr1	LaBr2	0.881	0.925	0.964	1.113	1.056	1.009
		LaBr3	0.881	0.890	0.902	1.391	1.386	1.359
		LaBr4	1.469	1.470	1.442	0.835	0.839	0.850
	LaBr2	LaBr1	0.881	0.925	0.964	1.113	1.056	1.009
		LaBr3	0.881	0.890	0.902	1.391	1.386	1.359
		LaBr4	1.469	1.470	1.442	0.835	0.839	0.850
	LaBr3	LaBr1	1.003	1.039	1.008	0.628	0.762	0.879
		LaBr2	1.003	1.039	1.008	0.628	0.762	0.879
		LaBr4	1.003	1.202	1.288	1.255	1.094	0.965
	LaBr4	LaBr1	0.502	0.762	0.879	1.075	1.039	1.008
		LaBr2	0.502	0.762	0.879	1.075	1.039	1.008
		LaBr3	1.003	1.094	0.965	1.075	1.202	1.288
	HPGe1	LaBr1	1.003	1.039	1.008	0.628	0.762	0.879
		LaBr2	1.003	1.039	1.008	0.628	0.762	0.879
		LaBr3	0.000	0.308	0.590	2.510	2.029	1.604
		LaBr4	1.003	1.202	1.288	1.255	1.094	0.965
	HPGe2	LaBr1	0.502	0.762	0.879	1.075	1.039	1.008
		LaBr2	0.502	0.762	0.879	1.075	1.039	1.008
		LaBr3	1.003	1.094	0.965	1.075	1.202	1.288
		LaBr4	2.006	1.767	1.427	0.000	0.268	0.525
	HPGe3	LaBr1	0.881	0.925	0.964	1.113	1.056	1.009
		LaBr2	0.881	0.925	0.964	0.835	0.871	0.909
		LaBr3	0.881	0.890	0.902	1.391	1.386	1.359
		LaBr4	1.469	1.470	1.442	0.835	0.839	0.850
	HPGe4	LaBr1	0.881	0.925	0.964	0.835	0.871	0.909
		LaBr2	0.881	0.925	0.964	1.113	1.056	1.009
		LaBr3	0.881	0.890	0.902	1.391	1.386	1.359
		LaBr4	1.469	1.470	1.442	0.835	0.839	0.850

Appendix B

Experimental supplement

B.1 Trigger generation matrices

The trigger generation matrices for the Trigger Logic (TrLoII) that were used in the configuration for the experimental setups in 2012 and 2013 are shown in tables B.1 and B.2, respectively. Due to the additional three small $LaBr_3$:Ce detectors in 2012, more trigger combinations were needed.

Table B.1: Trigger generation matrix for the experiments in 2012.

Output	12 Pulser	11 RF / BPU	10 HPGe 0°	9 HPGe M2	8 3" LaBr M2 High	7 3" LaBr M2 Low	6 HPGe OR High	5 HPGe OR Low	4 1.5" LaBr OR High	3 1.5" LaBr OR Low	2 3" LaBr OR High	1 3" LaBr OR Low
1 Singles LaBr											x	
2 Singles HPGe							x					
3 Coincidence Low-Low								x				x
4 LaBr M2 Low						x					x	
5 HPGe M2				x								
6 0°			x									
7 Pulser	x											
8 Coincidence Low-High							x					x
9 Singles 1.5" LaBr High									x			
10 Singles 3" LaBr Low												x
11 Singles HPGe Low								x				
12 Coincidence HPGe Low										x		x
13 Singles 1.5" LaBr Low										x		
14 Coincidence 1.5" LaBr-HPGe								x		x		
15 Coincidence High-Low								x			x	

Table B.2: Trigger generation matrix for the experiments in 2013.

Output	12 Pulser	11 RF / BPU	10 HPGe 0°	9 –	8 HPGe M2 High	7 HPGe M2 Low	6 LaBr M2 High	5 LaBr M2 Low	4 HPGe OR High	3 HPGe OR Low	2 LaBr OR High	1 LaBr OR Low
1 Singles LaBr											x	
2 Singles HPGe									x			
3 Coincidence Low-Low										x		x
4 Coincidence Low-High									x			x
5 LaBr M2 High								x			x	
6 HPGe M2 High						x			x			
7 0°			x									
8 Pulser	x											
9 Singles LaBr Low												x
10 Singles HPGe Low										x		
11 coincidence Low-High										x	x	

B.2 GHOST - Gamma Histogramming and Online Spectra Tool

To allow for monitoring of the data quality during the recording phase of the experiment it is useful to have the ability to quickly unpack, analyse and visualise the currently accumulated data. As described above, unpacking is handled by the UCESB unpacker, which cannot only read from already stored LMD files, but just as well read directly from a network stream provided by the data acquisition system. This was used to produce a temporary ROOT file containing the data that was currently being recorded. To read, analyse and display these files, the *Gamma Histogramming and Online Spectra Tool* (GHOST) was written as a ROOT program. This program, when invoked without any special options, opens up a window on the desktop showing the current status of the recorded data in ROOT histograms. Whenever new data is written to the temporary file, GHOST updates the content of the histograms automatically, leading to a near-realtime view of the data. Each detector of the γ^3 setup is represented with two energy (uncalibrated and calibrated) and two timing (raw and with respect to a reference detector) histograms. Additionally, it is possible to specify filtering conditions (e.g. timing constraints) for a special set of energy histograms. The main feature of the visualisation is the possibility to directly produce summed energy histograms of all detectors of each type and also two-dimensional matrices showing the energies of two coincident detector hits. Occasionally it was necessary to also monitor the gain stability of the HPGe detectors. For this reason histograms were added to show the time evolution of the HPGe energy histograms. Figure 3.10 shows two screen shots of the running application. In the top screen shot the energy spectra are shown for the $LaBr_3$:Ce detectors, and the bottom picture shows the view containing the summed energy spectra and the coincidence matrices. The concept of ROOT's *friend trees* has been used to efficiently store calibrated data without duplicating the parts of the tree that do not need any calibration. Filtering of the tree can be done using the special branch TPAT containing the *trigger pattern*. Instead of storing separate filtered trees according to the different TPAT selections, the concept of *entry lists* has been employed for the selection. This mechanism allows to write the list of entries in the tree that satisfy a specific condition (in this case a constraint on the values of TPAT) to a file. When analysing the entries in a tree, this file can be used as an additional input to skip unwanted events during processing. Depending on the condition this can constitute a significant speedup.

B.3 Backup strategies

Data recorded in nuclear physics experiments are valuable goods and should be treated as such. This includes not only the careful preparation and analysis, but extends to data handling and storage as well. In the γ^3 experimental campaigns of 2012 and 2013 about 5 TB of LMD files have been recorded during more than 1500 h of beam on target. Any data loss should be actively avoided by the experimenters at any point in time by employing reasonable data backup strategies, since the probability to either recover lost data or to be able to redo an experiment is surprisingly small. Data from the GENIE acquisition was written to disk every two hours and then copied to a local file server. This strategy ensured that never more than two hours worth of singles spectra could get lost. The MBS data was recorded on the readout PC, and directly mirrored using the RSYNC command to a locally mounted second hard drive as well as to the local file server. Additionally, all data was securely transmitted to the file storage at GSI in Germany on a daily basis, to serve as an off-site backup. Using RSYNC ensures that both copies of the data are identical by comparing MD5 hashes generated from the data. The data acquisition and related programs (such as the unpacker, GHOST and various maintenance scripts) were kept under version control using GIT and were also backed up on- and off-site. In case of fatal failure of the readout PC, the time to replace it would have included installing the operating system and copying over the files from the backup. This could have been done within a few hours, which was considered an appropriate time frame.

Bibliography

[1] P. Curie, M. Curie, and H. Becquerel, *Sur les corps radioactifs* (Gauthier-Villars, 1902).

[2] H. Geiger and E. Marsden, Philosophical Magazine Series 6 **25**, 604 (1913), ISSN 1941-5982.

[3] P. B. Moon, Proceedings of the Physical Society. Section A **64**, 76 (1951), ISSN 0370-1298.

[4] E. Hayward and E. Fuller, Physical Review **106**, 991 (1957), ISSN 0031-899X.

[5] R. Moreh, W. Sandefur, W. Sellyey, D. Sutton, and R. Vodhanel, Physical Review C **25**, 1824 (1982), ISSN 0556-2813.

[6] U. Berg, K. Ackermann, K. Bangert, C. Bläsing, W. Naatz, R. Stock, K. Wienhard, M. Brussel, T. Chapuran, and B. Wildenthal, Physics Letters B **140**, 191 (1984), ISSN 03702693.

[7] H. Ohgaki, T. Noguchi, S. Sugiyama, T. Yamazaki, T. Mikado, M. Chiwaki, K. Yamada, R. Suzuki, and N. Sei, Nuclear Instruments and Methods in Physics Research Section A: Accelerators, Spectrometers, Detectors and Associated Equipment **353**, 384 (1994), ISSN 0168-9002.

[8] N. Pietralla, H. Weller, V. Litvinenko, M. Ahmed, and A. Tonchev, Nuclear Instruments and Methods in Physics Research Section A: Accelerators, Spectrometers, Detectors and Associated Equipment **483**, 556 (2002), ISSN 0168-9002.

[9] N. Pietralla, Z. Berant, V. N. Litvinenko, S. Hartman, F. F. Mikhailov, I. V. Pinayev, G. Swift, M. W. Ahmed, J. H. Kelley, S. O. Nelson, et al., Phys. Rev. Lett. **88**, 012502 (2002).

[10] H. R. Weller, M. W. Ahmed, H. Gao, W. Tornow, Y. K. Wu, M. Gai, and R. Miskimen, Prog. Part. Nucl. Phys. **62**, 257 (2009).

[11] G. Baldwin and G. Klaiber, Physical Review **71**, 3 (1947), ISSN 0031-899X.

[12] W. Kuhn, Zeitschrift für Physik **33**, 408 (1925), ISSN 1434-6001.

[13] F. Reiche and W. Thomas, Zeitschrift für Physik **34**, 510 (1925), ISSN 1434-6001.

[14] M. Goldhaber and E. Teller, Physical Review **74**, 1046 (1948), ISSN 0031-899X.

[15] U. Kneissl, H. Pitz, and A. Zilges, Progress in Particle and Nuclear Physics **37**, 349 (1996), ISSN 0146-6410.

[16] M. Scheck, H. von Garrel, N. Tsoneva, D. Belic, P. von Brentano, C. Fransen, A. Gade, J. Jolie, U. Kneissl, C. Kohstall, et al., Physical Review C **70**, 044319 (2004), ISSN 0556-2813.

[17] H. von Garrel, P. Brentano, C. Fransen, G. Friessner, N. Hollmann, J. Jolie, F. Käppeler, L. Käubler, U. Kneissl, C. Kohstall, et al., Physical Review C **73**, 054315 (2006), ISSN 0556-2813.

[18] U. Kneissl, N. Pietralla, and A. Zilges, Journal of Physics G: Nuclear and Particle Physics **32**, R217 (2006).

[19] R. Georgii, T. von Egidy, J. Klora, H. Lindner, U. Mayerhofer, J. Ott, W. Schauer, P. von Neumann-Cosel, A. Richter, C. Schlegel, et al., Nuclear Physics A **592**, 307 (1995), ISSN 03759474.

[20] R. Georgii, P. von Neumann-Cosel, T. von Egidy, M. Grinberg, V. Khitrov, J. Ott, P. Prokofjevs, A. Richter, W. Schauer, C. Schlegel, et al., Physics Letters B **351**, 82 (1995), ISSN 03702693.

[21] M. Wilhelm, S. Kasemann, G. Pascovici, E. Radermacher, P. von Brentano, and A. Zilges, Physical Review C **57**, 577 (1998), ISSN 0556-2813.

[22] T. Poelhekken, S. Hesmondhalgh, H. Hofmann, A. van der Woude, and M. Harakeh, Physics Letters B **278**, 423 (1992), ISSN 03702693.

[23] G. A. Bartholomew, Annual Review of Nuclear Science **11**, 259 (1961), ISSN 0066-4243.

[24] R. Mohan, M. Danos, and L. Biedenharn, Physical Review C **3**, 1740 (1971), ISSN 0556-2813.

[25] K. Govaert, F. Bauwens, J. Bryssinck, D. De Frenne, E. Jacobs, W. Mondelaers, L. Govor, and V. Ponomarev, Physical Review C **57**, 2229 (1998), ISSN 0556-2813.

[26] A. Zilges, S. Volz, M. Babilon, T. Hartmann, P. Mohr, and K. Vogt, Physics Letters B **542**, 43 (2002), ISSN 03702693.

[27] N. Ryezayeva, T. Hartmann, Y. Kalmykov, H. Lenske, P. von Neumann-Cosel, V. Ponomarev, A. Richter, A. Shevchenko, S. Volz, and J. Wambach, Physical Review Letters **89**, 272502 (2002), ISSN 0031-9007.

[28] T. Hartmann, M. Babilon, S. Kamerdzhiev, E. Litvinova, D. Savran, S. Volz, and A. Zilges, Physical Review Letters **93**, 192501 (2004), ISSN 0031-9007.

[29] R. Schwengner, G. Rusev, N. Tsoneva, N. Benouaret, R. Beyer, M. Erhard, E. Grosse, A. Junghans, J. Klug, K. Kosev, et al., Physical Review C **78**, 1 (2008), ISSN 0556-2813.

[30] A. P. Tonchev, S. L. Hammond, J. H. Kelley, E. Kwan, H. Lenske, G. Rusev, W. Tornow, and N. Tsoneva, Phys. Rev. Lett. **104**, 072501 (2010).

[31] J. Isaak, D. Savran, M. Fritzsche, D. Galaviz, T. Hartmann, S. Kamerdzhiev, J. H. Kelley, E. Kwan, N. Pietralla, C. Romig, et al., Phys. Rev. C **83**, 034304 (2011).

[32] J. Isaak, D. Savran, M. W. Ahmed, J. Beller, E. Fiori, J. Glorius, J. H. Kelley, N. Pietralla, C. Romig, G. Rusev, et al. (2013).

[33] J. Endres, E. Litvinova, D. Savran, P. Butler, M. Harakeh, S. Harissopulos, R.-D. Herzberg, R. Krücken, A. Lagoyannis, N. Pietralla, et al., Physical Review Letters **105**, 1 (2010), ISSN 0031-9007.

[34] D. Savran, M. Elvers, J. Endres, M. Fritzsche, B. Löher, N. Pietralla, V. Y. Ponomarev, C. Romig, L. Schnorrenberger, K. Sonnabend, et al., Physical Review C **84**, 1 (2011), ISSN 0556-2813.

[35] V. Derya, J. Endres, M. N. Harakeh, D. Savran, H. J. Wörtche, and A. Zilges, Journal of Physics: Conference Series **366**, 012012 (2012), ISSN 1742-6596.

[36] V. Derya, J. Endres, M. Elvers, M. Harakeh, N. Pietralla, C. Romig, D. Savran, M. Scheck, F. Siebenhühner, V. Stoica, et al., Nuclear Physics A **906**, 94 (2013), ISSN 03759474.

[37] A. Leistenschneider, T. Aumann, K. Boretzky, D. Cortina, J. Cub, U. Pramanik, W. Dostal, T. Elze, H. Emling, H. Geissel, et al., Physical Review Letters **86**, 5442 (2001), ISSN 0031-9007.

[38] P. Adrich, A. Klimkiewicz, M. Fallot, K. Boretzky, T. Aumann, D. Cortina-Gil, U. Pramanik, T. Elze, H. Emling, H. Geissel, et al., Physical Review Letters **95**, 130 (2005), ISSN 0031-9007.

[39] O. Wieland and A. Bracco, Progress in Particle and Nuclear Physics **66**, 374 (2011), ISSN 01466410.

[40] B. Özel, J. Enders, P. von Neumann-Cosel, I. Poltoratska, A. Richter, D. Savran, S. Volz, and A. Zilges, Nuclear Physics A **788**, 385 (2007), ISSN 03759474.

[41] D. Vretenar, Y. F. Niu, N. Paar, and J. Meng, Physical Review C **85**, 044317 (2012), ISSN 0556-2813.

[42] X. Roca-Maza, G. Pozzi, M. Brenna, K. Mizuyama, and G. Colò, Physical Review C **85**, 024601 (2012), ISSN 0556-2813.

[43] D. Savran, T. Aumann, and A. Zilges, Progress in Particle and Nuclear Physics **70**, 210 (2013), ISSN 0146-6410.

[44] P. Ring and P. Schuck, *The nuclear many-body problem* (Springer, Heidelberg, 1980).

[45] J.-P. Blaizot and G. Ripka, *Quantum theory of finite systems*, vol. 3 (Mit Press Cambridge, 1986).

[46] A. Carbone, G. Colò, A. Bracco, L.-G. Cao, P. F. Bortignon, F. Camera, and O. Wieland, Physical Review C **81**, 041301 (2010), ISSN 0556-2813.

[47] P.-G. Reinhard and W. Nazarewicz, Physical Review C **81**, 051303 (2010), ISSN 0556-2813.

[48] H. Hergert, P. Papakonstantinou, and R. Roth, Physical Review C **83**, 064317 (2011), ISSN 0556-2813.

[49] E. G. Lanza, A. Vitturi, M. V. Andrés, F. Catara, and D. Gambacurta, Physical Review C **84**, 064602 (2011), ISSN 0556-2813.

[50] A. Vitturi, E. G. Lanza, M. V. Andres, F. Catara, and D. Gambacurta, Journal of Physics: Conference Series **267**, 012006 (2011), ISSN 1742-6596.

[51] D. Gambacurta, M. Grasso, V. De Donno, G. Co', and F. Catara, Physical Review C **86**, 021304 (2012), ISSN 0556-2813.

[52] M. Tohyama and T. Nakatsukasa, Physical Review C **85**, 031302 (2012), ISSN 0556-2813.

[53] G. Tertychny, V. Tselyaev, S. Kamerdzhiev, F. Grümmer, S. Krewald, J. Speth, A. Avdeenkov, and E. Litvinova, Physics Letters B **647**, 104 (2007), ISSN 03702693.

[54] S. Pascu, J. Endres, N. V. Zamfir, and A. Zilges, Physical Review C **85**, 064315 (2012), ISSN 0556-2813.

[55] E. Litvinova, P. Ring, and D. Vretenar, Physics Letters B **647**, 111 (2007), ISSN 03702693.

[56] E. Litvinova, P. Ring, V. Tselyaev, and K. Langanke, Physical Review C **79**, 054312 (2009), ISSN 0556-2813.

[57] E. Litvinova, P. Ring, and V. Tselyaev, Physical Review Letters **105**, 022502 (2010), ISSN 0031-9007.

[58] N. Tsoneva and H. Lenske, Physical Review C **77**, 024321 (2008), ISSN 0556-2813.

[59] N. Tsoneva and H. Lenske, Physics Letters B **695**, 174 (2011), ISSN 03702693.

[60] R.-D. Herzberg, P. von Brentano, J. Eberth, J. Enders, R. Fischer, N. Huxel, T. Klemme, P. von Neumann-Cosel, N. Nicolay, N. Pietralla, et al., Physics Letters B **390**, 49 (1997), ISSN 03702693.

[61] N. Paar, D. Vretenar, E. Khan, and G. Colo, Rep. Prog. Phys. **70**, 691 (2007).

[62] V. Derya, private communication (2013).

[63] S. Volz, N. Tsoneva, M. Babilon, M. Elvers, J. Hasper, R.-D. Herzberg, H. Lenske, K. Lindenberg, D. Savran, and a. Zilges, Nuclear Physics A **779**, 1 (2006), ISSN 03759474.

[64] J. Endres, D. Savran, A. M. van den Berg, P. Dendooven, M. Fritzsche, M. N. Harakeh, J. Hasper, H. J. Wörtche, and A. Zilges, Physical Review C **80**, 034302 (2009), ISSN 0556-2813.

[65] V. Yu. Ponomarev, private communication (2013).

[66] C. Angell, S. Hammond, H. Karwowski, J. Kelley, M. Krtička, E. Kwan, A. Makinaga, and G. Rusev, Physical Review C **86**, 051302 (2012), ISSN 0556-2813.

[67] P. Nolan, D. Todd, P. Smith, D. Love, P. Twin, O. Andersen, J. Garrett, G. Hagemann, and B. Herskind, Physics Letters B **108**, 269 (1982), ISSN 0370-2693.

[68] B. Cederwall, I. Lee, S. Asztalos, M. Brinkman, J. Becker, R. Clark, M. Deleplanque, R. Diamond, P. Fallon, L. Farris, et al., Nuclear Instruments and Methods in Physics Research Section A: Accelerators, Spectrometers, Detectors and Associated Equipment **354**, 591 (1995), ISSN 0168-9002.

[69] N. Pietralla, C. Fransen, D. Belic, P. von Brentano, C. Frieß ner, U. Kneissl, A. Linnemann, A. Nord, H. Pitz, T. Otsuka, et al., Physical Review Letters **83**, 1303 (1999), ISSN 0031-9007.

[70] B. Löher, V. Derya, T. Aumann, J. Beller, N. Cooper, M. Duchêne, J. Endres, E. Fiori, J. Isaak, J. Kelley, et al., Nuclear Instruments and Methods in Physics Research Section A: Accelerators, Spectrometers, Detectors and Associated Equipment **723**, 136 (2013), ISSN 01689002, 1304.6270.

[71] D. Bohle, A. Richter, W. Steffen, A. E. L. Dieperink, N. L. Iudice, F. Palumbo, and O. Scholten, Phys. Lett. B **137**, 27 (1984).

[72] N. L. Iudice and A. Richter, Physics Letters B **304**, 193 (1993), ISSN 0370-2693.

[73] K. Heyde, P. von Neumann-Cosel, and A. Richter, Rev. Mod. Phys. **82**, 2365 (2010).

[74] F. R. Metzger, Prog. in Nucl. Phys **53** (1959).

[75] R. M. Steffen and K. Alder, *The Electromagnetic Interaction In Nuclear Spectroscopy*, chap. Angular Distribution And Correlation Of Gamma Rays, vol. 1 of [76] (1975).

[76] W. D. Hamilton, ed., *The Electromagnetic Interaction In Nuclear Spectroscopy*, vol. 1 (North Holland Publishing Company, Amsterdam, Oxford, 1975).

[77] G. F. Knoll, *Radiation Detection and Measurement* (John Wiley and Sons, Inc, New York, 2000), 3rd ed.

[78] G. R. Gilmore, *Practical Gamma-Ray Spectroscopy* (John Wiley and Sons, Inc, New York, 2008), 2nd ed.

[79] P. H. V. Cittert, Z. Phys. **69**, 298 (1933).

[80] R. Gold, Argonne National Laboratory Report **ANL-6984** (1964).

[81] M. Morháč, J. Kliman, V. Matoušek, M. Veselský, and I. Turzo, Nuclear Instruments and Methods in Physics Research Section A: Accelerators, Spectrometers, Detectors and Associated Equipment **401**, 385 (1997), ISSN 0168-9002.

[82] *ROOT Framework Home Page*, http://root.cern.ch/ (2010).

[83] M. Jandel, M. Morháč, J. Kliman, L. Krupa, V. Matoušek, J. Hamilton, and A. Ramayya, Nuclear Instruments and Methods in Physics Research Section A: Accelerators, Spectrometers, Detectors and Associated Equipment **516**, 172 (2004), ISSN 01689002.

[84] A. N. Tikhonov and V. Y. Arsenin, *Solution of Ill-posed Problems* (Winston & Sons, Washington, 1977), ISBN 0-470-99124-0.

[85] L. Federici, G. Giordano, G. Matone, G. Pasquariello, P. G. Picozza, R. Caloi, L. Casano, M. P. Pascale, M. Mattioli, E. Poldi, et al., Il Nuovo Cimento B **59**, 247 (1980), ISSN 0369-3554.

[86] C. Sun, J. Li, G. Rusev, A. Tonchev, and Y. Wu, Physical Review Special Topics - Accelerators and Beams **12**, 062801 (2009), ISSN 1098-4402.

[87] C. Sun, Y. Wu, G. Rusev, and A. Tonchev, Nuclear Instruments and Methods in Physics Research Section A: Accelerators, Spectrometers, Detectors and Associated Equipment **605**, 312 (2009), ISSN 01689002.

[88] N. Pietralla, T. Li, M. Fritzsche, M. Ahmed, T. Ahn, A. Costin, J. Enders, J. Li, S. Müller, P. von Neumann-Cosel, et al., Phys. Lett. B **681**, 134 (2009).

[89] S. Riboldi, F. Camera, N. Blasi, S. Brambilla, C. Boiano, F. C. Crespi, A. Giaz, B. Million, R. Nicolini, L. Pellegri, et al., in *2011 IEEE Nuclear Science Symposium Conference Record* (IEEE, 2011), pp. 776–778, ISBN 978-1-4673-0120-6.

[90] A. Giaz, L. Pellegri, S. Riboldi, F. Camera, N. Blasi, C. Boiano, A. Bracco, S. Brambilla, S. Ceruti, S. Coelli, et al., Nuclear Instruments and Methods in Physics Research Section A: Accelerators, Spectrometers, Detectors and Associated Equipment **729**, 910 (2013), ISSN 01689002.

[91] P. Dorenbos, J. de Haas, and C. van Eijk, IEEE Transactions on nuclear science **51**, 1298 (2004), ISSN 0018-9499.

[92] F. Quarati, A. Owens, P. Dorenbos, J. de Haas, G. Benzoni, N. Blasi, C. Boiano, S. Brambilla, F. Camera, R. Alba, et al., Nuclear Instruments and Methods in Physics Research Section A: Accelerators, Spectrometers, Detectors and Associated Equipment **629**, 157 (2011), ISSN 01689002.

[93] J. Allison, K. Amako, J. Apostolakis, H. Araujo, P. Arce Dubois, M. Asai, G. Barrand, R. Capra, S. Chauvie, R. Chytracek, et al., IEEE Transactions on Nuclear Science **53**, 270 (2006).

[94] B. Löher, D. Savran, E. Fiori, M. Miklavec, N. Pietralla, and M. Vencelj, Nuclear Instruments and Methods in Physics Research Section A: Accelerators, Spectrometers, Detectors and Associated Equipment **686**, 1 (2012), ISSN 0168-9002.

[95] H. Essel and N. Kurz, Nuclear Science, IEEE Transactions on **47**, 337 (2000), ISSN 0018-9499.

[96] Marcin Wojdyr and Peng Zhang, *xylib*, http://xylib.sourceforge.net (2013).

[97] K. Große, *GSI Scientific Report 2010 [GSI Report 2011-1]*, vol. 2011-1 of *GSI Report* (GSI, Darmstadt, 2011), wissenschaftlicher Ergebnisbericht der GSI, GSI Annual Report, URL `http://repository.gsi.de/record/53521`.

[98] H. T. Johansson, *The UCESB unpacker generator, Long write-up - documentation and manual*, http://fy.chalmers.se/ f96hajo/ucesb (2010).

[99] C. Sun, Dissertation, Duke University (2009), URL `http://hdl.handle.net/10161/1579`.

[100] S. Carson, C. Iliadis, J. Cesaratto, A. Champagne, L. Downen, M. Ivanovic, J. Kelley, R. Longland, J. R. Newton, G. Rusev, et al., Nuclear Instruments and Methods in Physics Research Section A: Accelerators, Spectrometers, Detectors and Associated Equipment **618**, 190 (2010), ISSN 0168-9002.

[101] P. Menge, G. Gautier, A. Iltis, C. Rozsa, and V. Solovyev, Nuclear Instruments and Methods in Physics Research Section A: Accelerators, Spectrometers, Detectors and Associated Equipment **579**, 6 (2007), ISSN 01689002.

[102] A. Iltis, M. Mayhugh, P. Menge, C. Rozsa, O. Selles, and V. Solovyev, Nuclear Instruments and Methods in Physics Research Section A: Accelerators, Spectrometers, Detectors and Associated Equipment **563**, 359 (2006), ISSN 01689002.

[103] D. Savran, M. Fritzsche, J. Hasper, K. Lindenberg, S. Müller, V. Ponomarev, K. Sonnabend, and A. Zilges, Physical Review Letters **100** (2008), ISSN 0031-9007.

[104] C. Romig, private communication (2014).

[105] N. NICA, *Nuclear data sheets 108,1287* (2007).

[106] M. Babilon, T. Hartmann, P. Mohr, K. Vogt, S. Volz, and A. Zilges, Phys. Rev. C **65**, 037303 (2002).

[107] M. Viitasalo and I. Forsblom, Zeitschrift für Physik **269**, 173 (1974), ISSN 0044-3328.

[108] M. N. Harakeh and A. Woude, *Giant Resonances: Fundamental High-Frequency Modes of Nuclear Excitation*, vol. 24 (Oxford University Press, 2001).

[109] M. Büssing, M. Elvers, J. Endres, J. Hasper, A. Zilges, M. Fritzsche, K. Lindenberg, S. Müller, D. Savran, and K. Sonnabend, Physical Review C **78**, 044309 (2008), ISSN 0556-2813.

[110] FAIR GmbH and GSI, *Green Paper, The Modularized Start Version : FAIR - Facility for Antiproton and Ion Research* (FAIR, Damstadt, 2009), URL `http://repository.gsi.de/record/54094`.

[111] ELI-NP, *The White Book of ELI Nuclear Physics Bucharest-Magurele, Romania*, http://www.eli-np.ro/documents/ELI-NP-WhiteBook.pdf (2013).